1998

The Structure and Stability of Selected, 2-D Self-Gravitating Systems.

Saied W. Andalib
Louisiana State University and Agricultural & Mechanical College

INFORMATION TO USERS

This manuscript has been reproduced from the microfilm master. UMI films the text directly from the original or copy submitted. Thus, some thesis and dissertation copies are in typewriter face, while others may be from any type of computer printer.

The quality of this reproduction is dependent upon the quality of the copy submitted. Broken or indistinct print, colored or poor quality illustrations and photographs, print bleedthrough, substandard margins, and improper alignment can adversely affect reproduction.

In the unlikely event that the author did not send UMI a complete manuscript and there are missing pages, these will be noted. Also, if unauthorized copyright material had to be removed, a note will indicate the deletion.

Oversize materials (e.g., maps, drawings, charts) are reproduced by sectioning the original, beginning at the upper left-hand corner and continuing from left to right in equal sections with small overlaps. Each original is also photographed in one exposure and is included in reduced form at the back of the book.

Photographs included in the original manuscript have been reproduced xerographically in this copy. Higher quality 6" x 9" black and white photographic prints are available for any photographs or illustrations appearing in this copy for an additional charge. Contact UMI directly to order.

UMI

A Bell & Howell Information Company
300 North Zeeb Road, Ann Arbor MI 48106-1346 USA
313/761-4700 800/521-0600

THE STRUCTURE AND STABILITY OF SELECTED, 2-D SELF-GRAVITATING SYSTEMS

A Dissertation

Submitted to the Graduate Faculty of the
Louisiana State Unviersity and
Agricultural and Mechanical College
in partial fulfillment of the
requirements for the degree of
Doctor of Philosopy

in

The Department of Physics and Astronomy

by
Saied Andalib
B.S., Virginia Polytechnique Institute & State University, 1983
M.S., Louisiana State University, 1987
M.S., Louisiana State University, 1990
May 1998

ACKNOWLEDGEMENTS

First, I would like to thank God for the completion of my higher education. Also, I would like to thank my advisor, Dr. Joel E. Tohline for his help and understanding along with his guidance throughout my years at LSU. Through his patience, kindness, and scientific knowledge, it was a great experience working with him.

Many thanks to Ophelia Dudley along with her family, for her patience and understanding for typing and late hours of work.

I would also like to thank Dimitris M. Christodoulou for his numerous help on many occasions throughout my stay at LSU.

I would like to thank Howard Cohl for his help on IDL and John Cazes for the 3D animation. I would also like to thank Hortensia Valdes and Monika Lee for their help with software.

Thanks to Karla Lockwood for helping in solving many problems with the use of the word processor.

TABLE OF CONTENTS

Acknowledgements ii

Abstract v

Chapter

1. Introduction 1
   - 1.1 Analytical vs. Computational Approach 2
   - 1.2 Stellar Hydrodynamics 3
   - 1.3 Numerical Simulations 5
   - 1.4 Finite Difference Schemes 6
   - 1.5 Classical Equilibrium Structures 7
   - 1.6 Recent Developments 9
   - 1.7 Our Advancements 11

2. Basic Hydrodynamic Equations 15
   - 2.1 Euler's Equation 15
   - 2.2 Thermodynamics Considerations 16
   - 2.3 The Gravitational Potential 17
   - 2.4 Rotating Frame of Reference 18
   - 2.5 The Equation of Continuity 20
   - 2.6 The Equation of State 20
   - 2.7 Axisymmetric Euler's Equation 22

3. Stability of Accretion Tori 24
   - 3.1 Equilibrium Structure of ICT Models 25
   - 3.2 Parameterization 26
   - 3.3 Equilibrium Enthalpy 28
   - 3.4 Properties of the Equilibrium Models 31
   - 3.5 Global Physical Quantities 35
   - 3.6 Comparison with Numerical ICT Models 39
   - 3.7 The Narrow Torus Approximation 42
   - 3.8 The Principal Modes of Nonaxisymmetric Instability 45
   - 3.9 Regions of Unstable P-, I-, and J-Modes 47
   - 3.10 The P-modes 51
   - 3.11 The I-modes 54
   - 3.12 The J-modes 63
   - 3.13 I-modes vs. J-modes 71
   - 3.14 Comparison with Previously Obtained Results 72

4. Two-Dimensional Nonaxisymmetric Systems 79
4.1 Equilibrium Models of 2D, Compressible Fluids 80
4.2 Solutions of Euler's Equation 82
4.3 Stream Function and Its Associated PDE 84
4.4 Dirichlet Boundary Condition 86
4.5 Stream Function and Streamlines 87
4.6 Numerical Scheme and Discretization 87
4.7 Iteration Procedure 89
4.8 The Internal Circulation 90

5. Steady State Structures 92
5.1 Infinite Cylinders 98
5.2 Two-Dimensional Disks 120
5.3 Present Numerical Restrictions 153

6. Summary and Conclusion 154

References 162

Vita 164

ABSTRACT

Models of radially and vertically extended self-gravitating disks orbiting a central point mass are relevant to the dynamics of astrophysical systems and are thought to be common in many galaxies. The gravity driven instabilities in these accretion disks are now believed to be a possible mechanism for star formation via disk fragmentation (Shu, Adams, & Lizano 1987, Adams, Rudin & Shu 1989; Christodoulou 1995 a, b).

We quantify these regions of instability using a simple toroidal model of an accretion disk. We choose the two-dimensional axisymmetric, incompressible slender disks to examine and map out these principal modes of gravity driven instabilities. Through stability analyses and numerical simulations we have found that only the gravity driven "intermediate" modes (see Goodman and Narayan 1988) are important in all self-gravitating accretion disks with small or moderate axis ratios. The P-mode instability found by Papalaizou and Pringle (1984) is unlikely to play a role in the dynamics of realistic disk systems.

Next, we extend the existing numerical methods for constructing equilibrium structures to include nonaxisymmetric systems. We have developed a new computational technique to obtain two-dimensional, nonaxisymmetric, compressible systems with nontrivial internal motions. We have constructed two types of two-dimensional configurations: infinite cylinders and infinitesimally thin disks. The infinite cylinders have been primarily restricted to elliptic-like boundaries but the disks have exhibited much more flexibility in their geometries. At smaller axis ratios,

they become dumbbells or loosely coupled binaries. The topology and dynamics of the flow is governed by the presence of vortices and stagnation points. In our simulation it is shown that there are equilibrium configurations that can only exist in the presence of internal differential motions and not in uniformly rotating models.

This indicates that in general, the equilibrium structures of these nonaxisymmetric configurations are dependent not just on the constant frame rotation but perhaps even more importantly on the internal differential motion. This is especially important when we construct nonaxisymmetric models with high $T/|W|$, where T and W are the kinetic and the gravitational potential energy respectively. In these systems, most of the contribution to $T/|W|$ comes from internal rotation.

CHAPTER 1

INTRODUCTION

The structural properties, the stability, and the dynamical evolution of rotating self-gravitating gas clouds are of wide astrophysical interest. Through fluid dynamical simulations of these clouds we have powerful new tools to study and analyze a variety of astronomical objects. The allowed equilibrium structures of protostellar models, for example, and a more complete understanding of their evolution, their possible breakup and fragmentation, may provide us the necessary clues and information to understand star formation and galaxy structures. The process by which stars and galaxies form is one of the major topics in astronomy. Our current theoretical understanding in this area is far from complete and further investigations are required.

Many galactic disks are essentially two-dimensional in nature and show nonaxisymmetric features. Their centralmost regions often have bar mode geometry. Nonaxisymmetric structures are also relevant to our understanding of star formation and binary systems. If gravitationally collapsed objects like black holes and neutron stars also possess nonaxisymmetric geometries, such object will be strong sources of gravitational radiation. Therefore, it is important to better understand the structure and dynamics of general compressible nonaxisymmetric configurations.

One key step toward a better understanding of the dynamics and internal structure of galaxies and stars, is to investigate the equilibrium configurations of such objects. These rotating self-gravitating gaseous structures are thought to be figures

of equilibrium where gravitational, centrifugal, and thermal pressure forces are in detailed balance. Therefore, by investigating and classifying all possible figures of equilibrium and their modes of instability we will be able to form a more complete theoretical picture of these astrophysical structures. In particular, we study the unstable modes in the axisymmetric accretion disks and discuss their relative importance to disk fragmentation.

A comprehensive stability analysis of astrophysical systems requires the construction of compressible triaxial equilibrium structures with internal differential motion. At present, however, this is still out of our reach. As a result, we develop a two-dimensional computational method as an effort in that direction to serve as an intermediate step until the full solution is realized in the future.

1.1 Analytical vs. Computational Approach

Our understanding of many important astrophysical phenomena has been mainly driven by new and sophisticated observations and in large part by the increasing capabilities of current generations of computers, along with the emergence of efficient and powerful computational techniques. The latter are of special significance. The dynamics of many astrophysical phenomena are governed by a complicated set of coupled nonlinear partial differential equations (PDEs). Analytical treatments of these equations are very rare and at best limited to highly idealized and simplified models (e.g., one dimensional, spherical symmetry, incompressibility, small perturbation, etc.) which, as a result, have little or no resemblance to the actual astronomical phenomena. A typical example of a system

involving coupled nonlinear PDEs is the equations describing the motion of fluids. Without some very specific and simplifying assumptions, analytical solutions to this relatively simple system of equations cannot be found.

The only alternative, then, to obtain physically realistic models is to seek computational methods and algorithms to obtain numerical solutions to these equations. Computational astrophysics is a relatively young, but rapidly growing discipline. Over the years it has become an important and integral part of theoretical astrophysics. Both analytical and numerical techniques have their own unique strengths and weaknesses. An analytical solution, if possible, can provide great insight into the underlying physical laws governing the system, but as mentioned earlier it is generally limited to highly idealized and simplified models. Computational methods on the other hand, are applicable to a wide range of astronomical problems, but it is often much more difficult to gain insight into the dynamics of the system under consideration. However, if a numerical scheme has been well designed for a specific problem, it is a relatively easy task to modify it to broaden its domain of applicability, and to solve a much broader class of problems than are solvable through purely analytical techniques.

1.2 Stellar Hydrodynamics

Many astrophysical systems (e.g., stars, galaxies, interstellar gas clouds, or accretion disks) are governed by the laws of gas dynamics and can be described by the equations of self-gravitating compressible hydrodynamic systems. Modeled on this classical hydrodynamics foundation, one may regard these systems to be

continuous rather than particulate in structure. In this scenario, the macroscopic matter will be of primary interest. The matter in bulk is considered to be continuous no matter how small the portion may be. The fluid constituents are assumed to have the same identical properties as those of the bulk fluid at all macroscopic levels. Furthermore, the requirement of the continuous fluid concept is carried out down to the smallest dimensions relevant from the classical Newtonian viewpoint. This is so that Newton's laws of particle mechanics will be applicable. To that end, one may make an appropriate definition of a fluid particle to be a small continuous fluid element which is infinitesimal on the macroscopic scale but very large at the molecular level. Such a fluid particle containing a large aggregate of molecules is then treated as an idealized point particle which can be described by the laws of classical mechanics. A fluid element is to maintain all its microscopic constituents for a long period of time on the astronomical scale. Hence, the mean free path for collision for the constituent molecules must be very small relative to the size of the fluid element. The microscopic properties of the matter which arise from the molecular motions of the fluid are then accounted for implicitly through thermodynamic considerations. It is further assumed that the environment is in local thermodynamic equilibrium. This is required in order to calculate the equation of state, through which various macroscopic parameters like fluid density, pressure, and temperature, etc. are related to each other; e.g., $f(\rho, P, T, \cdots) = 0$. We will be interested primarily in systems

with barotropic equations of state where the pressure is only dependent on density: $P = P(\rho)$.

1.3 Numerical Simulations

It is of particular significance to understand the astrophysical phenomena through numerical investigations. With the advent of increasingly powerful computers and the availability of new efficient computational techniques, computer simulations of astrophysical systems are rapidly gaining importance. In most circumstances, numerical modeling may be the only way to acquire a detailed understanding about these physical systems. Each numerical scheme has its own strengths and weaknesses. The choice of the most suitable method depends in part on the physical system under consideration.

There are several types of computational schemes one may choose from, such as finite-difference, finite-element, Monte-Carlo, and other statistical methods. Furthermore, the choice of the coordinate system itself could be either Eulerian or Lagrangian. In an Eulerian hydrodynamic description, the coordinate system is fixed in space, whereas in a Lagrangian description it is attached to the fluid elements. Often a Lagrangian description is the preferred choice in one dimensional configurations since the partial derivatives are reduced to total derivatives and the equations are simplified. In two and three dimensions, however, the grid may become severely distorted very quickly and the numerical treatments become less accurate. Eulerian formulations on the other hand do not suffer from this grid

distortion problem and therefore often are the preferred approach in multidimensional simulations.

1.4 Finite Difference Schemes

Of the various numerical methods, one which is widely adopted throughout the computational disciplines and in astrophysical fluid dynamics in particular, is the finite-difference method. It involves transforming the set of PDEs into approximate algebraic expressions which are much simpler to solve. This is achieved by discretizing the corresponding analytical equations in a space-time continuum into their equivalent difference forms. The resulting algebraic equations are then applied on some suitably chosen grid at each computational cell. The choice of the computational grid is dictated mainly by the physical characteristics and the symmetries inherent in the system. The analytical functions are then evaluated at the center, corners or on the edges of these grid cells. Similarly, the partial derivatives are calculated by the differences between adjacent cells. If the original PDEs are linear, then their corresponding algebraic equations are also linear. The system of linear equations so obtained are always very sparse; that is, the corresponding coefficient matrix is almost entirely made of zeros. Numerous optimized and efficient algorithms have been developed for this type of numerically intensive problem. The solution to this matrix equation if it exists is the solution of the corresponding PDEs on those grid points within the allowed error bounds. If, on the other hand, the PDEs are nonlinear, the system of algebraic equations so obtained are also nonlinear and can be solved via special methods such as Newton-

Raphson's method. There is no general method to handle nonlinear equations and they are usually treated on an individual basis.

1.5 Classical Equilibrium Structures

The study of the influence of gravity and rotation on the evolution and internal structure of the stars dates back to the time of Newton. A slowly rotating oblate spheroid with small ellipticity was considered to be a possible figure of equilibrium (see Chandrasekhar 1969). The ellipticity was defined by the ratio of perpendicular to the equatorial axis and was related to the relative strength of the gravitational and centrifugal forces.

The general proof that any uniformly rotating, homogeneous oblate spheroid with arbitrary ellipticity is a possible figure of equilibrium was furnished by Maclaurin (1742). He showed that there was a direct relationship between the ellipticity e, the uniform mass density ρ, and the constant angular velocity Ω required for equilibrium:

$$\frac{\Omega^2}{\pi G\rho} = 2\frac{\sqrt{1-e^2}}{e^3}(3-2e^2)\sin^{-1}e - \frac{6}{e^2}(1-e^2) .$$

Axially symmetric configurations, although very significant, are not the only possible figures of equilibrium. It was shown by Jacobi (1834) that a solidly rotating, homogeneous triaxial ellipsoidal figure also can be in a state of equilibrium. Later, Meyer (1842) showed that at an ellipticity e = 0.813 (T/|W| = 0.14), the Jacobi sequence bifurcates from the Maclaurin sequence. This classical work on

ellipsoidal figures of equilibrium has been reviewed extensively by Chandrasekhar (1969).

The classical equilibrium figures reviewed by Chandrasekhar were all either uniformly rotating with constant angular velocity Ω or they had simple linear internal motions. At one extreme are stationary ellipsoidal models ($\Omega = 0$) where internal fluid flow along elliptical streamlines will compensate for the lack of the frame rotation. The existence of such figures was proven by Dedekind (1860). The problem of the general condition for the existence of ellipsoidal configurations with linear motions was posed by Dirichlet (1860), where he was able to demonstrate a detailed solution in the special case of spheroids. The complete solution was obtained by Riemann (1860), where the flow was shown to be a superposition of a constant frame rotation coupled with an internal flow of uniform vorticity. Therefore, Riemann ellipsoids have the Maclaurin spheroids and Jacobi and Dedekind ellipsoids as special cases.

The existence of other types of nonaxisymmetric objects came next. In particular, the existence of pear-shaped figures was established by Poincare. Specifically, Poincare (1885) showed the existence of a bifurcation point along the Jacobi sequence, where a new pear-shaped sequence branches off. He also put forward the general theory of the equilibrium and stability of ellipsoidal figures and introduced the concept of bifurcation.

Two-dimensional equilibrium configurations such as infinite cylinders and their stability modes were studied by Jeans (1902) around the turn of the century.

Infinite cylinders with circular and elliptical cross-sections and those with a slight deformation on the surface were investigated via analytical techniques. He identified points of bifurcation along both the circular and elliptical sequences and, in particular, he found the two-dimensional analog of the Maclaurin spheroids and the Poincare pear-shaped sequences. The models considered by Jeans had no internal flow, and the equilibrium was maintained through constant frame rotation. The possible figures of equilibrium were dependent on Ω, the constant angular rotation of the figure.

1.6 Recent Developments

These classical analyses of the existence and stability of possible equilibrium configurations have generally focused on incompressible structures and occasionally simple axisymmetric compressible cases. In addition, the majority of the models considered had no internal flow or had a simple linear motion at best. Although they provided fundamental advancements in our understanding of the equilibrium structures of rotating objects, they were still of limited applicability to real astrophysical objects. They were based entirely on analytical methods and they are now superseded by numerical techniques.

Many of the interesting stellar phenomena occurring in nature are based on compressible fluids without axial symmetry, and they exhibit complicated nonlinear internal motions. These early works however, provided the foundation for the subsequent developments in this field especially towards constructing better and

more realistic models that more closely resemble the naturally occurring astrophysical structures.

One primary goal has been to solve the equations governing the compressible fluid dynamics in astronomical objects such as stars and galaxies. In principle, one would like to be able to construct a fully 3D, self-gravitating compressible equilibrium model with no restriction on the type of internal flow and free from any symmetry assumptions. In other words, one would like to develop a computational scheme where the general solution to the full set of the nonlinear hydrodynamic equations and all the forces involved are realized. In practice, however, this has proven to be an exceedingly difficult and intractable problem. Thus, many of the numerical techniques and algorithms developed in this field over the years have been designed to solve only certain special classes in the problem domain. They are each optimized and applied to a subset of the full equations governing specific hydrodynamic systems of interest. A substantial part of our present work (see § 1.8, below) is devoted toward the development of better tools with which to complete this task.

In a relatively recent study of the stability of astrophysical fluid disks, Papaloizou & Pringle (1984, P&P hereafter) made the discovery that massless accretion tori orbiting a central star are unstable to nonaxisymmetric modes (P-modes). Their analysis was further generalized by Goodman & Narayan (1988, GN hereafter) to self-gravitating accretion disks who discovered two additional nonaxisymmetric modes of instability; the "intermediate" and the Jeans modes (I-

and J- modes, respectively). These discoveries suggested the possibility of disk fragmentation as a viable mode of star formation.

1.7 Our Advancement

We continue this trend by developing a new computational method to obtain a special class of two-dimensional structures. In chapter 2 we present the basic hydrodynamic equations describing the motion of an isentropic compressible fluid with no viscosity. Since generally self-gravity cannot be ignored in many astronomical systems, the gravitational potential is incorporated into the equations via a solution of the Poisson equation for a given density distribution. The fluid density and velocity field are further constrained through the continuity equation to ensure mass conservation. The momentum equations and the equation of continuity supplemented by the polytropic equation of state fully describe the system. Hachisu's Self-Consistent-Field (HSCF) technique is then discussed and used in Chapter 3 to obtain equilibrium structures of slender accretion tori.

In subsequent chapters we proceed with two relatively independent tasks: the stability analysis of self-gravitating accretion tori and the construction of two-dimensional nonaxisymmetric equilibrium systems with nontrivial internal flows.

In Chapter 3 we present a survey of the above three principal nonaxisymmetric modes of instability (the P-, I- and J-modes) that have been found in rotating, self-gravitating, accretion-disk models. We adopt the standard idealized model of accretion tori orbiting a central star. GN described their linear stability analysis in terms of dimensionless parameters (p, ß), where p was a measure of the disk self-

gravity and ß was effectively the mode number of the instability. We consider the parameterization in the (M_D/M_C, T/|W|)-plane, where M_D and M_C are the disk mass and the central point mass respectively, to be more appropriate since these parameters are physically well understood. In particular, the dimensionless parameter T/|W| serves as a standard stability parameter in rapidly rotating, self-gravitating systems. Furthermore, in their linear stability analysis, GN did not distinguish between Ω_o, the orbital frequency of disk material at the pressure maximum and Ω_K, the Keplerian frequency. As we explain in more detail in chapter 3, these two frequencies can be considered equal only in the limit $M_D/M_C \rightarrow 0$. We have improved upon the GN presentation, clearly distinguishing between these frequencies and therefore extending the applicability of their analysis to systems with larger disk masses.

The I- and J-modes are primarily driven by self-gravity, so they appear in all models with nonzero torus mass that are sufficiently slender; the J-modes dominate over the I-modes only in the most slender of the unstable models; and the corresponding regions of instability are not expected to be strongly dependent on the assumption of incompressibility or on the particular choice of the angular momentum profile. The P-modes appear only at extremely low mass ratios (M_D/M_C,T/|W| $\leq 1.15 \times 10^{-3}$) and only in extremely slender tori (aspect ratio $\varepsilon \leq$ 0.02733). Thus, they probably play no role in the dynamical evolution of realistic

disk systems and the I-modes emerge as the most important modes of instability for all self-gravitating accretion disks with small or moderate aspect ratios.

In Chapter 4 we develop a new computational method (2DSCF) to obtain equilibrium models of two-dimensional, nonaxisymmetric compressible systems with nontrivial internal flows. The motivation for this effort has been threefold. First, the stability analysis of the equilibrium figures has historically been limited to incompressible gases with axial symmetry or to nonaxisymmetric structures but with very simple angular velocity distributions. Real astrophysical systems are compressible and when compressible figures are constructed with simple linear flow, T/|W| is limited to very small values. Higher Ω will lead to shedding of material at the boundary due to centrifugal force. To obtain higher ratios of T/|W| without causing equatorial mass shedding, it becomes necessary to have the kinetic energy come mostly from the internal flow rather than from the uniform frame rotation. This, in turn, will require a more complex and nonlinear specification of the internal angular velocity $\omega(x, y)$. Second, as we will see in chapter 5, uniform rotation is not adequate in all cases. There exist equilibrium configurations that cannot be constructed with uniform rotation, and they can only exist with some type of internal motion. Third, these new models are designed to bridge the gap between the three-dimensional, nonaxisymmetric, incompressible models with simple internal flows at one extreme and fully general three-dimensional, compressible models with nontrivial velocity fields to be obtained in the future.

In our 2DSCF technique, nonlinear vortical flow is controlled via a set of free parameters allowing for different flow topologies. In particular, the stream function is calculated as a boundary value problem using standard methods. In chapter 5 we construct several two-dimensional structures using the techniques developed in chapter 4. We construct compressible analogs of the classical incompressible sequences. Additionally, we construct dumbbell shaped configurations with very small axis ratios that are almost loosely coupled binaries. They possess highly nonlinear and complex vortical internal flow. Finally, in chapter 6 we present a summary of the results along with some concluding remarks.

CHAPTER 2

BASIC HYDRODYNAMIC EQUATIONS

In this chapter we present the necessary equations describing the motion of a self-gravitating, compressible fluid in a rotating frame of reference. These equations will be used in subsequent chapters when we construct equilibrium models of rotating fluids and test their stability. First, Euler's momentum equation (ME) is presented for a particular class of fluids, then it is transformed to a frame of reference that is rotating with a constant angular velocity Ω about the z-axis. Euler's equation along with the equation of continuity (EOC), the Poisson equation, and an appropriate equation of state are sufficient to completely describe the dynamics of the astrophysical fluid systems being considered here. A special case of Euler's equation that is relevant to axisymmetric structures with a power-law velocity profile is derived at the end of this chapter and drawn upon in chapter 3 when we study models with azimuthal symmetry. Throughout the derivations we will use cylindrical coordinates.

2.1 Euler's Equation

To describe the fluid flow in a dynamically consistent fashion, we adopt the basic form of Euler's equation presented in chapter 1 of Landau & Lifshitz (1987). That is,

$$\frac{d\mathbf{V}}{dt} = -\frac{\nabla P}{\rho} - \nabla\Phi , \tag{2.1}$$

where **V** is the velocity, P is the pressure, ρ is the mass density, and Φ is the total gravitational potential. We restrict our discussions to ideal fluids. Hence, we assume no irreversible processes will occur and that there will be no heat transfer during the flow. In other words, the specific entropy of the fluid will not change with time. Furthermore, we discuss only isentropic models. Another characteristic of ideal fluids is that the flow involves no viscous dissipation, that is, the fluid is said to be invicid. These two properties, when incorporated into the derivations, reduce the complexity of Euler's equation.

2.2 Thermodynamics Considerations

Here we utilize the thermodynamic properties of ideal fluids to recast eq. (2.1) into a form more suitable for computations. Let H and U be the enthalpy per unit mass and internal energy per unit mass of the fluid, respectively. These two state variables are related through the expression,

$$dH = dU + d(P/\rho) . \tag{2.2}$$

From the second law of thermodynamics, furthermore, we have,

$$TdS = dU + Pd(1/\rho) , \tag{2.3}$$

where T and S are the absolute temperature and the entropy per unit mass of the fluid. Since $dS = 0$ in an isentropic fluid, relation (2.2) implies $dU = -Pd(1/\rho)$, and relation (2.2) in turn yields the following relationship for isentropic fluids:

$$dH = dP/\rho. \tag{2.4}$$

Hence,

$$\nabla H = \frac{\nabla P}{\rho}, \tag{2.5}$$

and Euler's equation takes the form

$$\frac{dV}{dt} = -\nabla(H+\Phi). \tag{2.6}$$

2.3 The Gravitational Potential

Since self-gravity generally cannot be ignored in astrophysical contexts, in general the gravitational potential Φ that appears on the right hand side of Euler's equation will be the sum of an "internal disk" potential Φ_D, and the potential from any external sources, Φ_C. That is

$$\Phi = \Phi_C + \Phi_D \ . \tag{2.7}$$

Throughout this work the internal disk potential will be obtained from a solution of the Poisson equation

$$\nabla^2\Phi_D = 4\pi G\rho, \tag{2.8}$$

where G is the gravitational constant. In chapter 3, we will examine the structure and stability of axisymmetric fluid disks (tori) in the presence of a central point mass M_C, in which case the external potential under consideration will be given by the function

$$\Phi_C = -\frac{GM_C}{\sqrt{R^2+Z^2}}, \tag{2.9}$$

where R and Z are cylindrical coordinates.

2.4 Rotating Frame of Reference

When studying the properties of rotating astrophysical fluid systems, we must generally expect the internal fluid flow to be characterized by differential rotation and motion that, in general, may be nonaxisymmetric. In steady-state configurations we also expect the fluid to move along a family of closed streamlines, but a streamline may display complicated topologies due to the presence of vortices and stagnation points. When vortices are present, the dynamics of the flow is governed by the interactions among these vortices. In particular, when viewed from a proper frame, the flow may be divided into several nonoverlapping regions, each identified by a vortex at its center. In examining such flows, it often proves instructive to separate the fluid motion into two entirely distinct components: One due to the "mean" rotation of the fluid configuration and a second that characterizes the internal differential motion of the fluid. The first of these usually is characterized by a constant angular velocity Ω about some axis (which we choose to be the Z-axis) such that, from the point of view of an observer in a frame rotating with the same Ω either the surface of the equilibrium configuration or the fluid itself will appear to be at rest. Throughout the following chapters we usually will write the velocity as the sum of these two components and examine the structure or stability of various configurations from a frame that is rotating with the "mean" motion of the fluid. This is accomplished by transforming Euler's equation into the rotating frame of reference with constant angular velocity Ω as follows:

$$(d/dt + \Omega \times)(\mathbf{V} + \Omega \times \mathbf{X}) = -\nabla(H + \Phi) \ . \tag{2.10}$$

Here the following standard vector transformations have been applied:

$$d/dt \rightarrow d/dt + \Omega \times \ , \tag{2.11}$$

$$\mathbf{V} \rightarrow \mathbf{V} + \Omega \times \mathbf{X} \ , \tag{2.12}$$

where d/dt, and **V** on the right-hand side refer to the rotating reference frame. The resulting equation is further simplified with the following two vector differential identities:

$$\frac{d}{dt} = \frac{\partial}{\partial t} + \mathbf{V} \cdot \nabla \ , \tag{2.13}$$

and

$$(\mathbf{V} \cdot \nabla)\mathbf{V} = \frac{1}{2}\nabla V^2 + \xi \times \mathbf{V} \ , \tag{2.14}$$

where

$$\xi \equiv \nabla \times \mathbf{V} \tag{2.15}$$

is the vorticity of the fluid. The vorticity is a measure of the local, instantaneous rate of rotation of the fluid in the neighborhood of a given point. Let $\mathbf{V}_I = \mathbf{V}_R + \Omega \times \mathbf{X}$, where V_I and V_R are the velocities in the inertial and rotating frame respectively. Then the following relations hold:

$$\nabla \times \mathbf{V}_I = \nabla \times \mathbf{V}_R + \nabla \times (\Omega \times \mathbf{X}) = \xi + 2\Omega \ , \tag{2.16}$$

where the second summation term has been evaluated using the known vector differential identities. If the fluid is rotating with a fixed angular velocity of $\Omega = 1/2\ \nabla \times \mathbf{V}_I$ in a neighborhood around a given point, then the vorticity $\xi = 0$ at that point

and the fluid is irrotational. Hence, we may interpret the vorticity at any point as twice the local angular velocity at that point. Throughout the derivations we have set $\partial/\partial t = 0$, since we are only interested in the steady-state systems.

After carrying out the multiplication and collecting terms, in the rotating frame of reference Euler's equation assumes the following form:

$$(\xi + 2\Omega) \times \mathbf{V} = -\nabla(H + \Phi + \frac{1}{2}V^2 - \frac{1}{2}\Omega^2 R^2). \tag{2.17}$$

where R is the cylindrical radius.

2.5 The Equation of Continuity

During the course of the fluid motion, the mass of the fluid must be conserved. This constraint will provide a relation between the fluid density and the fluid velocity in the form of the Continuity Equation:

$$\nabla \cdot (\rho \mathbf{V}) = 0 , \tag{2.18}$$

where $\partial/\partial t = 0$ for steady state systems. (For a derivation of the EOC, see Chapter 1 of Landau & Litshitz 1987).

2.6 The Equation of State

As the fluid elements move along their trajectories they may expand or contract due to pressure acted on by the neighboring volume elements. As a result, the density of the fluid will change accordingly. The amount of change in the density in general depends on pressure, temperature and the chemical composition of the fluid. As was mentioned in the introduction, we will consider only barotropic systems where the pressure depends on density alone: $P = P(\rho)$. In particular, we choose a

polytropic equation of state in which the following relation between density and pressure is satisfied:

$$P = K\rho^{1+1/n}, n \geq 0 \tag{2.19}$$

where K and n are the polytropic constant and polytropic index respectively. When n = 0, the fluid is incompressible. Higher n values correspond to higher degrees of compressibility.

With this choice of the polytropic equation of state, we may obtain a relationship between density ρ and enthalpy H via eq. (2.4), namely,

$$\rho = \left[\frac{H}{K(1+n)}\right]^n . \tag{2.20}$$

We will utilize this expression for density in chapter 4 when we develop a new computational method.

Euler's equation and the equation of continuity, along with the Poisson equation and the polytropic equation of state completely determine the motion of ideal self-gravitating compressible fluids. In the subsequent chapters we will seek solutions to these coupled partial differential equations (PDEs) when we construct equilibrium structures of differentially rotating fluids. These equilibrium models are to serve as approximate representations of astronomical gas clouds during their evolutionary history.

2.7 Axisymmetric Euler's Equation

Here we will develop a special version of Euler's equation suited for fluids with axisymmetric flow in the inertial frame of reference. In particular, we consider the case when the velocity is only in the azimuthal direction: $\mathbf{V} = (0, V_\theta, 0)$, and V_θ only depends on R. It is readily verified that the EOC is identically satisfied in the steady-state. We start with the Euler's equation in the inertial frame of reference (eq. 2.6). The left hand side can be transformed to the following using equations 2.13-2.14:

$$\xi \times \mathbf{V} + \frac{1}{2}\nabla V^2 = -\nabla(H+\Phi) \tag{2.21}$$

where, again, the partial time derivative has been set to zero for steady-state systems. Next, we will consider a power-law velocity profile, where the angular velocity $\Omega(R)$ is given by

$$\Omega(R) = \Omega_o(R_o/R)^q \tag{2.22}$$

for different values of the exponents q. In the special case when $q = 3/2$, the flow is "Keplerian", that is, $\Omega(R)$ has the familiar profile of planetary orbits in our solar system. Then the velocity is:

$$\mathbf{V} = \hat{\theta}\, \Omega(R)\, R\,. \tag{2.23}$$

It can be shown that for this choice of the velocity field, the vorticity (eq. 2.15) is given by the expression,

$$\xi = (2 - q)\Omega\, \hat{k}\,. \tag{2.24}$$

Notice that when q = 2 --constant specific angular momentum-- the vorticity is identically zero everywhere. The first term on the left hand side of equation (2.21) can now be calculated by taking the cross product of the above two equations and writing the result in the gradient form:

$$\xi \times \mathbf{V} = -\frac{2-q}{2-2q}\nabla(\Omega^2 R^2)\,. \tag{2.25}$$

Hence all the terms in eq. (2.21) can be written in the form of a gradient. Removing the gradients on both sides will result in the following scalar equation relating the principal physical variables for axisymmetric structures:

$$H+\Phi-\frac{\Omega^2 R^2}{2-2q}=C_I\,, \tag{2.26}$$

when C_I is the integration constant and is determined by applying the boundary condition at suitably chosen points at the surface of the fluid. We will derive solutions of this equation in Chapter 3 when we study the instability modes of the slender, incompressible tori with constant specific angular momentum (q = 2).

CHAPTER 3

STABILITY OF ACCRETION TORI

Models of radially and vertically extended, self-gravitating disks or tori orbiting around a central point-mass potential are relevant to the dynamics of astrophysical systems that are believed to commonly exist in many galaxies.

Papaloizou & Pringle (1984) first discovered a nonaxisymmetric unstable mode (P-mode) in massless slender tori orbiting a central point mass (see also Kojima, 1986 and Frank & Robertson 1988). Self-gravitating slender tori were considered next by Goodman & Narayan (1988; hereafter GN). They found two additional nonaxisymmetric unstable modes — a Jeans-type, or "J", mode and an "I" mode being intermediate between the other two.

Our work (see Andalib, Tohline, Christodoulou, 1997) represents a step in the direction of quantifying the regions of instability in a simple toroidal model of an accretion disk, the slender incompressible self-gravitating torus with constant specific angular momentum (in brief, ICT). This model was studied originally by GN and our investigation is a direct extension of their work. We will map out in a unified manner the three principal unstable modes in this model and compare the derived marginal stability curves against related results previously obtained in different accretion-disk models (simplified two-dimensional and more realistic three-dimensional models) which included the effects of compressibility and different angular momentum distributions. In this way, we can clearly establish the general applicability of the results obtained from the simple ICT model and we can begin

building a quantitative theoretical picture for the appearance of unstable modes. To facilitate such straightforward comparisons in future studies, the results of our work are produced, not only in terms of the standard dimensionless self-gravity parameters (p, ß) which were conveniently used in previous linear stability analyses (GN; Christodoulou & Narayan 1992; Christodoulou 1993, hereafter CN, and C93 respectively), but also in terms of more meaningful global physical quantities, such as the disk-to-central-star mass ratio M_D/M_C and the familiar ratio of the kinetic to gravitational potential energy T/|W| (Tohline & Hachisu 1990; Woodward, Tohline and, Hachisu 1994, hereafter TH, and WTH, respectively). We applied the results from the linear instability analysis with the numerical model constructed with the HSCF. These models are not required to be slender or to have small mass ratios.

3.1 Equilibrium Structure of ICT Models

The equilibrium ICT is composed of an axisymmetric fluid with mass M_D, circular cross-section of radius a, and uniform density ρ orbiting around a point-mass M_C (GN). We adopt cylindrical coordinates (R, ϕ, Z) and we assume that the point-mass is fixed at the origin of the coordinate frame. The center of the cross-section of the torus then lies on the symmetry plane Z = 0 at cylindrical radius R_0. In terms of these quantities, the total mass of the torus is

$$M_D = 2\pi^2 \rho a^2 R_o . \qquad (3.1)$$

The specific (i.e., per unit mass) angular momentum is constant, leading to an angular velocity of the fluid of the form given by eq. (2.22) with q = 2 and with Ω_0 defined as the orbital frequency of fluid residing at location R_0.

In this section, we will leave the parameter q unspecified in order to discuss some general features of the rotation profile (2.22). In later sections, we will concentrate on the constant specific angular momentum case with q = 2. If the ICT is in equilibrium, generally the total angular velocity $\Omega(R)$ will include contributions from the self-gravity of the fluid, as well as from the presence of the central point-mass. The self-gravity of the disk is determined by a solution of the axisymmetric Poisson equation. The central point mass is introduced through the Keplerian angular velocity defined at radius R_o by

$$\Omega_K \equiv \sqrt{\frac{GM_C}{R_0^3}}, \tag{3.2}$$

where G is the gravitational constant.

3.2 Parameterization

For convenience, we define the following dimensionless parameters that characterize this equilibrium model:

$$p_K^2 \equiv \frac{4\pi G\rho}{\Omega_K^2}, \tag{3.3}$$

$$p^2 \equiv \frac{4\pi G\rho}{\Omega_0^2}, \tag{3.4}$$

$$\eta \equiv \left(\frac{\Omega_K}{\Omega_0}\right)^2, \tag{3.5}$$

$$\mu \equiv \frac{1}{2\pi}\left(\frac{M_D}{M_C}\right), \tag{3.6}$$

$$\varepsilon \equiv \frac{a}{R_0}, \tag{3.7}$$

and

$$t \equiv \frac{T}{|W|}\ . \tag{3.8}$$

These parameters are not all independent. For example, detailed force-balance or, equivalently, virial balance specifies a relation between η, μ (or p), and ε; eqs. (3.3)-(3.5) imply that

$$p^2 = \eta p_K^2; \tag{3.9}$$

and eqs. (3.1), (3.2)-(3.7) imply that

$$\mu = \frac{1}{4} p_K^2 \varepsilon^2 \text{ and } \eta\mu = \frac{1}{4} p^2 \varepsilon^2. \tag{3.10}$$

Also note that in equilibrium, $0 \le t \le 1/2$ and $0 \le p_K$, p, $\mu \le \infty$. The aspect ratio ε can be used as a typical expansion variable in analytic calculations (GN; CN). For example, in the (zeroth-order) narrow-torus approximation, $\varepsilon \to 0$. This approximation is further discussed in § 3.7 below. The self-gravity parameter η lies in the interval $0 \le \eta \le 1 + 0(\varepsilon^2)$ and is similar to the corresponding parameter used by CN and C93 and denoted there by the symbol η_*. Here, however, η is defined at the geometric center of the meridional cross-section of the torus R_o and not at the pressure maximum R_*. Because $\eta \propto R$ in all ICT models with $M_C \neq 0$ and because

the geometric center lies to the right of the pressure maximum ($R_o > R_\bullet$), η can take values larger than 1 in our case despite the fact that $\eta_\bullet \leq 1$. This occurs only when deviations of order ε^2 are considered and only at low mass ratios (typically when $\mu << \varepsilon^2$), where $\eta_\bullet \approx 1$ at the pressure maximum.

3.3 Equilibrium Enthalpy

We begin with the scalar Euler's equation (SEE) for axisymmetric systems, eq. (2.26). The total gravitational potential is given by eq. (2.7). The gravitational potential due to the point-mass is given by the eq. (2.9). The potential due to self-gravity has been determined to second-order accuracy in the parameter ε by Dyson (1893). Defining a new radial coordinate r measured on the meridional plane from the center of the cross-section of the torus, denoting the angle between the meridional position vector r and the R-axis by θ, and letting $x \equiv R - R_0 \equiv -r\cos\theta$ with $|x| \leq a$, Dyson's result can be written as

$$\Phi_D = -\frac{GM_D}{\pi R_o}\left[L + \frac{1}{2}\left(1 - \frac{r^2}{a^2}\right) + \frac{1}{2}\varepsilon\left(L - 1 - \frac{r^2}{4a^2}\right)\frac{r}{a}\cos\theta + \frac{1}{16}\varepsilon^2\Phi_D^{(2)}\right] \quad (3.11)$$

where

$$L \equiv \ln\left(\frac{8}{\varepsilon}\right), \quad (3.12)$$

and

$$\Phi_D^{(2)} \equiv \frac{1}{4} - L + 2(L-1)\frac{r^2}{a^2} - \frac{3}{4}\frac{r^4}{a^4} + \left[3\left(L - \frac{5}{4}\right) - \frac{5}{6}\frac{r^2}{a^2}\right]\frac{r^2}{a^2}\cos 2\theta \,. \quad (3.13)$$

Ostriker (1964) has also presented and used this result but he defined the term r cosθ with the opposite sign compared to Dyson (1893). The expressions given above also correct a typographical error in Ostriker's equation (80). Equation (3.11) limits our analysis to at most second-order accuracy in ε but this is not a serious limitation since, in what follows, we are primarily interested in second or lower orders.

Expanding the SEE to order ε^2, applying the boundary condition H(r = a) = 0 and using eqs. (3.2), (3.5), and (3.6), we determine the integration constant C_I as

$$-\frac{C_I}{\Omega_K^2 R_0^2}=1-\frac{\varepsilon^2}{2}+\frac{1}{2\eta(1-q)}+2\left[L\left(1-\frac{\varepsilon^2}{8}\right)+\frac{25}{192}\varepsilon^2\right]\mu$$
$$+\varepsilon\frac{x}{a}\left[\frac{1}{\eta}-1-\left(L-\frac{5}{4}\right)\mu\right] \qquad (3.14)$$
$$+\frac{1}{2}\varepsilon^2\frac{x^2}{a^2}\left[3+\frac{1-2q}{\eta}+\frac{3}{2}\left(L-\frac{55}{36}\right)\mu\right].$$

Clearly, C_I is a constant (independent of powers of x) to order ε^2 only if the last two terms are zero, i.e., only if

$$\frac{1}{\eta}=1+\left(L-\frac{5}{4}\right)\mu, \qquad (3.15)$$

and if the rotation index q is allowed to take values different than 2 as specified by the constraint

$$q=\frac{1}{2}\left\{1+3\eta\left[1+\frac{1}{2}\left(L-\frac{55}{36}\right)\mu\right]\right\}. \qquad (3.16)$$

Using above equation (3.11) - (3.16), we find that the equilibrium enthalpy is given to order ε^2 by the equation

$$H=\frac{1}{2}\left[\Omega_K^2+2\pi G\rho\left(1-\frac{1}{4}\varepsilon\frac{x}{a}+\frac{1}{8}\varepsilon^2 H^{(2)}\right)\right]\left(a^2-r^2\right), \tag{3.17}$$

where

$$H^{(2)}\equiv L-\frac{11}{6}+\frac{5}{3}\frac{x^2}{a^2}-\frac{1}{12}\frac{r^2}{a^2}. \tag{3.18}$$

Equation (3.17) shows that the enthalpy is the sum of two separate contributions, one due to the presence of the central point-mass and another due to the presence of mass in the torus. We shall refer to these two contributions as the "external" and the "internal" enthalpy, respectively.

We also note that the constraint imposed by eq. (3.15) along with eqs. (3.5) and (3.6) provides a "zeroth-order" relation between Ω_0 and Ω_K that takes into account a nonzero torus mass. Not unexpectedly, if $M_D \neq 0$, then Ω_0 shifts to a value that is larger than the Keplerian value Ω_K, i.e.

$$\Omega_0=\Omega_K\sqrt{1+\frac{1}{2\pi}\left(L-\frac{5}{4}\right)\frac{M_D}{M_C}}\ . \tag{3.19}$$

Combined with the equations of § 3.2, eq. (3.15) also provides another important zeroth-order relation, i.e.

$$\frac{\Omega_0^2}{2\pi G\rho}=\frac{\varepsilon^2}{2\eta\mu}=\frac{2}{p^2}=\frac{1}{2}\varepsilon^2\left(L-\frac{5}{4}+\frac{1}{\mu}\right). \tag{3.20}$$

This is precisely the relation derived by Ostriker (1964; eqs. [105] and [111]) for incompressible tori and, in the limit of $\mu \to \infty$ (i.e., $M_C = 0$), it reduces to the corresponding expressions derived by Dyson (1893) and Wong (1974).

3.4 Properties of the Equilibrium Model

The above second-order accurate equilibrium enthalpy distribution is limited by the requirement that the rotation index q vary in a specific manner (see eq. [3.16]). Thus, it cannot be generally used to describe all the $q = 2$ ICT models of interest with varying mass ratios, aspect ratios, etc. (It is only in the special case of a torus with $\mu = 0$ and $\eta = 1$ that eq. [3.16] leads to $q = 2$.) Nevertheless, it is worth mentioning some interesting features of this type of equilibrium solution before we proceed to analyze lower-order solutions.

Notice from eq. (3.17) that, although the $H = 0$ meridional contour is a circle of radius a centered at R_0, the pressure/enthalpy maximum does not occur at $R = R_0$ but is offset in the radial direction. The exact location of this maximum can be found by letting $Z = 0$ (i.e., $r = x$) and by solving the resulting cubic equation $dH/dx = 0$ for x. Such equilibrium models are unusual because the internal pinching structure of their equipressure surfaces is in marked contrast with the regularity exhibited by the outer $P = 0$ circular surface.

We have checked that such models do indeed exist for various q-values in the interval $1 < q < 2$, as determined by eqs. (3.15) and (3.16). We have constructed numerically incompressible tori in equilibrium around a central point-mass using the

HSCF method and an R-Z grid with 256 x 256 equally spaced zones. As M_D/M_C is varied between 0.01 and 100 in these models and as η is arbitrarily chosen between 0.08 and 0.2, P_K varies from 1 to 40; p is between 1 and 6.5; η is between 1 and 0; and t varies from 0.5 to 0.3. The equilibrium parameters of twelve characteristic models are listed in Table 1, where the analytically predicted values are shown in parentheses. The agreement between the parameter values predicted by the equations of §§ 3.2-3.3 and by the HSCF computer code, respectively, is good despite the fact that the ε–values are substantially larger than zero. The small disagreement seen in the η– and the t-values is the result of using the zeroth-order accurate eq. (3.15). As will be seen below, the next correction term in the $1/\eta$ expansion is of order ε^2 and is always negative. Therefore, eq. (3.15) underestimates η consistently and, since $t \propto 1/\eta$ (see eq. [3.28] below), the tabulated analytical t-values are consistently larger than the HSCF values. In the interval $0.05 \leq M_D/M_C \leq 2$, the tabulated t-values are overestimated by ≤ 0.01 (i.e., by $\lesssim 2\%$) in the zeroth-order analytic calculation.

Retaining terms up to only order ε (or lower) in eq. (3.17) allows us to discard the constraint expressed by eq. (3.16) and to set q = 2 exactly. The external enthalpy is then symmetric about R_0, i.e.

$$H_{ex} = \frac{1}{2}\Omega_K^2 a^2 \left(1 - \frac{r^2}{a^2}\right), \tag{3.21}$$

and the internal enthalpy is given by the expression

$$H_{in} = \pi G \rho a^2 \Omega_K^2 \left(1 - \frac{1}{4}\varepsilon \frac{x}{a}\right)\left(1 - \frac{r^2}{a^2}\right), \tag{3.22}$$

where, equivalently, $\pi G \rho a^2 = GM_D/(2\pi R_0)$. The total enthalpy is, of course, the sum of the two contributions, i.e., $H = H_{cx} + H_{in}$. The properties of this solution have also been discussed by Ostriker (1964).

Although the $H = 0$ surface presents a circular cross-section centered at R_0, the enthalpy maximum of the torus does not lie at R_0 but at

$$R_* \equiv R_0 \left[1 - \frac{\varepsilon^2}{8}\left(1 + \frac{2}{p_K^2}\right)^{-1}\right], \tag{3.23}$$

to second order in ε. Furthermore, the equipressure surfaces do not form nested contours concentric with the outer $P = 0$ surface. To more clearly identify the deviation caused by the presence of the internal enthalpy, we cast eq. (3.22) in the form

$$H_{in} = \frac{GM_D}{2\pi R_0}\left[1 - \frac{(x - x_*)^2 + Z^2}{a^2}\right], \tag{3.24}$$

where

$$\frac{x_*}{a} = -\frac{1}{8}\varepsilon\left(1 - \frac{r_{H_{in}}^2}{a^2}\right), \tag{3.25}$$

and $r_{H_{in}}$ is the meridional circular radius defined by any value of the internal enthalpy H_{in}. Thus, the surfaces of equal internal enthalpy are circular but, except for the $H_{in} = 0$ surface itself, the center of each circle (as well as the internal enthalpy maximum)

is slightly offset from R_0. In general, eq. (3.24) prescribes the amount by which each circular meridional cross-section is offset from R_0 as a function of H_{in}. Hence, to order ε^2 and in the absence of a point-mass, equipressure surfaces have circular cross-sections of radius $r_{H_{in}}$ and centers at Z = 0, R = R_0 + x_*. As $r_{H_{in}} \to 0$, the pressure peaks at R = $R_0(1 - \varepsilon^2/8)$. At the other extreme, as $r_{H_{in}} \to a$, the pressure vanishes at the outer circular surface which is centered at R = R_0. In general, the equipressure surfaces depend on the relative values of M_C and M_D. When the contribution from either mass is dominant, the corresponding equipressure surfaces are either nearly centered at R_0 (if $M_D << M_C$) or offset from R_0 (if $M_D >> M_C$; see eq. [3.25]). When the two masses are comparable, the equipressure surfaces are formed by a linear superposition of the two kinds of circular cross-sections, as described by eqs. (3.21) and (3.24); and the location of the total enthalpy maximum is given by eq. (3.23).

The leading terms in eq. (3.17) give the zeroth-order enthalpy distribution

$$H=\frac{1}{2}\Omega_K^2 a^2\left(1+\frac{1}{2}p_K^2\right)\left(1-\frac{r^2}{a^2}\right), \tag{3.26}$$

with p_K defined by eq. (3.3). This expression is similar to that derived by GN (see, e.g., their eq. [2.23]) except that the frequency Ω_K appears here in place of Ω_0 both explicitly and implicitly in the definition of the self-gravity parameter p_K. This highlights a key difference between our derivation and the one presented by GN. In deriving eqs. (3.17) and (3.26), we have kept the two frequencies Ω_K and Ω_0 distinct

from one another whereas GN implicitly assumed that, independent of the mass of the torus, $\Omega_K = \Omega_0$ (i.e., that $\eta = 1$).

It is evident from eq. (3.15) or eq. (3.19) that the two frequencies are equal only in the limit of vanishing mass ratio, i.e., when $\mu = 0$ resulting in $\eta = 1$ (and in $p = p_K$ as well). In general, since we are interested in systems with $\mu \neq 0$, the choice $\Omega_K = \Omega_0$ is not appropriate because it eliminates from consideration a large variety of models with tori of nonzero mass. This point has also been discussed by CN and C93. In what follows, we will continue to maintain a clear distinction between the two frequencies Ω_0 and Ω_K as well as between the two associated self-gravity parameters p and p_K.

3.5 Global Physical Quantities

In the P&P (1984) analysis of zero-mass tori, a single dimensionless parameter – the aspect ratio ε–was sufficient to uniquely define the structure of the equilibrium models. In extending this analysis to tori with nonzero mass, GN utilized a second dimensionless parameter, p, that measures the relative importance of self-gravity. Finally, CN introduced in their analysis an additional self-gravity parameter, η, with the understanding that ε, p, and η are not completely independent but related in equilibrium. In an attempt to relate the results of these studies to a broader range of accretion-disk systems, we wish to utilize an alternative pair of dimensionless parameters, the mass ratio $M_D/M_C = 2\pi\mu$ (eq. 3.6) and the energy ratio t (eq. 3.8), which also define each self-gravitating equilibrium model, but in a way that is

physically more relevant and more easily understood. To do that, we need to develop an accurate set of equations mapping the older pair of parameters to the new one.

The mass ratio M_D/M_C can be easily related to the parameters p or p_K and from eqs. (3.6) and (3.10), i.e.

$$\frac{M_D}{M_C}=\frac{\pi}{2}p_K^2\varepsilon^2=\frac{\pi}{2\eta}p^2\varepsilon^2. \tag{3.27}$$

An expression for the energy ratio t is found by direct integrations that determine the rotational kinetic energy T and the gravitational potential energy W to order ε^2 (see also Dyson 1893 and Ostriker 1964), i.e.

$$t=\frac{T}{|W|}=\frac{1}{2\eta}\frac{1+\frac{1}{4}(q-1)(2q-3)\varepsilon^2}{1+(L+\frac{1}{4})\mu-\frac{1}{8}[1+(L-\frac{2}{3})\mu]\varepsilon^2}. \tag{3.28}$$

Eq. (3.15) is not sufficiently accurate to be used for the elimination of the parameter η from eqs. (3.27) and (3.28). Specifically, eq. (3.15) breaks down in the limit of small torus mass ($\mu \rightarrow 0$) when the μ-dependent term becomes comparable to the $0(\varepsilon^2)$ term that was not accounted for to the order of the derivation in § 3.3 which led to eq. (3.15) and to the parenthetical results listed in Table 1. For this reason, we proceed to establish a relation between η, μ, and ε that is more accurate than eq. (3.15) and that is valid over a wide interval of mass ratios and aspect ratios. Such a relation is provided at the geometric center of the meridional cross-section by the virial theorem,

TABLE 1
EQUILIBRIUM INCOMPRESSIBLE CIRCULAR TORI

M_D/M_C	ε	q	p_K	p	η	t
0.01	0.080	1.996	0.994 (0.993)	0.994 (0.990)	1.000 (0.995)	0.497 (0.499)
0.05	0.135	1.982	1.319 (1.326)	1.316 (1.311)	0.995 (0.978)	0.488 (0.494)
0.10	0.161	1.966	1.547 (1.565)	1.534 (1.533)	0.984 (0.959)	0.480 (0.489)
0.50	0.184	1.861	3.038 (3.066)	2.815 (2.798)	0.859 (0.833)	0.445 (0.455)
1.00	0.195	1.765	4.057 (4.099)	3.488 (3.474)	0.739 (0.718	0.418 (0.427)
2.00	0.201	1.635	5.608 (5.628)	4.272 (4.224)	0.580 (0.563)	0.385 (0.394)
3.00	0.195	1.549	7.012 (7.100)	4.789 (4.811)	0.466 (0.459)	0.373 (0.376)
5.00	0.190	1.446	9.360 (9.413)	5.448 (5.450)	0.339 (0.335)	0.355 (0.357)
10.0	0.195	1.335	12.80 (12.96)	5.789 (5.841)	0.205 (0.203)	0.336 (0.337)
20.0	0.184	1.260	19.16 (19.39)	6.411 (6.453)	0.112 (0.111)	0.326 (0.327)
50.0	0.202	1.206	27.84 (28.00)	6.188 (6.207)	0.049 (0.049)	0.315 (0.315)
100.	0.202	1.186	39.38 (39.60)	6.265 (6.284)	0.025 (0.025)	0.312 (0.312)

NOTE: The parenthetical values of t were determined analytically from the zeroth-order form of eq. (3.28). All the other analytic values were determined from the equations of §§ 3.2 - 3.3

$$2T + W + 3\Pi = 0\,, \tag{3.29}$$

after the internal energy $\Pi \equiv \int H\, dM$ (where dM is the mass element) is calculated from the second-order accurate equilibrium enthalpy distribution discussed in § 3.3 (eq 3.17). Performing the calculations with q = 2, we find that the condition of virial balance (eq. 3.29) demands that

$$\frac{1}{\eta}=1+\left(L-\frac{5}{4}\right)\mu-\frac{9}{8}\left[1+\frac{1}{2}\left(L-\frac{145}{108}\right)\mu\right]\varepsilon^2+O\left(\mu\varepsilon^2\right), \tag{3.30}$$

an expression that should be contrasted to eq. (3.15) above. Note that, in the limit of $\mu \rightarrow \infty$, $\eta \rightarrow 0$ irrespective of the value of ε. In the opposite limit of $\mu << \varepsilon^2$, this equation shows that η can be somewhat larger than one.

Eliminating η between eq. (3.28) with q = 2 and eq. (3.1), we obtain the expression

$$t=\frac{1}{2}\frac{1+\left(L-\frac{5}{4}\right)\mu-\frac{7}{8}\left[1+\frac{5}{14}\left(L-\frac{17}{12}\right)\mu\right]\varepsilon^2}{1+\left(L+\frac{1}{4}\right)\mu-\frac{1}{8}\left[1+\left(L-\frac{2}{3}\right)\mu\right]\varepsilon^2}+O\left(\mu\varepsilon^2\right) \tag{3.31}$$

We can now distinguish the following limiting cases:

Case (a) If $\varepsilon^2 << \mu$ and μ is small, then eq. (3.31) reduces to

$$t=\frac{1}{2}\frac{1+\left(L-\frac{5}{4}\right)\mu}{1+\left(L+\frac{1}{4}\right)\mu}\approx\frac{1}{2}\left(1-\frac{3}{2}\mu\right); \tag{3.32}$$

Case (b) If $\mu << \varepsilon^2$ (or if $M_D \rightarrow 0$) and ε is small, then eq. (3.32) reduces to

$$t=\frac{1}{2}\frac{1-\frac{7}{8}\varepsilon^2}{1-\frac{1}{8}\varepsilon^2}\approx\frac{1}{2}\left(1-\frac{3}{4}\varepsilon^2\right); \tag{3.33}$$

Case (c) In the intermediate regime where $\mu \sim \varepsilon^2$ and if μ, ε are small, eq. (3.31) reduces to

$$t=\frac{1}{2}\left[1-\frac{3}{4}\left(\varepsilon^2+2\mu\right)\right]; \tag{3.34}$$

Case (d) In the absence of a central point-mass ($M_C = 0$, $\mu \rightarrow \infty$) and if ε is small, eq. (3.31) reduces to

$$t=\frac{1}{2}\frac{\left(L-\frac{5}{4}\right)-\frac{5}{16}\left(L-\frac{17}{12}\right)\varepsilon^2}{\left(L-\frac{1}{4}\right)-\frac{1}{8}\left(L-\frac{2}{3}\right)\varepsilon^2}. \tag{3.35}$$

Note that, in cases (b) and (d) with $M_D = 0$ and $M_C = 0$, respectively, $t \rightarrow 1/2$ as $\varepsilon \rightarrow 0$.

3.6 Comparison with Numerical ICT Models

We have checked the accuracy and validity of the above-described transformation (eqs. [3.27], [3.30], and [3.31]) by using again the HSCF method (and again an R-Z grid resolution of 256×256 equally spaced zones) to numerically construct detailed-force-balance ICT models with various mass ratios and aspect ratios. Although the rotation index was fixed to the value $q = 2$, these models were not constrained to have perfectly circular cross-sections, nor were they confined to the regime where ε is small.

In the HSCF method, it is convenient to adopt units such that $G = \rho = R_+ = 1$, where R_+ is the outer equatorial radius of the torus. The code solves iteratively eq. 2.26 for which the potential Φ_D due to self-gravity is provided by a numerical solution of the axisymmetric Poisson equation and $\Omega(R)$, Φ_C are specified by eqs. 2.22, 2.9, respectively (see Hachisu [1986] for more details). Two free parameters, M_D/M_C and the inner equatorial radius R_-, are chosen before the start of the iteration cycle and are kept constant throughout the computation of a specific model. After the code has converged to an equilibrium structure, characteristic values of all the relevant parameters of the model (i.e., ε, p_K, p, η and t) can be readily computed as follows. Because the meridional cross-sections are generally not circular, the aspect ratio ε is not precisely defined; an effective ε-value is determined for each numerical model through the equation $\varepsilon_{eff} = a'/R_0$ by computing the equivalent radius a' of a circular torus centered at R_0 and having the same surface area and volume as the torus of the converged ICT model. For convenience, then, all parameters are computed using these values of ε_{eff} and R_0.

A comparison between numerical and analytic results for ICT models with $0.01 \leq M_D/M_C \leq 100$ is shown in Table 2. The analytically determined parameters are listed in parentheses. The agreement between results is good in the range of $\varepsilon_{eff} \lesssim 0.3$ and continues to hold even for models with $\varepsilon_{eff} \approx 0.4$. For $\varepsilon_{eff} < 0.4$, the difference between numerical and analytic results in the tabulated t-values is < 2%

TABLE 2
EQUILIBRIUM ICT MODELS WITH q = 2

M_D/M_C	ε_{eff}	p_K		p		η		t	
0.01 ...	0.070	1.135	(1.135)	1.135	(1.135)	1.000	(1.000)	0.497	(0.497)
	0.106	0.753	(0.753)	0.756	(0.756)	1.008	(1.008)	0.495	(0.495)
	0.145	0.549	(0.549)	0.555	(0.555)	1.020	(1.020)	0.491	(0.491)
0.10 ...	0.074	3.428	(3.428)	3.346	(3.348)	0.953	(0.954)	0.487	(0.487)
	0.112	2.258	(2.258)	2.223	(2.221)	0.970	(0.967)	0.484	(0.484)
	0.164	1.536	(1.536)	1.528	(1.528)	0.990	(0.989)	0.479	(0.479)
	0.224	1.128	(1.128)	1.140	(1.140)	1.021	(1.021)	0.470	(0.471)
0.50 ...	0.074	7.616	(7.616)	6.774	(6.768)	0.791	(0.790)	0.455	(0.456)
	0.113	4.972	(4.972)	4.498	(4.496)	0.818	(0.818)	0.452	(0.452)
	0.196	2.874	(2.874)	2.686	(2.682)	0.873	(0.871)	0.441	(0.443)
	0.259	2.180	(2.180)	2.090	(2.086)	0.919	(0.916)	0.431	(0.433)
	0.320	1.760	(1.760)	1.738	(1.732)	0.975	(0.969)	0.417	(0.421)
	0.391	1.441	(1.441)	1.480	(1.473)	1.054	(1.045)	0.399	(0.404)
1.00 ...	0.074	10.77	(10.77)	8.698	(8.683)	0.652	(0.650)	0.431	(0.432)
	0.167	4.766	(4.766)	4.069	(4.059)	0.729	(0.725)	0.419	(0.421)
	0.216	3.702	(3.702)	3.238	(3.229)	0.765	(0.761)	0.411	(0.414)
	0.297	2.690	(2.690)	2.458	(2.445)	0.835	(0.826)	0.395	(0.400)
	0.334	2.390	(2.390)	2.232	(2.216)	0.872	(0.860)	0.386	(0.393)
	0.372	2.142	(2.142)	2.046	(2.032)	0.912	(0.899)	0.377	(0.384)
	0.421	1.894	(1.894)	1.867	(1.853)	0.971	(0.957)	0.364	(0.372)
2.00 ...	0.074	15.23	(15.23)	10.61	(10.55)	0.485	(0.480)	0.404	(0.406)
	0.167	6.746	(6.746)	5.061	(5.043)	0.563	(0.559)	0.388	(0.391)
	0.300	3.764	(3.764)	3.085	(3.058)	0.672	(0.660)	0.361	(0.369)
	0.423	2.669	(2.669)	2.386	(2.354)	0.799	(0.778)	0.330	(0.342)
	0.507	2.224	(2.224)	2.126	(2.097)	0.914	(0.889)	0.305	(0.320)
10.0 ...	0.074	34.06	(34.06)	13.48	(13.42)	0.157	(0.155)	0.362	(0.364)
	0.168	15.04	(15.04)	6.722	(6.683)	0.200	(0.197)	0.335	(0.339)
	0.305	8.279	(8.279)	4.244	(4.167)	0.263	(0.253)	0.297	(0.309)
	0.436	5.787	(5.787)	3.337	(3.255)	0.338	(0.316)	0.260	(0.282)
100.....	0.074	107.7	(107.7)	14.54	(14.46)	0.018	(0.018)	0.346	(0.349)
	0.168	47.49	(47.49)	7.376	(7.335)	0.024	(0.024)	0.315	(0.318)
	0.306	26.12	(26.12)	4.779	(4.663)	0.033	(0.032)	0.270	(0.285)
	0.441	18.08	(18.08)	3.863	(3.668)	0.046	(0.041)	0.228	(0.255)

for $M_D/M_C \leq 1$, $\leq 4\%$ for $M_D/M_C \leq 10$, and $< 6\%$ for $M_D/M_C \leq 100$. For $\varepsilon_{cff} > 0.4$, this difference is $< 2.2\%$ for $M_D/M_C = 1$, $< 8.5\%$ for $M_D/M_C \leq 10$, and $< 12\%$ for $M_D/M_C \leq 100$.

3.7 The Narrow-Torus Approximation

Linear stability analysis in the zeroth-order narrow-torus ($\varepsilon \rightarrow 0$) approximation has been performed by GN in the limit of $\eta = 1$ (i.e., $\Omega_0 = \Omega_K$). Based on the descriptions of the equilibrium models presented in § 3.1 above, we extend the GN analysis to models with $\eta \neq 1$. For this purpose, we use the computer code developed by J. Goodman but we introduce the self-gravity parameter η in the linear analysis via the equilibrium enthalpy distribution (combine eqs. 3.5, 3.9, and 3.26)

$$H=\frac{1}{2}\Omega_0^2 a^2\left(\eta+\frac{1}{2}p^2\right)\left(1-\frac{r^2}{a^2}\right). \tag{3.36}$$

The standard linearized equations and the numerical techniques have been described in detail by GN. Here we briefly repeat the main points in order to show how the same set of equations and the same code can be efficiently used to obtain results on the stability of ICT ($q = 2$) models with $\Omega_0 \neq \Omega_K$ and various mass ratios.

Despite the prominence of the frequency Ω_K in the description of § 3.4, the stability analysis is performed in a reference frame that rotates with frequency Ω_0 about the Z-axis. Linearizing to zeroth-order the three components of the equation of motion, the continuity equation, and the Poisson equation, we seek nonaxisymmetric normal modes of the general form

$$f'(x,y,z,\tau) = f'(x,z) \exp(iky - i\omega\tau), \tag{3.37}$$

where f' denotes any perturbed variable, $x \equiv R - R_o$, $y \equiv R_o \phi$, $z \equiv Z$ and τ is the time. (Note, however, that GN use the definition $x = + r \cos\theta$ which differs in the sign from the definition in § 3.3. Since the linear analysis is performed to zeroth order in ε, this difference does not affect the equilibrium enthalpy.) The azimuthal wavenumber is defined by $k \equiv m/R_o$ (where $m \geq 2$ is an integer) and ω represents the generally complex eigenfrequency ($\mathrm{Im}[\omega] > 0$ for exponentially growing, unstable modes).

It is convenient to define the dimensionless wavenumber

$$ß \equiv ka \equiv m\varepsilon, \tag{3.38}$$

the dimensionless eigenfrequency

$$\nu \equiv \frac{\omega}{\Omega_0}, \tag{3.39}$$

and the dimensionless Doppler-shifted frequency of a pattern as seen by the unperturbed fluid at position x, i.e.

$$\sigma \equiv \frac{\omega + 2\Omega_0 kx}{\Omega_0} = \nu + 2\beta\frac{x}{a}, \tag{3.40}$$

that effectively defines the location (x-value) of corotation for each mode through the equation $\mathrm{Re}[\sigma] = 0$.

As noted earlier (see § 2.7), the vorticity of the ICT vanishes in equilibrium. Thus, only nonvortical modes are physically relevant in the sense that vortical

modes are necessarily neutral. For nonvortical modes, the perturbed velocity profile v' derives from a velocity potential ψ', i.e.

$$v' = \nabla\psi' \tag{3.41}$$

which satisfies Laplace's equation $\nabla^2\psi' = 0$. The perturbed potentials are related through the equation (see GN for more details)

$$H' = i\sigma\psi' - \Phi', \tag{3.42}$$

where H' and Φ' are the perturbed enthalpy and self-gravitational potential, respectively. In our linear analysis, we normalize all the dynamical variables in terms of the quantities Ω_0 and a. With the help of eq. (3.42) and of the equilibrium expression (3.36) and defining $\xi \equiv x/a$, the boundary condition that $H' = 0$ at the perturbed surface of the model can be written in the form

$$\sigma^2\psi' + i\sigma\Phi' - \left(\eta + \frac{1}{2}p^2\right)\frac{\partial\psi'}{\partial\xi} = 0 \quad \text{at } \xi = 1, \tag{3.43}$$

i.e., at the unperturbed boundary of the equilibrium torus. The discontinuity in the normal derivative of Φ' also leads to a condition that applies to the unperturbed boundary of the torus, i.e.

$$\left(\left.\frac{\partial\Phi'}{\partial\xi}\right|_{\xi=1^+} - \left.\frac{\partial\Phi'}{\partial\xi}\right|_{\xi=1^-}\right) + \frac{p^2}{\eta + \frac{1}{2}p^2}(\Phi' - i\sigma\psi') = 0 \quad \text{at } \xi = 1. \tag{3.44}$$

For any choice of the input parameters p, η, and ß, eqs. (3.43) and (3.44) are solved numerically in Goodman's code by direct expansions of the variables ψ' and Φ' in series of modified Bessel functions; the eigenfrequencies v and the associated

eigenfunctions ψ' and Φ' are all determined self-consistently in the output. Note that, when choosing p and η independently, the value of ε is no longer a free parameter (see, e.g., eq. [3.30]). In turn, the ε–value obtained by equilibrium requirements along with any freely chosen, ß–value specifies uniquely the mode number m via eq. (3.38). We note that the deduced mode numbers can generally take any positive real value, but only integer m-values have physical meaning.

3.8 The Principal Modes of Nonaxisymmetric Instability

The fundamental investigations of the stability of rotating toroidal fluid systems with and without self-gravity (P&P 1984; GGN 1986; GN 1988) have clearly identified three principal Z-symmetric modes of nonaxisymmetric instability. These modes are now known as the P-, I-, and J-modes.

(a) P-modes: These are caused by waves that propagate at the two edges of the torus and that couple across a forbidden region around corotation. The two waves carry equal but opposite in sign amounts of angular momentum. Corotation is always inside the torus and relatively near or at the pressure maximum. The P-modes exist in systems with low degrees of self-gravity (i.e., with low values of the self-gravity parameters p_K and p) and with rotation profiles characterized by a rotation index in the range $\sqrt{3} \leq q \leq 2$. Such modes become weaker with increasing self-gravity and disappear altogether at considerably low values of M_D/M_C.

As the self-gravity of the torus is increased, two new modes of instability appear. These modes were first identified by Maxwell (1859) in a study of the

stability of the rings of planet Saturn. The I-modes generally appear before the J-modes, at lower degrees of self-gravity (see GN; CN; C93; Christodoulou et al. 1995a, b). This observation led Maxwell to discard the J-modes and to concentrate on the I-modes in his investigation of the low-mass rings around Saturn.

(b) I-modes: These are caused by a merger of two disturbances carrying equal but opposite in sign amounts of angular momentum. One disturbance corresponds to free epicyclic waves with high frequencies in the rotating frame while the other disturbance is driven by self-gravity and represents azimuthal compressive motions that nearly corotate with the fluid. Corotation for the I-modes usually lies beyond the outer edge of the torus. In fact, these are the only modes possessing this characteristic property. The I-modes appear first at moderate degrees of self-gravity and persist with increasing self-gravity all the way into the regime where the J-modes also appear.

(c) J-modes: These are manifestations of the Jeans instability in a strongly self-gravitating torus in which the fluid tends to break up into separate self-gravitating clumps. The J-modes are also caused by a merger of two disturbances which, however, are both driven by self-gravity and are both nearly corotating with the fluid. Corotation is always inside the torus and relatively near or at the pressure maximum. The J-modes appear and persist only in slender tori dominated by strong self-gravity and are not affected substantially by the absence/presence of a central object with a moderate or reasonably large mass.

In the following two sections, we employ the formulation described in §§ 3.1 and 3.7 to map out in detail the P-, I-, and J-modes of the ICT models in various parameter spaces. We also compare our results to those obtained from previous investigations.

3.9 Regions of Unstable P-, I-, and J-Modes

Combining eqs. 3.10 and 3.30 and solving for p^2, we find that

$$p^2=\frac{4}{\varepsilon^2}\left[\frac{1-\eta\left(1-\frac{9}{8}\varepsilon^2\right)}{\left(L-\frac{5}{4}\right)-\frac{9}{16}\left(L-\frac{145}{108}\right)\varepsilon^2}\right]. \tag{3.45}$$

This relation helps us determine how to select the independent parameters p and η of the various equilibrium ICT models in a meaningful and consistent manner. Equation (3.45) shows that $p^2(\varepsilon)$ attains a minimum for any arbitrary choice of η in the interval $0 \le \eta \le 1$ and that p^2 increases with ε if $\eta > 1$. The minimum p–values and the corresponding values of ε, μ, M_D/M_C, and t are listed in Table 3 for various values of $\eta \le 1$. The same results are also illustrated in Fig. 3.1.

These results effectively determine all the independent p–values, i.e. $p \ge P_{min}$ which are physically relevant for a particular choice of the second independent parameter η. Specifically, they indicate which low p-values should be excluded from consideration after an η–value has been freely chosen. Moreover, the above results indicate that, for every chosen value of $\eta < 1$ and for any chosen value of $P > P_{min}$, there exist two independent equilibrium solutions characterized by different values

of the aspect ratio ε. Hence, for $p > P_{min}$ and for $\eta < 1$, each model specified by the pair of parameters (p, η) corresponds to two distinct systems with different values of ε, M_D/M_C, and $T/|W|$. One of the two corresponding ε–values is quite large for practically all values of η (see Table 3 and Fig. 3.1). The other ε–value is always smaller than the critical ε–value that corresponds to $p = P_{min}$ and, thus, more in accordance with the spirit of the narrow-torus approximation that $\varepsilon << 1$.

We make use of these conclusions in the following sections, where we analyze the stability properties of equilibrium ICT models selected by specifying the two independent parameters p and η.

TABLE 3
MINIMUM P—VALUES AND CORRESPONDING EQUILIBRIUM PARAMETERS FOR A CHOSEN η

η	p_{min}	ε	μ	M_D/M_C	t
0	2.970426	0.826122	∞	∞	0.175858
0.1	2.931156	0.793298	13.517321	84.931831	0.183686
0.2	2.882108	0.760481	6.004913	37.729979	0.192775
0.3	2.822566	0.726876	3.507738	22.039769	0.203482
0.4	2.751191	0.691591	2.262666	14.216749	0.216315
0.5	2.665741	0.653470	1.517251	9.533171	0.232040

TABLE 3 Continued

η	p_{min}	ε	μ	M_D/M_C	t
0.6	2.562459	0.610792	1.020681	6.413128	0.251882
0.7	2.434620	0.560603	0.665297	4.180186	0.277961
0.8	2.268361	0.496779	0.396826	2.493334	0.314439
0.9	2.025217	0.401731	0.183870	1.155291	0.371482
0.9228	1.947049	0.370057	0.140645	0.883698	0.389981
0.95	1.829477	0.321084	0.090804	0.570540	0.416921
0.99	1.508705	0.181087	0.018849	0.118432	0.475235
0.999	1.235467	0.071801	0.001969	0.012373	0.496618
0.9999	1.066305	0.026485	0.000199	0.001253	0.499588
0.999976	0.990303	0.014121	0.000049	0.000307	0.499889
0.999990	0.949263	0.009420	0.000020	0.000126	0.499952
0.999999	0.862475	0.003279	0.000002	0.000013	0.499994
1	0	0	0	0	0.5

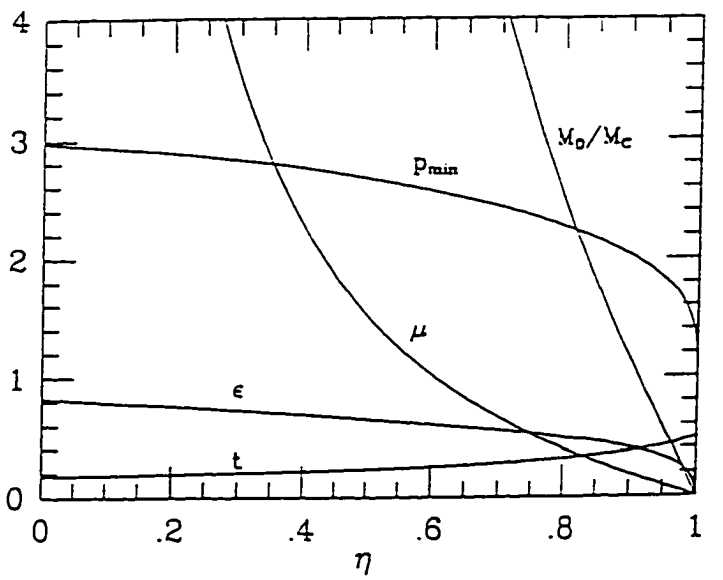

Fig. 3.1— The minimum values p_{min} and the corresponding values of ε,μ, M_D/M_C, and t are plotted as functions of η in the interval $0 \leq \eta \leq 1$.

3.10 The P-modes

Linear analysis shows that the P-modes exist in all models with $p \leq 0.990303$ and $\eta = 1$. As η is decreased toward zero, the maximum critical value $p \equiv p_{max}$ also decreases toward zero. Specifically, $p_{max} = 0.908$, 0.746, 0.582, 0.408, and 0.201 for $\eta = 0\,9$, 0.7, 0.5, 0.3, and 0.1, respectively. Also, as η is increased above one, the P-modes still exist in the (p, η)–plane. However, our calculations indicate that the region of physically important P-modes is limited in the narrow interval of

$$0.999976 \leq \eta \leq 1.00003\,. \qquad (3.46)$$

The lower limit is imposed by the requirement that $p_{max} \geq p_{min}$ for any chosen value of $\eta \leq 1$. In other words, the P-modes are physical only in models in which the modes exist for p–values larger than the minimum values determined by eq. (3.45) above. From Table 3, the critical case occurs for $\eta = 0.999976$ where $p_{max} \geq p_{min} = 0.990303$. The upper limit is imposed by the requirement that $\eta_{\bullet} \leq 1$. In other words, the P-modes are physical only in models in which the value of the parameter η at the pressure maximum of the torus, as determined with the help of eq. (3.23), does not exceed unity. Based on these results, we concentrate below on the P-modes in models whose η–values are specified by eq. (3.46), but the first important conclusion of our investigation can readily be obtained from this equation and from the results listed in Table 3: because $\eta \approx 1$ in eq. (3.46), the P-modes are severely

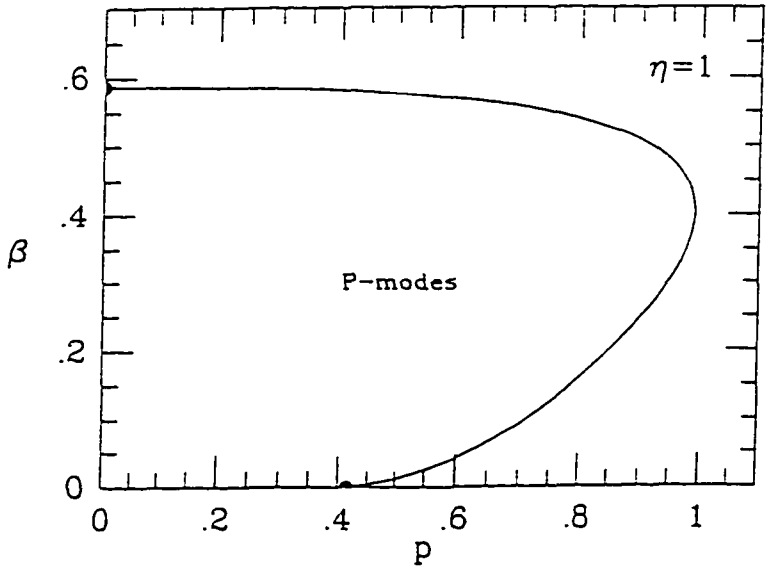

Fig. 3.2.—The region of unstable P-modes in the (p,ß)-plane for $\eta = 1$. The marginal curve is practically indistinguishable for any other value in the narrow interval of $0.999976 \leq \eta \leq 1.00003$ where the P-modes are physically important. The end points of this curve at p = 0.414, ß = 0.001 and at p = 0, ß = 0.588 are marked by solid dots.

restricted to rapidly rotating models with extremely small mass ratios and extremely small aspect ratios (see § 3.10 for details).

As was detailed above, different parts of the instability region shown in Fig. 3.2 are accurate descriptions of P-modes for models with η-values given by eq. (3.46). Our next step is to transform the information derived from linear stability analysis into a set of easier understood equilibrium parameters that characterize unstable ICT models. The simplest and most important such parameters are the aspect ratio ε, the mass ratio M_D/M_C, the energy ratio T/|W|, and the integer mode numbers m of the unstable P-modes. The transformation is achieved with the help of the equations derived in § 3.5, and 3.7 above.

Our results are shown in Table 4, where the derived equilibrium parameters are listed for models with η-values as specified by eq. (3.46). The largest tabulated η-value ($\eta = 1.00003$) is important because it leads to the highest possible mass ratio and aspect ratio ($M_D/M_C = 1.15 \times 10^{-3}$ and $\varepsilon = 0.02733$ for $p = 0.99$ and for only one unstable P-mode with $m = 15$). The rest of the tabulated models with various η-values are shown for comparison purposes. They demonstrate that, when η is decreased below 1.00003, then all unstable models have significantly lower ε and M_D/M_C-values compared to the quoted highest possible values. Also note that according to the discussion of § 3.9, there exist two possible solutions for models with $\eta < 1$. The solutions omitted from Table 4 lead to even lower mass ratios and aspect ratios compared to the tabulated values.

3.11 The I-modes

Linear analysis shows that the I-modes exist in all models with $p \geq p_{min}$ and $\eta \leq 0.9228$. Thus, for $\eta \leq 0.9228$, the results listed in Table 3 and plotted in Fig. 3.1 also represent the critical values $p_{crit} = p_{min}$ where the I-modes disappear with decreasing p (see also Fig. 3.3). For $0.9228 < \eta < 1$, the I-modes disappear at higher critical values $p \equiv p_{crit}$ compared to those listed in Table 3. For example, $p_{crit} = 2.001$ and 2.100 for $\eta = 0.95$ and 1, respectively (while, from Table 3, $p_{min} = 1.829$ and 0, respectively). For $\eta > 1$, the I-modes exist in the (p, η)-plane but have no physical significance as the transformation described at the end of § 3.7 does not produce any integer mode numbers or any aspect ratios lower than $\varepsilon = 1$. For this reason, we concentrate below on the I-modes in models with $0 \leq \eta \leq 1$.

Fig. 3.4 shows the results from linear stability analysis of the I-modes in the (p, ß)–plane. Various marginal stability curves are plotted for different η-values in the interval $0 \leq \eta \leq 1$. The critical case of $\eta = 0.9228$ is denoted by a dashed line. For $\eta = 0.9228$, the I-modes disappear at higher p values ($p = p_{crit}$) compared to the values of p_{min} listed in Table 3. For $\eta < 0.9228$, the marginal stability curves end abruptly at $p = P_{min}$ where the physically acceptable models also terminate. Hence, the lowest p value for the appearance of the I-modes occurs for $\eta = 0.9228$ and is $p_{crit} = p_{min} = 1.947049$ (Table 3 and Fig. 3.3). The transformation of the regions of I-mode instability to different parameter spaces is discussed below.

Some of the results of our investigation of I-modes are summarized in Table 5 for typical models with $\eta = 0$, 0.5, and 0.9228. For each pair of (p, η) values and for models with $p > p_{min}$ (Table 3), only one of the solutions is tabulated because the other solution leads to unphysical aspect ratios ($\varepsilon > 1$) and/or noninteger mode numbers ($m < 1$). One such solution with ε, $m < 1$ is presented for $\eta = 1$ at the bottom of Table 5, where its counterpart with ε, $M_D/M_C \approx 0$ is also noted. The regions of unstable I-modes are illustrated also in Figs. 3.5-7.

TABLE 4
UNSTABLE P-MODES

η	p	$1 - \eta_*$	ß	ε	m	M_D/M_C	t
1.00003	0.9903	8.0×10^{-7}	0.400-0.407	0.02739	none	1.16×10^{-3}	0.499581
	0.99	6.7×10^{-7}	0.395-0.412	0.02733	15	1.15×10^{-3}	0.499583
	0.98	0	0.356-0.445	0.02557	14-17	9.86×10^{-4}	0.499637
1.00002	0.9903	8.2×10^{-6}	0.400-0.406	0.02620	none	1.06×10^{-3}	0.499617
	0.99	8.1×10^{-6}	0.395-0.412	0.02614	none	1.05×10^{-3}	0.499618
	0.98	4.0×10^{-6}	0.356-0.445	0.02432	15-18	8.92×10^{-4}	0.499672
	0.97	4.6×10^{-7}	0.335-0.460	0.02263	15-20	7.57×10^{-4}	0.499718
1.00001	0.9903	1.5×10^{-5}	0.400-0.406	0.02486	none	9.52×10^{-4}	0.499655
	0.99	1.5×10^{-5}	0.395-0.412	0.02480	16	9.47×10^{-4}	0.499657
	0.98	1.1×10^{-5}	0.356-0.445	0.02287	16-19	7.89×10^{-4}	0.499710
	0.97	7.8×10^{-6}	0.335-0.459	0.02109	16-21	6.58×10^{-4}	0.499755
	0.96	4.9×10^{-6}	0.318-0.470	0.01946	17-24	5.48×10^{-4}	0.499793
	0.95	2.5 x 10-6	0.304-0.479	0.01795	17-26	4.57×10^{-4}	0.499825
	0.94	5.2×10^{-7}	0.291-0.486	0.01658	18-29	3.82×10^{-4}	0.499851

TABLE 4 Continued

η	p	1 - η.	ß	ε	m	M_D/M_C	t
0.999999....	0.9903	2.3×10^{-5}	0.401-0.406	0.02309	none	8.21×10^{-4}	0.499702
	0.99	2.3×10^{-5}	0.395-0.411	0.02303	none	8.16×10^{-4}	0.499704
	0.98	1.9×10^{-5}	0.356-0.445	0.02092	18-21	6.60×10^{-4}	0.499757
	0.97	1.5×10^{-5}	0.335-0.459	0.01895	18-24	5.30×10^{-4}	0.499802
	0.96	1.2×10^{-5}	0.318-0.470	0.01709	19-27	4.23×10^{-4}	0.499840
0.999990 ...	0.9903	2.9×10^{-5}	0.401-0.405	0.02127	19	6.97×10^{-4}	0.499747
	0.99	2.8×10^{-5}	0.395-0.411	0.02119	19	6.92×10^{-4}	0.499749
	0.98	2.4×10^{-5}	0.356-0.445	0.01877	19-23	5.32×10^{-4}	0.499804
	0.97	2.1×10^{-5}	0.335-0.459	0.01636	21-28	3.96×10^{-4}	0.499852
	0.96	1.8×10^{-5}	0.318-0.470	0.01382	24-33	2.77×10^{-4}	0.499895
0.999976 ...	0.990303	3.2×10^{-5}	0.403	0.014121	none	3.07×10^{-4}	0.499889

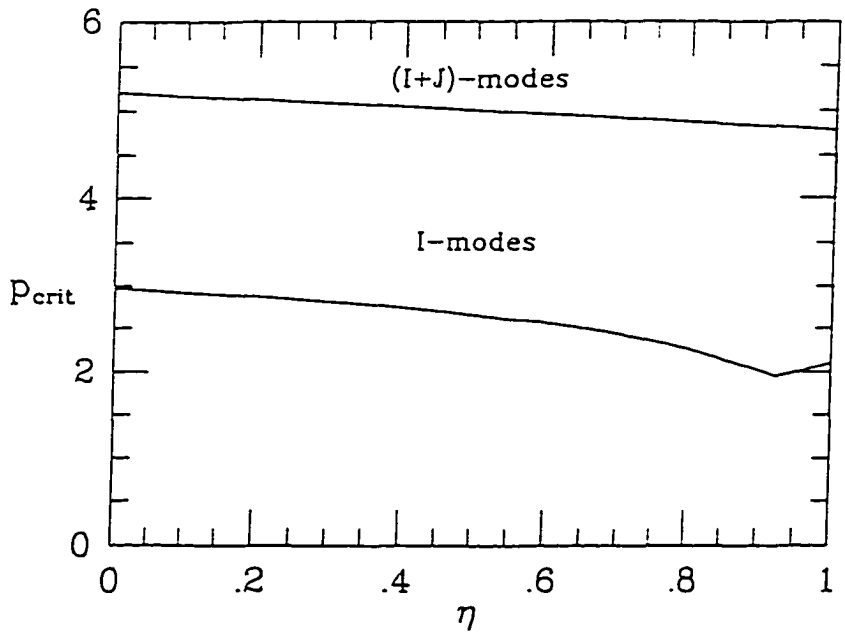

Fig. 3.3 — The critical values Pcrit for the appearance of the I-modes and the J-modes are plotted as functions of η in the interval $0 \leq \eta \leq 1$. Note the characteristic change in the behavior of the I-mode curve at $\eta = 0.9228$.

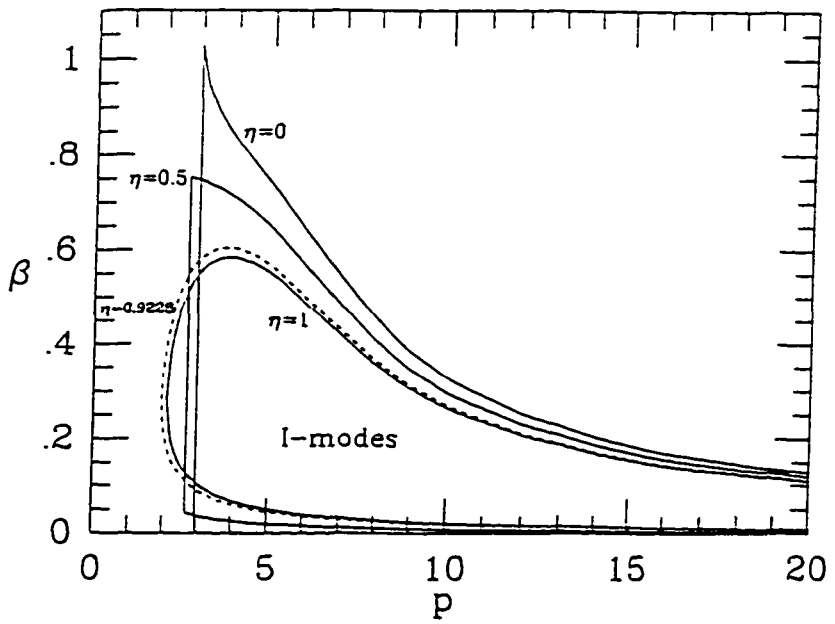

Fig. 3.4. — Regions of unstable I-modes in the (p, ß)-plane for η = 0, 0.5, 0.9228, and 1. For clarity, the η = 0.9228 marginal curve is shown as a dashed line.

TABLE 5
UNSTABLE I-MODES

η	p	η_*	ß	ε	m	M_D/M_C	t
0.....	2.970426	0	0.000-1.029	0.826122	l	∞	0.175858
	3	0	0.000-1.012	0.7420	l	∞	0.1917
	4	0	0.000-0.832	0.3931	l-2	∞	0.2620
	6	0	0.000-0.641	0.2208	l-2	∞	0.3018
	8	0	0.000-0.452	0.1529	l-2	∞	0.3202
	10	0	0.000-0.327	0.1162	l-2	∞	0.3318
	20	0	0.000-0.127	0.0513	l-2	∞	0.3583
0.5....	2.665741	0.4766	0.043-0.753	0.653470	l	9.533171	0.232040
	3	0.4905	0.037-0.747	0.4114	l	4.7858	0.3092
	4	0.4963	0.026-0.710	0.2500	l-2	3.1406	0.3581
	6	0.4987	0.016-0.567	0.1442	l-3	2.3512	0.3881
	8	0.4994	0.011-0.404	0.1009	l-4	2.0461	0.4006
	10	0.4996	0.008-0.296	0.0772	l-3	1.8714	0.4079
	20	0.4999	0.004-0.118	0.0346	l-3	1.5010	0.4238
0.9228..	1.947049	0.9122	0.280	0.370057	none	0.883698	0.389981
	3	0.9215	0.090-0.582	0.1174	l-4	0.2113	0.4734
	4	0.9222	0.060-0.604	0.0789	l-7	0.1697	0.4800
	6	0.9225	0.035-0.500	0.0478	l-10	0.1402	0.4843
	8	0.9227	0.025-0.362	0.0341	l-10	0.1270	0.4860
	10	0.9227	0.019-0.269	0.0264	l-10	0.1189	0.4870
	20	0.9228	0.008-0.110	0.0122	l-9	0.1005	0.4891
l[a].....	2.100	0.9657	0.283	0.6316	none	2.7637	0.2707
	3	0.9104	0.104-0.551	0.9359	none	12.3830	0.1517

[a]The solutions with high ε-values are listed; the omitted solutions have $\varepsilon \sim 10^{-6}$, $M_D/M_C \sim 10^{-11}$, $t \approx 0.5$, and m-values $\sim 10^5$.

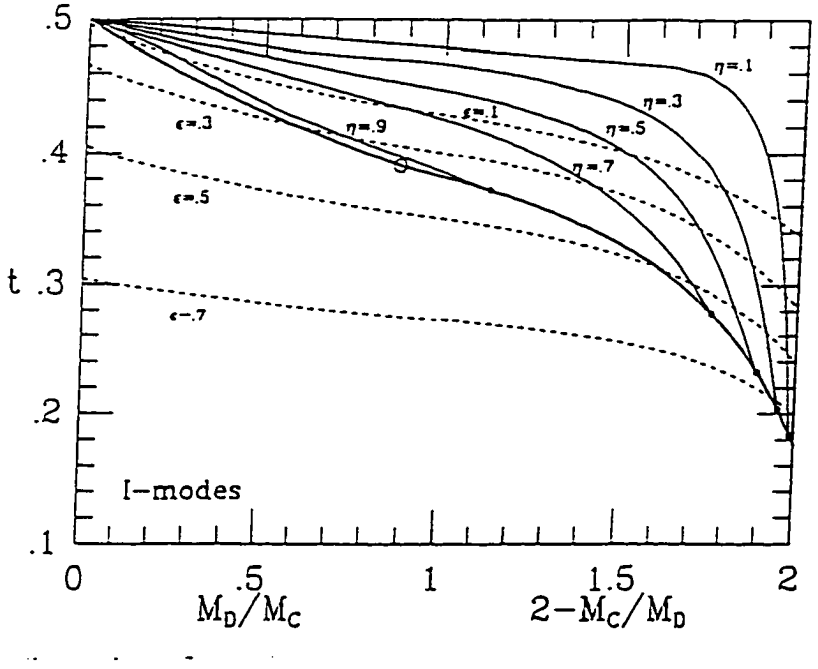

Fig. 3.5 — The region of unstable I-modes is shown in the (M_D/Mc,T/|W|)-plane. The quantity 2–M_C/M_D is plotted instead of the mass ratio for models with M_D/M_C > 1. Thus, the vertical line with 2–M_C/M_D = 2 represents models without a central point-mass (η = 0). Dashed lines represent contours of constant ε–values. The heavy solid line denotes the boundary below which the I-modes disappear. Light solid lines represent contours of constant η-values that terminate on the boundary line at the points indicated by solid dots. The kink marked by an open circle on the boundary line at M_D/M_C = 0.8837, T/|W| = 0.3900 is real and corresponds to the change of behavior of the solutions at η = 0.9228.

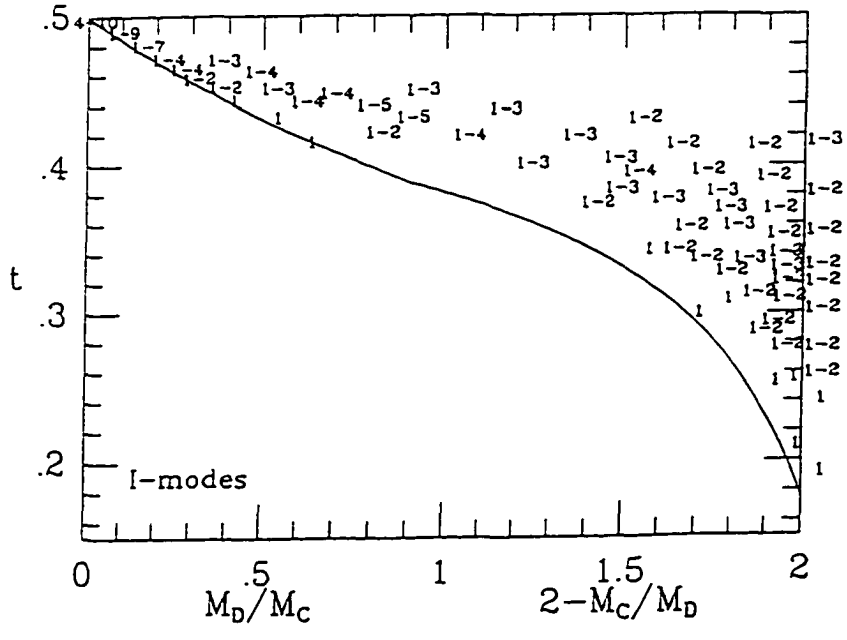

Fig. 3.6 — The integer mode numbers m of the unstable I-modes are illustrated for some characteristic models in the (M_D/M_C, $T/|W|$)-plane. The solid line denotes the boundary below which the I-modes disappear. Models with $\eta = 0$ lie on the $2-M_C/M_D = 2$ vertical line and their mode numbers are shown just outside the frame of the plot.

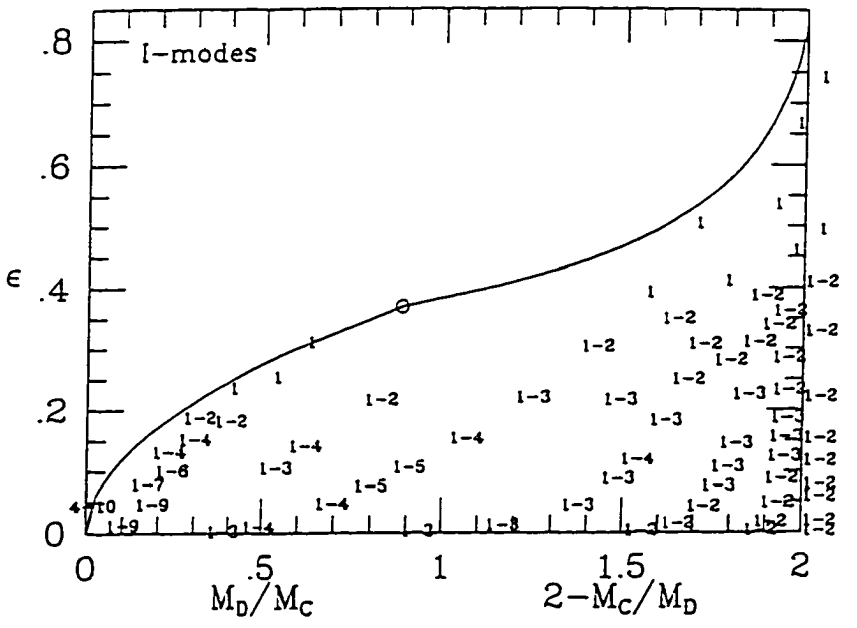

Fig. 3.7 — The region of unstable I-modes is shown in the (M_D/M_C, ε)-plane. The solid line denotes the boundary above which the I-modes disappear. The kink marked by an open circle on the boundary line at $M_D/M_C = 0.8837$, $\varepsilon = 0.3700$ is real and corresponds to the change of behavior of the solutions at $\eta = 0.9228$. The integer mode numbers m of the unstable I-modes are illustrated for some characteristic models. Models with $\eta = 0$ lie on the $2 - M_C/M_D = 2$ vertical line and their mode numbers are shown just outside the frame of the plot.

Figs. 3.5 and 3.6 show the region of unstable I-modes in the (M_D/M_C, $T/|W|$) plane. Contours of constant η and contours of constant ε are superimposed in Fig. 3.5 and the unstable mode numbers are illustrated for some characteristic models in Fig. 3.6. Fig. 3.7 shows the marginal stability curve in the (M_D/M_C, ε)-plane and illustrates again the unstable mode numbers for various equilibrium models. Notice that for $M_D/M_C > 0.5$, the $m = 2$ I-modes are not predicted to be unstable near the boundary curve but they are found to be unstable in models with even higher $T/|W|$-values and even lower ε-values compared to those along the boundary. This behavior is due to the narrow-torus approximation that becomes progressively more accurate with decreasing aspect ratio. Furthermore, our transformation results become more inaccurate with increasing ε– and M_D/M_C–values (§ 3.5) and should not be taken at face value in the region of instability that extends to models with very high ε–values. In general, it is safe to conclude that the marginal stability curve obtained for the I-modes is a good description of the demarkation line between stable and unstable models with ≤ 0.4, $T/|W| \geq 0.3$, and a wide variety of mass ratios ($M_D/M_C \leq 2$).

3.12 The J-modes

Linear analysis shows that the J-modes exist for all values of $\eta < 1$ but only in models with large values of p. Such models have large t-values and their tori are necessarily slender with small ε–values. Thus, the J-modes disappear at substantially higher critical values of $p \equiv p_{crit}$ compared to the I-modes. For

example, p_{crit} = 5.205, 5.165, 5.126, 5.085, 5.042, 5.000, 4.959, 4.915, 4.872, 4.827, and 4.780 for η–values between 0 and 1 in steps of 0.1 (see also Fig. 3.3 above). For $\eta > 1$, the J-modes exist in the (p, η)-plane but have no physical significance as the transformation described at the end of § 3.1 does not produce any integer mode numbers or any aspect ratios lower than $\varepsilon = 1$. For this reason, we concentrate below on the J-modes in models with $0 \leq \eta \leq 1$.

Fig. 3.8 shows the results from linear stability analysis of the J-modes in the (p, ß)-plane. Various marginal stability curves are plotted for different η – values in the interval $0 \leq \eta \leq 1$. The lowest p-value for the appearance of the J-modes occurs for $\eta = 1$ and is p_{crit} = 4.780 (Fig. 3.3). The transformation of the regions of J-mode instability to different parameter spaces is discussed below.

The results of our investigation of J-modes are summarized in Table 6 for typical models with η = 0, 0.5, and 0.9. This last value was chosen as representative of the high η region of the parameter space because there exist no physically interesting solutions for the J-modes in models with $\eta = 1$, where $\varepsilon \leq 10^{-6}$, $M_D/M_C \leq 5 \times 10^{-11}$, $t \approx 0.5$, and $m \sim 106$. For each pair of (p, η)-values, only one of the two possible solutions is tabulated because the other solution leads to unphysical aspect ratios ($\varepsilon > 1$) and/or noninteger mode numbers ($m < 1$). The regions of unstable J-modes are illustrated also in Figs. 3.9-11.

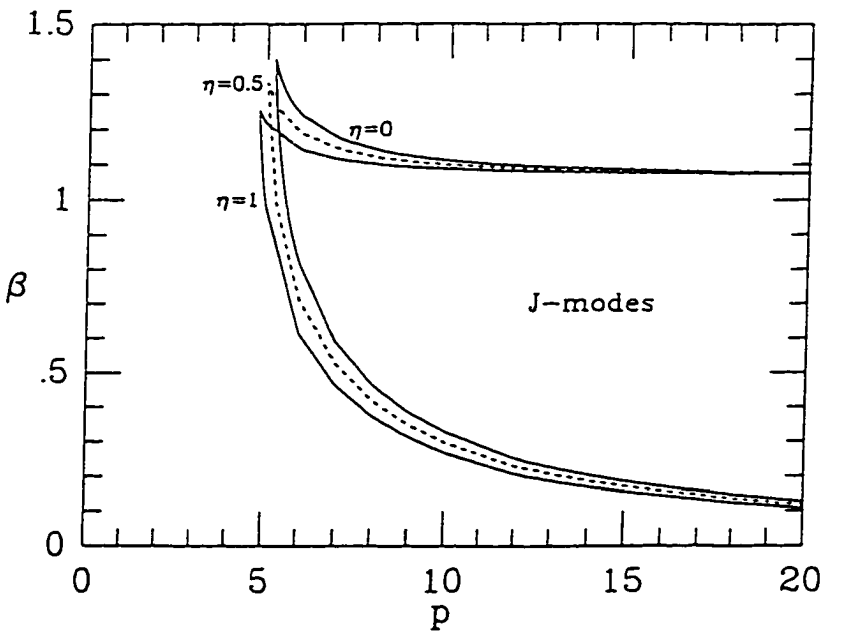

Fig. 3.8 – Regions of unstable J-modes in the (p, ß)-plane for η = 0, 0.5, and 1. For clarity, the η = 0.5 marginal curve is shown as a dashed line.

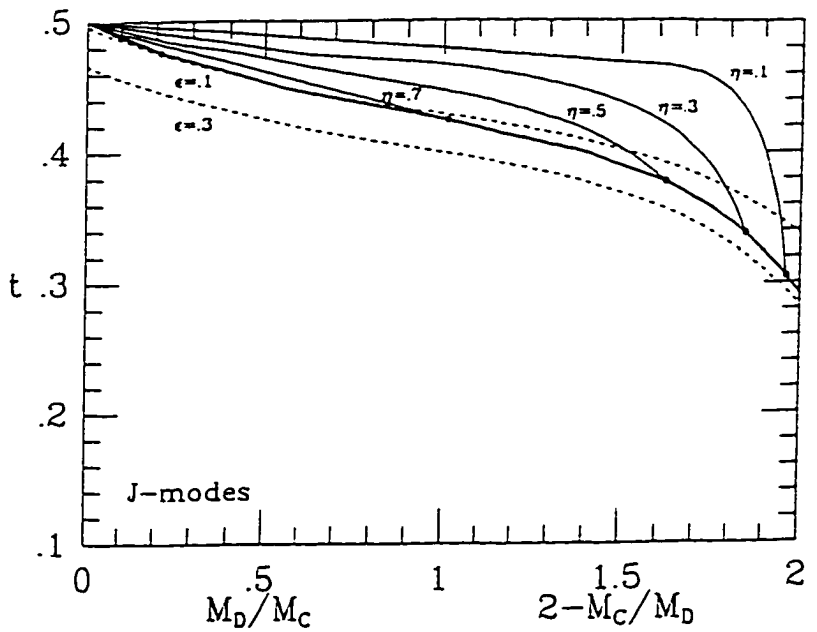

Fig. 3.9 — The region of unstable J-modes is shown in the (M_D/M_C, $T/|W|$)–plane. Dashed lines represent contours of constant ε–values. The heavy solid line denotes the boundary below which the J-modes disappear. Light solid lines represent contours of constant η–values that terminate on the boundary line at the points indicated by solid dots. The $\eta = 0.9$ contour almost coincides with the boundary curve and is not labelled but it terminates at the indicated solid dot near $M_D/M_C = 0.2$, $T/|W| = 0.48$.

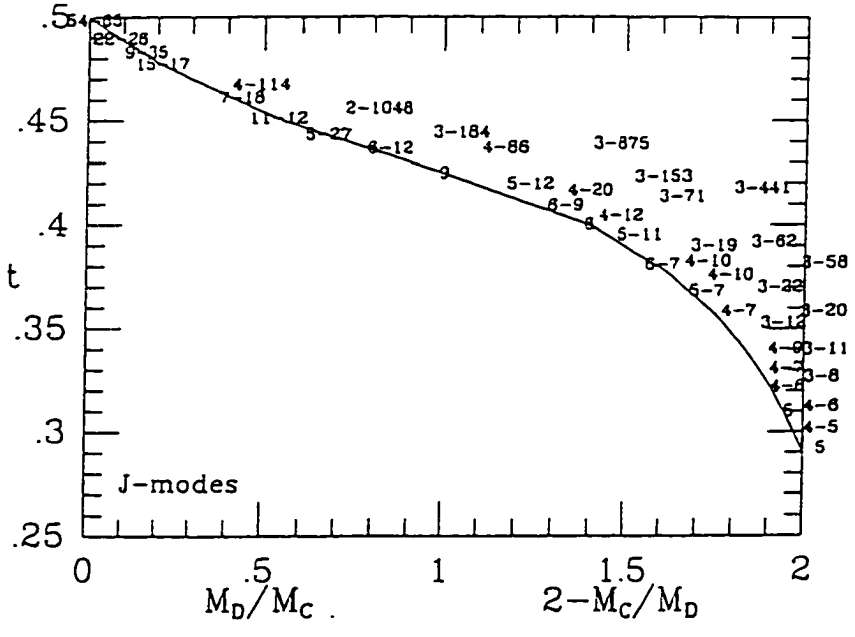

Fig. 3.10 – The integer mode numbers m of the unstable J-modes are illustrated for some characteristic models in the (M_D/M_C, $T/|W|$)-plane. The solid line denotes the boundary below which the J-modes disappear. Models with $\eta = 0$ lie on the $2 - M_C/M_D = 2$ vertical line and their mode numbers are shown just outside the frame of the plot.

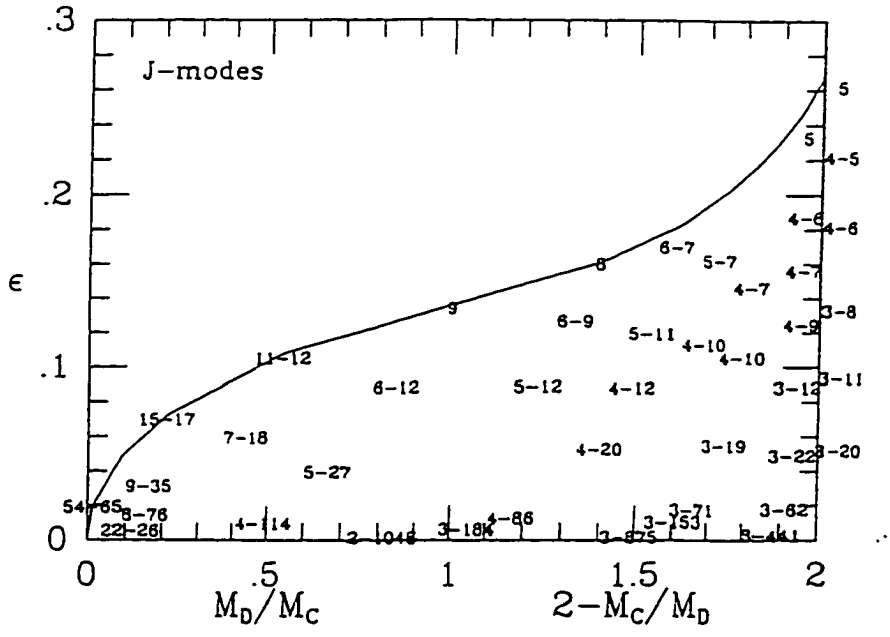

Fig. 3.11 – The region of unstable J-modes is shown in the (M_D/M_C, ε)–plane. The solid line denotes the boundary above which the J-modes disappear. The integer mode numbers m of the unstable J-modes are illustrated for some characteristic models. Models with $\eta = 0$ lie on the $2 - M_C/M_D = 2$ vertical line and their mode numbers are shown just outside the frame of the plot.

TABLE 6
UNSTABLE J-MODES

η	p	η_*	ß	ε	m	M_D/M_C	t
0....	5.205	0	1.400	0.2673	none	∞	0.2903
	6	0	0.811-1.240	0.2208	4-5	∞	0.3018
	8	0	0.462-1.142	0.1529	4-7	∞	0.3203
	10	0	0.327-1.111	0.1162	3-9	∞	0.3318
	20	0	0.127-1.077	0.0513	3-20	∞	0.3583
	50	0	0.041-1.069	0.0182	3-58	∞	0.3816
0.5...	5.000	0.4980	1.333	0.1828	none	2.6260	0.3772
	6	0.4987	0.708-1.189	0.1442	5-8	2.3512	0.3881
	8	0.4994	0.416-1.121	0.1009	5-11	2.0461	0.4006
	10	0.4996	0.296-1.099	0.0772	4-14	1.8714	0.4079
	20	0.4999	0.118-1.074	0.0346	4-31	1.5010	0.4238
	50	0.5000	0.038-1.068	0.0124	4-86	1.2037	0.4372
0.9...	4.827	0.8994	1.270	0.0724	none	0.2135	0.4764
	6	0.8997	0.631-1.151	0.0555	12-20	0.1939	0.4790
	8	0.8998	0.379-1.105	0.0396	10-27	0.1749	0.4814
	10	0.9000	0.272-1.089	0.0306	9-35	0.1634	0.4827
	20	0.9000	0.110-1.072	0.0140	8-76	0.1373	0.4856
	50	0.9000	0.036-1.068	0.0051	8-208	0.1144	0.4880

Figs. 3.9 and 3.10 show the region of unstable J-modes in the (M_D/M_C,T/|W|) plane. Contours of constant η and contours of constant ε are superimposed in Fig. 3.9 and the unstable mode numbers are illustrated for some characteristic models in Fig. 3.10. Fig. 3.11 shows the marginal stability curve in the (M_D/M_C, ε)–plane and illustrates again the unstable mode numbers for various equilibrium models. The results on the J-modes are accurate because these modes appear only in radially slender tori. Notice that, irrespective of the mass ratio, it is very difficult to excite m = 2 J-modes. These unstable modes first appear in extremely slender tori with $\varepsilon \sim 10^{-3}$ and $T/|W| \approx 0.46$. Figs. 3.4 and 3.8 show that the J-modes always extend to higher ß-values than the I-modes. Because, in addition, the J-modes appear only in the most slender of the unstable models, higher J-mode numbers than I-mode numbers are consistently excited in the models depicted in Figs. 3.7 and 3.11. This behavior of unstable mode numbers distinguishes the J-modes from the I-modes.

The behavior of the unstable mode numbers along the marginal stability curve is again different for the J-modes than for the I-modes. As is seen more clearly in Fig. 3.11, the first mode number that is excited just inside the boundary line increases steadily with decreasing mass ratio. In addition, many J-modes are simultaneously unstable in relatively slender tori with low mass ratios, but only a few J-modes are simultaneously unstable in massive, radially extended tori. This behavior also characterizes the J-modes and was first noticed by CN.

3.13 I-modes vs. J-modes

The J-modes appear in a region of the parameter space where I-modes also exist. One would then like to know which type of instability dominates in the region of large T/|W|-values and small ε–values where the I-modes and the J-modes are both unstable. The answer depends on the relative growth rates of the modes. We have examined the growth rates of many models in order to determine the region of the parameter space dominated by $m \geq 2$ J-modes that grow faster than all the unstable I-modes with $m \geq 2$. Our results are plotted in Fig. 3.12, where a detailed comparison between the I-modes and the J-modes is also presented in various parameter spaces. It is evident that the J-modes dominate over the I-modes soon after they appear in all the plotted parameter spaces.

Despite this behavior, the importance of the J-modes is practically limited to high mass ratios compared to the general importance of the I-modes over all mass ratios simply because the J-modes appear and dominate in models with exclusively small disk aspect ratios. Considering then high mass ratios, the J-modes are able to dominate in some models with reasonable aspect ratios (e.g., $\varepsilon \leq 0.1651$ for $M_D/M_C \rightarrow \infty$; see Fig. 3.12c). This conclusion is further quantified in Table 7 where we track the separatrix along which the I-modes and the J-modes have equal growth rates (i.e., $\mathrm{Im}[\nu_I] = \mathrm{Im}[\nu_J]$). The relevant mode numbers β_I, m_I and β_J, m_J of the fastest growing modes and the real parts of the I-mode eigenfrequencies $\mathrm{Re}[\nu_I]$ in the

rotating reference frame are also listed along this critical curve. (Since $\mathrm{Re}[\nu_J] = 0$ for all the J-modes, these eigenfrequencies are not listed in Table 7.)

As Table 7 indicates, the fastest growing J-mode jumps from $m_J = 5$ to 6 and from $m_J = 6$ to 7 at $\eta \approx 0.4$ and 0.6, respectively. These changes are also reflected in the kinks of the critical curve in Fig. 3.12a. Also notice that m_J increases along the separatrix faster than m_I which remains for the most part around 2 and 3. Furthermore, the tabulated growth rates indicate that both instabilities become weaker with decreasing mass ratio and aspect ratio (or, equivalently, with increasing η). Finally, the pattern speeds Ω_p of the unstable I-modes in the inertial frame are obtained from the listed values of $\mathrm{Re}[\nu_I]$ and the equation $\Omega_p/\Omega_0 = 1 - \mathrm{Re}[\nu_I]/m_I$. Since $\mathrm{Re}[\nu_I] \approx 1$ along the separatrix, the pattern speeds can be approximated by the relation $\Omega_p/\Omega_0 \approx 1 - 1/m_I$. This property is characteristic of all the I-modes (Bryan 1889; Hunter 1963; CN; C93).

3.14 Comparison With Previously Obtained Results

The results presented in § 3.10 and in Table 4 suggest that the P-modes appear only in slender models with $\eta \approx 1$. The same conclusion was also hinted by the study of compressible self-gravitating annuli in C93: the P-modes were detected in a model with $p = 1$ and $\eta_* = 0.996$ at the pressure maximum, but they were already absent and replaced by edge modes in a model with $p = 3$ and $\eta_* = 0.955$. On the other hand, Kojima (1986) and WTH studied the appearance of P-modes in zero-

Fig. 3.12 – (a)-(c) The region where the J-modes dominate over the I-modes because they exhibit larger growth rates is shown in the (η, p_{crit})-plane, the (M_D/M_C, $T/|W|$) plane, and the (M_D/M_C, ε)-plane. The solid lines denote the separatrix along which the I-modes and the J-modes have equal growth rates. The J-modes become dominant beyond this critical curve as indicated in the plots. The marginal stability curves where the modes first appear are also indicated by dashed lines. (d) The m = 2 I-mode boundary (fitted dashed line) determined numerically by WTH from marginally stable compressible models with M_D/M_C = 0.2, 1, 5, and oo (solid dots) is shown along with the I-mode boundary and the separatrix beyond which the J-modes dominate (solid lines), both determined from ICT models in this work.

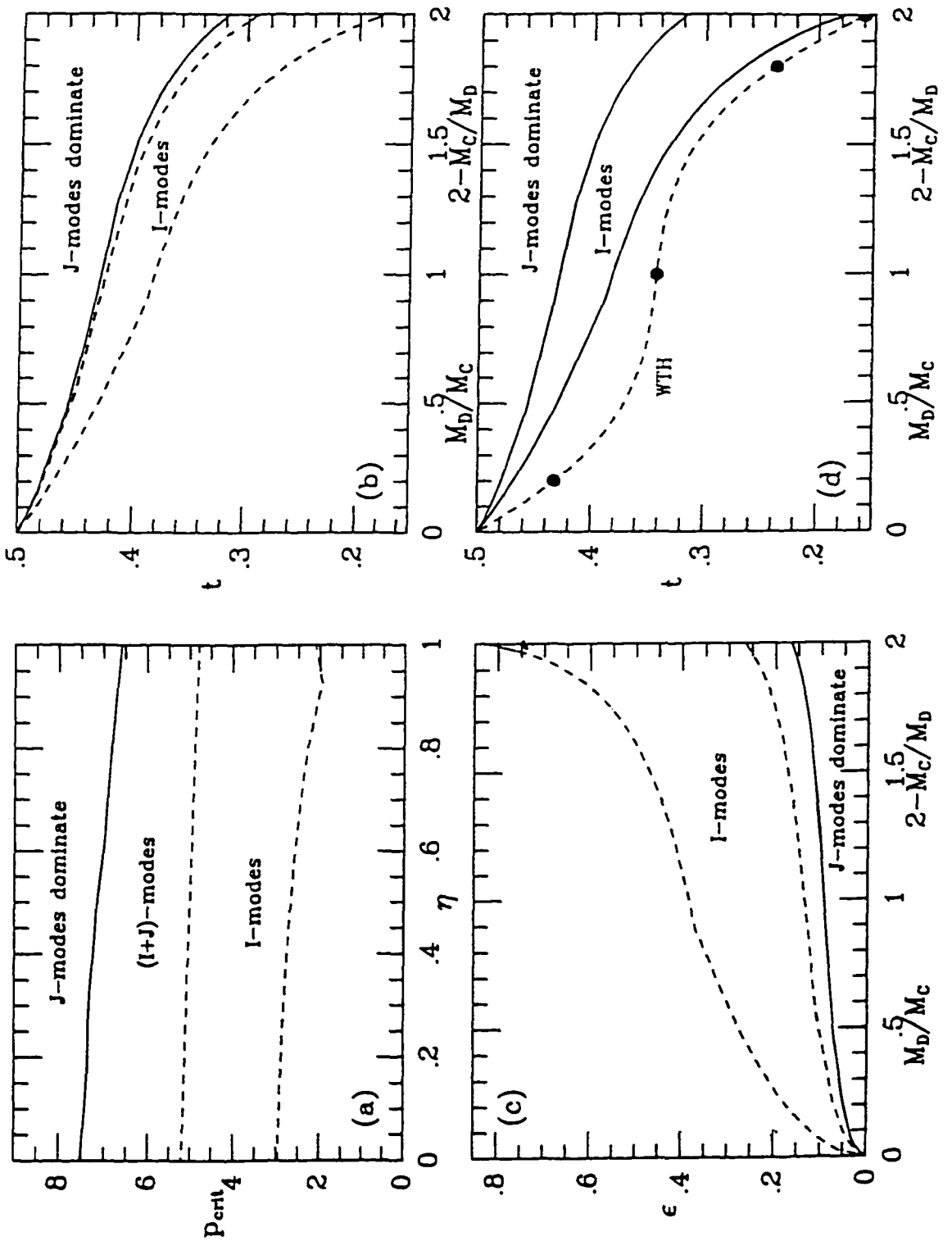

TABLE 7
I-MODES AND J-MODES OF EQUAL STRENGTH
($Im[\nu_I] = Im[\nu_J]$ AND $m_I, m_J \geq 2$)

η	p	ε	β_I	β_J	m_I	m_J	M_D/M_C	t	$Re[\nu_I]$	$Im[\nu_I]$
0.0	7.526	0.1651	0.330	0.825	2	5	∞	0.3167	1.0575	0.9922
0.1	7.428	0.1574	0.315	0.787	2	5	21.466	0.3302	1.0562	0.9833
0.2	7.359	0.1482	0.297	0.741	2	5	9.3463	0.3449	1.0522	0.9725
0.3	7.345	0.1370	0.274	0.685	2	5	5.3061	0.3612	1.0449	0.9607
0.4	7.234	0.1273	0.255	0.764	2	6	3.3292	0.3780	1.0363	0.9380
0.5	7.161	0.1155	0.231	0.693	2	6	2.1503	0.3963	1.0228	0.9099
0.6	7.011	0.1038	0.208	0.727	2	7	1.3862	0.4154	1.0047	0.8689
0.7	6.925	0.0888	0.267	0.711	3	8	0.8493	0.4362	1.0414	0.8407
0.8	6.815	0.0714	0.214	0.714	3	10	0.4644	0.4580	1.0105	0.8079
0.9	6.705	0.0487	0.243	0.730	5	15	0.1858	0.4801	1.0293	0.7782
0.95	6.644	0.0331	0.231	0.761	7	23	0.0799	0.4907	1.0221	0.7598
0.999	6.583	0.0038	0.238	0.747	62	195	0.0010	0.4999	1.0262	0.7419

mass tori and the gradual disappearance of these unstable modes at both low and high aspect ratios. Unfortunately, these studies did not entirely capture the dynamics of the P-modes because the observed behavior of the P-modes in zero-mass tori does not carry to tori with low but nonzero masses (see below). Hence, the previous results concerning the P-modes in massless tori are not representative for realistic disk systems while the present results from tori with $M_D \neq 0$ support the surprising conclusion that these unstable modes are important only in low-mass narrow rings orbiting around massive central objects. As a result, the P-modes of instability do not seem to play the dominant role previously envisioned in the dynamics of real accretion disks, simply because real disks are not expected to be so narrow irrespective of their mass content.

The results concerning the appearance of the I- and J-modes in the (p, ß)-plane and in the (M_D/M_C, $T/|W|$)-plane (§ 3.11 and 3.12) compare well with previously obtained results in incompressible annuli with $q = 2$ (see Appendix B in C93 where the analytic calculations of GN are extended to models with $\eta \neq 1$) and in compressible tori with various angular momentum distributions (see the numerical simulations of TH and WTH), respectively. The regions of I-mode instability shown in Fig. 3.4 are similar to those obtained analytically by C93 for incompressible annuli, when two technical differences are properly accounted for: (a) The mass ratio per unit length in annular models does not have the same physical meaning as the mass ratio M_D/M_C in toroidal models. Thus, no attempt was made

by C93 to terminate the regions of I-mode instability at some minimum, physically relevant p value, as is shown here in Fig. 3.4. (b). The extent of the unstable regions in the (p, ß)-plane is reversed with varying η. This occurs because η is introduced with opposite signs into the stability analysis by the equilibrium enthalpy, which is $H \propto (\eta + p^2/2)$ for ICT models (see eq. [3.36] above) and $H \propto (2 - \eta + p^2)$ for annuli with $q = 2$ (C93). Along the same lines, the regions of J-mode instability shown in Fig. 3.8 are rather similar to those shown in C93 for $\eta \geq 0.56$. The small differences in the details of the shapes must be attributed to the idealized structure of annular models that extend vertically to infinity and are not subject to any Z-gradients.

The results concerning the appearance of the I- and J-modes in the (M_D/M_C, $T/|W|$)-plane (§ 3.13) are in agreement with the numerical results obtained by WTH who have surveyed the available parameter space using compressible equilibria constructed by the HSCF method and having mass ratios of $M_D/M_C = 0.2$, 1, 5, and ∞ and rotation indices of $q = 2$, 1.75, and 1.5. In both sets of results, the I-modes dominate in this parameter space. In fact, the published numerical studies did not detect the J-modes at all because they did not simulate self-gravitating models that were also suffciently slender. The I-modes turn out to be so important in a wide variety of self-gravitating models because the J-modes become dominant only in models with massive and narrow rings (for detailed comparisons, see Fig. 3.12 and Table 7). The only substantial difference between our results shown in Figs. 3.5, 3.6 and the corresponding instability region for $m = 2$ I-modes determined by WTH and

shown here in Fig. 12d is well-understood: Our results do not detect m = 2 I-modes in models with $\varepsilon > 0.4$ and $M_D/M_C > 1$ (see Fig. 3.7), but this is precisely the region of the parameter space where disk models are both massive and radially extended, and the approximations discussed § 3.5 and 3.7 begin to break down.

Because the I-modes appear to dominate the dynamics of both relatively slender and radially extended models over the entire range $0.1 \lesssim M_D/M_C \lesssim 10$ of physically interesting mass ratios, these modes turn out to be the most important modes of instability affecting the dynamical evolution of stellar and protostellar accretion disks whose masses are expected to produce ratios that are comfortably within the quoted range. In particular, evolving protostellar disks whose mass continually increases due to matter infall from the environment are expected to become unstable as soon as they cross into the I-mode region shown in Figs. 5-7 and 12. This point has been discussed in more detail by WTH in the context of eccentric m = 1 modes of instability. On the other hand, AGN disks orbiting around supermassive black holes are described by significantly smaller mass ratios. Therefore, we do not expect AGN disks to be influenced by P-modes because they are not sufficiently narrow, or by I-modes because they are not sufficiently massive, or by J-modes because they are neither sufficiently massive nor sufficiently narrow.

CHAPTER 4

TWO-DIMENSIONAL NONAXISYMMETRIC SYSTEMS

In this chapter we develop a new two-dimensional computational method for constructing compressible, nonaxisymmetric equilibrium configurations with non-trivial internal flows. It is partly based on the HSCF technique. In the past, the HSCF technique has been used to construct equilibrium figures of differentially rotating polytropes. Models constructed in this way often fall into several specific categories according to the symmetry considerations of the models, compressibility, and the type of internal motions allowed. If the models were to be compressible with internal motions, then one could only construct models with azimuthal symmetry, and the internal flow would be dictated by some power-law distribution of specific angular momentum (Hachisu, 1986). If nonaxisymmetric models were of interest, then only the incompressible configurations had internal flow with uniform vorticity (Eriguchi & Hachisu, 1985). Previously, nonaxisymmetric, compressible models have been limited to only uniform rotation and as mentioned earlier, such models are of relatively little interest because they cannot have high values of $T/|W|$.

With our new computational method we can construct two-dimensional, compressible equilibrium structures with internal motion. The models are not required to have any specific type of azimuthal symmetry. Furthermore, the internal flow is not prescribed in advance (e.g., by a power law distribution), but is derived from a stream function which in turn is the solution of a boundary value problem.

The equilibrium structures thus obtained are fully self-gravitating, where the gravitational potential is calculated via the Poisson equation.

We seek solutions to the equations describing the motion of an ideal fluid as derived in chapter 2. We utilize cylindrical polar coordinates and its discrete grid representation for the numerical treatment of the resulting partial differential equations (PDE). With this method we may now construct a large variety of equilibrium sequences of 2D models with nonaxisymmetric cross-sections.

4.1 Equilibrium Models of 2D, Compressible Fluids

Euler's equation, the equation of continuity, the Poisson equation and the equation of state as described in chapter 2 govern the dynamics and evolution of these equilibrium configurations. We proceed to find solutions to this coupled set of PDEs for a particular class of dynamical systems. Specifically, we seek only two-dimensional solutions, where the dynamical parameters depend on the cylindrical polar coordinates R and θ only, and the fluid motion is parallel to the x-y plane; $\Omega = \Omega\hat{k}, \mathbf{V}(R,\theta) = V_R(R,\theta)\hat{R} + V_\theta(R,\theta)\hat{\theta}$, and $V_z = 0$.

The steady-state EOC (2.18) can readily be satisfied by demanding that

$$\rho \mathbf{V} = \nabla \times \mathbf{A} \tag{4.1}$$

for some as yet unspecified vector $\mathbf{A} = (A_R, A_\theta, A_z)$. The task then shifts to identifying an appropriate expression for the vector potential **A**. In component form, eq. (4.1) coupled with the velocity constraints mentioned above leads to the following set of relations:

$$\rho V_R = \frac{1}{R}\frac{\partial A_z}{\partial \theta} - \frac{\partial A_\theta}{\partial z}, \tag{4.2}$$

$$\rho V_\theta = \frac{\partial A_R}{\partial z} - \frac{\partial A_z}{\partial R}, \tag{4.3}$$

$$0 = \frac{1}{R}\left[\frac{\partial}{\partial R}(RA_\theta) - \frac{\partial R_A}{\partial \theta}\right]. \tag{4.4}$$

From eq. (4.4), we have the following constraint on A_R and A_θ:

$$\frac{\partial}{\partial R}(RA_\theta) = \frac{\partial A_R}{\partial \theta}. \tag{4.5}$$

A general solution to this equation can be found only if there exists a scalar function $\Gamma(R,\theta,Z)$ such that

$$A_R = \frac{\partial \Gamma}{\partial R}, \tag{4.6}$$

and

$$A_\theta = \frac{1}{R}\frac{\partial \Gamma}{\partial \theta}. \tag{4.7}$$

Replacing A_R and A_θ with Γ in eqs. (4.2) and (4.3) gives:

$$\rho V_R = \frac{1}{R}\frac{\partial}{\partial \theta}\left[A_Z - \frac{\partial \Gamma}{\partial Z}\right], \tag{4.8}$$

and

$$\rho V_\theta = -\frac{\partial}{\partial R}\left[A_Z - \frac{\partial \Gamma}{\partial Z}\right]. \tag{4.9}$$

Since, $\mathbf{V}(R, \theta)$ does not depend on Z, A_Z and $\frac{\partial}{\partial Z}\Gamma$ must be functions of R and θ only. Therefore, A_Z is independent of Z and Γ is at most linear in Z. Defining a scalar function

$$\Psi(R, \theta) \equiv A_Z - \frac{\partial}{\partial Z}\Gamma, \tag{4.10}$$

the components of the momentum density may be written as:

$$\rho V_R = \frac{1}{R}\frac{\partial}{\partial \theta}\Psi, \tag{4.11}$$

$$\rho V_\theta = -\frac{\partial}{\partial R}\Psi. \tag{4.12}$$

The function $\Psi(R, \theta)$ will serve a similar role as the velocity potential for incompressible fluids. Later, we will develop a geometric representation of Ψ and its relationship to the fluid flow.

The equilibrium configuration is completely determined if the density distribution and the velocity components are known at every point in the region. Since the velocity field can be derived from the scalar potential Ψ, it follows that ρ, and Ψ will completely specify the equilibrium model.

The task is now to determine the scalar potential Ψ for a given density distribution ρ. In the following section we develop the necessary constraint between these two functions in the form of a PDE which will uniquely determine Ψ for a given ρ and angular frequency Ω.

4.2 Solutions of Euler's Equation

Replacing $\mathbf{V}(R, \theta)$ on the left-hand-side of Euler's equation (eq. 2.17) in terms of partial derivatives of Ψ gives rise to the following expression:

$$(\xi + 2\Omega) \times \mathbf{V} = \frac{\xi+2\Omega}{\rho}\nabla\Psi \ . \tag{4.13}$$

Since the right-hand-side of Euler's equation is in the gradient form, the left-hand-side must also be in the form of a gradient of some scalar function. However, except for Ω which is constant, generally the vorticity and density are both functions of R and θ. The expression in eq. (4.13) can be cast in the form of a gradient only if

$$\frac{\xi+2\Omega}{\rho} = f(\Psi) \tag{4.14}$$

where f is an arbitrary function. We will refer to this as the vorticity equation (VE). Then, one may write the left-hand-side in eq. (4.13) in the following form:

$$(\xi + 2\Omega) \times \mathbf{V} = \nabla F(\Psi) \tag{4.15}$$

where $f(\Psi) = dF/d\Psi$; since $\nabla F(\Psi) = dF/d\Psi \ \nabla\Psi = f(\Psi) \ \nabla\Psi$. Euler's equation may now be readily integrated to give the following scalar equation:

$$H+\Phi+F(\Psi)+\frac{1}{2}V^2-\frac{1}{2}\Omega^2 R^2 = C_I \tag{4.16}$$

where C_I is the integration constant. Hereafter, we will refer to this equation as the scalar momentum equation, or SME. For a given equilibrium system, the integration constant C_I and the constant angular frequency Ω are determined via the physical boundary condition as is discussed in the following section.

4.3 Stream Function and Its Associated PDE

From the VE we may solve for the vorticity in terms of ρ and f. Specifically, from the definition $\xi \equiv \nabla \times \mathbf{V}$, and the fact that $V_Z = 0$ and that V_R and V_θ do not depend on Z we have $\xi_R = \xi_\theta = 0$,

$$\xi = [\rho f(\Psi) - 2\Omega]\hat{k} , \tag{4.17}$$

and

$$\xi_z = \frac{1}{R}\left[\frac{\partial}{\partial R}(R V_\theta) - \frac{\partial}{\partial \theta} V_R\right]. \tag{4.18}$$

Replacing V_R and V_θ by their expressions in terms of partial derivatives of Ψ through eqs. (4.11) and (4.12), we arrive at the following PDE in terms of the unknown function Ψ:

$$\frac{\partial}{\partial R}\left[\frac{R}{\rho}\frac{\partial \Psi}{\partial R}\right] + \frac{\partial}{\partial \theta}\left[\frac{1}{R\rho}\frac{\partial \Psi}{\partial \theta}\right] = R[2\Omega - \rho f(\Psi)]. \tag{4.19}$$

The most general form that the function f(Ψ) can take is a power series in Ψ, that is,

$$f(\Psi) = \sum_{-\infty}^{+\infty} C_n \Psi^n \tag{4.20}$$

where the C_n's are the arbitrary coefficients and are chosen as free parameters. However, to keep the PDE (4.19) linear, we will only keep the linear terms and discard the higher ordered terms. Hence we will set $C_n = 0$ for, $n < 0$ or $n > 1$, and adopt the following form for the unknown function f(Ψ):

$$f(\Psi) = C_0 + C_1 \Psi . \tag{4.21}$$

With this form for $f(\Psi)$, we notice that C_0 is essentially the vortensity of the fluid, where vortensity is defined by the ratio ξ/ρ. C_1 has a less obvious and indirect physical interpretation. With this choice of the functional form of $f(\Psi)$, one may write the following expression for $F(\Psi)$:

$$F(\Psi) = C_0 \Psi + \frac{1}{2} C_1 \Psi^2, \tag{4.22}$$

where the integration constant has been set to zero. The SME (4.16) and PDE (4.19) now take the following forms:

$$H + \Phi + C_0\Psi + \frac{1}{2}C_1\Psi^2 + \frac{1}{2}V^2 - \frac{1}{2}\Omega^2 R^2 = C_1, \tag{4.23}$$

$$\frac{\partial}{\partial R}\left(\frac{R}{\rho}\frac{\partial \Psi}{\partial R}\right) + \frac{\partial}{\partial \theta}\left(\frac{1}{R\rho}\frac{\partial \Psi}{\partial \theta}\right) + C_1 R\rho\Psi = R\left(2\Omega - C_0\rho\right). \tag{4.24}$$

Equation (4.24) is a self-adjoint, elliptic PDE. For a given choice of the constants C_0, C_1, and Ω, and a given function $\rho(R, \theta)$, it must be solved for the unknown function $\Psi(R, \theta)$. An appropriate boundary condition must also be supplied in order to guarantee uniqueness of the solution. Once Ψ has been found, one may obtain the velocity field via eqs. (4.11) and (4.12). The density ρ, may be obtained from the enthalpy H via eq. (2.20).

The physical boundary of the system is defined where the density ρ and pressure P vanish. Hence, $H(R,\theta) = 0$ on the boundary as well. Following the general approach outlined by Hachisu (1986) of the self-consistent-field technique, we apply this boundary condition at two points *A* and *B* on the $x(\theta = 0)$ and $y(\theta =$

$\pi/2$)-axes, respectively, in order to determine the integration constant C_1 and Ω in the SME (4.23). The constants C_0 and C_1 are arbitrary and serve as free parameters for our models.

4.4 Dirichlet Boundary Condition

To solve the PDE (4.24), we must supply it with an appropriate boundary condition. We will derive this condition from the physical requirement that the fluid flow must everywhere remain tangent to the physical boundary. In other words, velocity vector $\mathbf{V}(R, \theta)$ must be tangent to the boundary defined by the curve $H(R,\theta) = 0$. In general, the unit vector tangent to the boundary is defined by the following equation,

$$\hat{T} = \frac{(dR, Rd\theta)}{\sqrt{dR^2 + R^2 d\theta^2}}. \tag{4.25}$$

Therefore, the velocity will be properly behaved if, at $H = 0$,

$$\mathbf{V} \times \hat{T} = 0 \ . \tag{4.26a}$$

In other words,

$$(V_R, V_\theta) \times (dR, Rd\theta) = 0 \ , \tag{4.26b}$$

$$R\, V_R\, d\theta - V_\theta\, dR = 0 \ . \tag{4.26c}$$

Substituting for the velocity components in terms of partial derivatives of Ψ in equation 4.26c, will result in

$$\frac{\partial \Psi}{\partial R} dR + \frac{\partial \Psi}{\partial \theta} d\theta = 0, \tag{4.27}$$

That is,

$$d\Psi = 0\,. \tag{4.28}$$

This implies that the function Ψ must be constant on the boundary. Since, the velocity components depend on the partial derivatives of Ψ only, we may choose this constant to be zero.

4.5 Stream Function and Streamlines

In order to derive a geometric interpretation of the velocity potential Ψ, we note the following property of the induced flow:

$$\mathbf{V}\cdot\nabla\Psi = \frac{1}{\rho}\left(\frac{1}{R}\frac{\partial}{\partial\theta}\Psi, -\frac{\partial}{\partial R}\Psi\right)\cdot\left(\frac{\partial}{\partial\theta}\Psi, \frac{1}{R}\frac{\partial}{\partial R}\Psi\right) = 0. \tag{4.29}$$

Hence, $\mathbf{V}$ is perpendicular to $\nabla\Psi$ everywhere inside the configuration as well as on the boundary. It must also be true that $\mathbf{V}$ is everywhere tangent to curves of constant Ψ. Therefore, once we have derived the equilibrium function $\Psi(R,\theta)$, contours of Ψ will identify fluid streamlines and Ψ can be thought of as a stream function. In particular, the boundary defined by $H = 0$ is also a streamline as required; both of the functions H and Ψ must share the same boundary contour.

4.6 Numerical Scheme and Discretization

To find the stream function Ψ, we must solve its associated self-adjoint, elliptic PDE (eq. 4.24) for fixed values of the constants Ω and C_0, and various trial density distributions $\rho(R,\theta)$. We adopt a discrete polar grid, $(R_j,\theta_,)$ such that,

$$R_j = jh, \text{ for } 0 \le j \le JBND\ , \tag{4.30a}$$

$$\theta_\ell = \ell k, \text{ for } 0 \le \ell \le LMAX\ , \tag{4.30b}$$

where $h \equiv 1/JMAX$, and $k \equiv 2\pi/LMAX$. We adopt the following standard finite-difference scheme representations of the partial derivatives on the left hand side of eq. (4.24):

$$\frac{\partial}{\partial R}\left[\frac{R}{\rho}\frac{\partial \Psi}{\partial R}\right] = \frac{1}{h^2}\left[a_+(\Psi_{j+1,\ell} - \Psi_{j,\ell}) - a_-(\Psi_{j,\ell} - \Psi_{j-1,\ell})\right] \tag{4.31a}$$

$$\frac{\partial}{\partial \theta}\left[\frac{1}{R\rho}\frac{\partial \Psi}{\partial \theta}\right] = \frac{1}{k^2}\left[b_+(\Psi_{j,\ell+1} - \Psi_{j,\ell}) - b_-(\Psi_{j,\ell} - \Psi_{j,\ell-1})\right] \tag{4.31b}$$

where

$$a_\pm \equiv \frac{R_j \pm \frac{h}{2}}{\rho(R_j \pm \frac{h}{2}, \theta_\ell)} \tag{4.32a}$$

$$b_\pm \equiv \left[R_j\, \rho\left(R_j, \theta_\ell \pm \frac{k}{2}\right)\right]^{-1}\ . \tag{4.32b}$$

An analytical function $f(R,\theta)$ is replaced by its discrete representation $f_{j,\ell} = f(R_j,\theta_\ell)$ centered at the j,ℓ cell on the polar grid. Substituting for the partial derivatives in the PDE in terms of their equivalent finite difference formulas and collecting terms, we will arrive at the following set of linear equations in the unknown function Ψ:

$$c_{j,\ell-1}\,\Psi_{j,\ell-1} + c_{j-1,\ell}\,\Psi_{j-1,\ell} + c_{j,\ell}\,\Psi_{j,\ell} + c_{j+1,\ell}\,\Psi_{j+1,\ell} + c_{j,\ell+1}\,\Psi_{j,\ell+1} = g_{j,\ell}, \tag{4.33}$$

for $1 \le j \le JBND$, and $1 \le \ell \le LMAX$,

where

$$c_{j,\ell-1} = \frac{1}{k^2} b_-,\ c_{j-1,\ell} = \frac{1}{h^2} a_- \tag{4.34a}$$

$$c_{j,\ell} = g - \frac{1}{h^2}(a_+ + a_-) - \frac{1}{k^2}(b_+ + b_-) \tag{4.34b}$$

$$c_{j+1,\ell} = \frac{1}{h^2} a_+,\ c_{j,\ell+1} = \frac{1}{k^2} b_+ \tag{4.34c}$$

and JBND is the j at the boundary which is dependent on the azimuthal index ℓ in nonaxisymmetric models. The coefficient matrix of the corresponding system of linear equations has dimension equal to the number of the grid points inside the region. The resulting sparse system is solved via the standard available packages.

4.7 Iteration Procedure

As in HSCF, we will normalize the density, the equatorial radius at point A on the x-axis, and the gravitational constant as follows: $\rho_{max} = R_A = G = 1$. At the boundary of the fluid, the enthalpy is zero. We will apply this condition at two points A and B on the x and y axes, respectively, to determine the integration constant C_I and the constant angular velocity Ω in the SME:

$$H(A) = 0 = C_I - \Phi(A) - \frac{1}{2} V_A^2 + \frac{1}{2}\Omega^2 \tag{4.35}$$

$$H(B) = 0 = C_I - \Phi(B) - \frac{1}{2} V_B^2 + \frac{1}{2}\Omega^2 R_B^2 \tag{4.36}$$

It should be noted that $\Psi(A) = \Psi(B) = 0$ as a result of the Dirichet boundary condition derived earlier. Therefore the following expressions are obtained for the constants C_I and Ω:

$$\Omega^2 = \frac{2(\Phi_A - \Phi_B) + V_A^2 - V_B^2}{1 - R_B^2} \tag{4.37}$$

$$C_I = \Phi_A + \frac{1}{2}V_A^2 - \frac{1}{2}\Omega^2 \tag{4.38}$$

The iteration is started with a choice of a uniform density distribution and no internal flow: $\rho = 1$, $\Psi = 0$, $VR = V_\theta = 0$ as an initial guess. The gravitational potential Φ for this density distribution is calculated via the Poisson equation. The constants C_I and Ω are then found through equations (4.37) and (4.38). The PDE is then solved for the unknown stream function for a given C_0 and C_I. Once the stream function and the density are known, the velocity field can be calculated via equations (4.11) and (4.12). At this point C_I, Ω, Φ, Ψ, V_R and V_θ are all known. We may use these parameters to obtain a new enthalpy from the SME. A new density is then calculated from this enthalpy via equation (2.20) for the chosen polytropic index *n*. The new density distribution thus obtained will serve as an input for the next iteration. This procedure is repeated until the relative changes between two successive iterations fall within the chosen error bound which is usually of the order of 10^{-4}.

4.8 The Internal Circulation

The equilibrium configurations to be obtained using the method developed in this chapter are the compressible analogs of the classical ellipsoidal sequences studied by Maclaurin, Dedekind, Jacobi, and Riemann. These classical ellipsoids all had uniform vorticity ξ. Since both ξ and Ω were parallel and along one of the

principal axes, a dimensionless parameter $f \equiv \xi/\Omega$ was defined to characterize the internal differential flow relative to the constant frame rotation Ω (see, for example, Chandrasekhar, 1969, p. 133).

A sequence was defined as one along which f remains constant. This definition of f will necessarily be generalized in order to apply to general compressible fluids with arbitrary nonuniform vorticity $\xi(R,\theta)$. We will define a generalized dimensionless parameter C, which characterizes the internal flow relative to the constant frame rotation:

$$C \equiv \frac{\oint_Q \mathbf{V} \cdot d\mathbf{l}}{\Omega A} \tag{4.39}$$

where dl is the tangent element along a closed contour Q enclosing an area A. This is the circulation of the fluid due to the internal flow around an arbitrary closed contour Q normalized to the constant frame rotation. The line integral can be transformed into a surface integral through the standard vector integral identity:

$$C \equiv \frac{\oint_Q \mathbf{V} \cdot d\mathbf{l}}{\Omega A} = \frac{\int_A \nabla \times \mathbf{V} \cdot d\mathbf{A}}{\Omega A} = \frac{\int \xi \, dA}{\Omega A} . \tag{4.40}$$

In the last term, the definition of vorticity (eq. 2.15) has been utilized. In particular, when the vorticity is uniform throughout the region, it reduces to the familiar $f \equiv \xi/\Omega$ which characterized the classical incompressible ellipsoidal sequences. In the special case when $C = -2$, the fluid is irrotational.

CHAPTER 5

STEADY STATE STRUCTURES

In this chapter we construct several sequences of equilibrium structures using the two-dimensional computational technique developed in the previous chapter. We construct infinite cylindrical models with polytropic indices n = 0.0, 0.2, 0.4, 0.5, 0.6 and 0.7, and a variety of two-dimensional disks with polytropic indices n = 0.0, 0.4, 0.7, 0.8, 1.0, and 1.3. We then discuss the significance of these models with internal motions compared to corresponding polytropic models with uniform rotation. In particular, we are able to construct specific configurations that would not exist in the uniformly rotating models but can only exist as differentially rotating structures. Furthermore, with the presence of these internal motions we are able to obtain equilibrium structures with higher T/|W| than would be possible to construct under the constraint of uniform rotation. Since the frame angular frequency cannot increase beyond a certain limit for a given axis ratio (due to mass shedding at the boundary), it becomes evident that the higher gain in T/|W| must come from the internal motions.

Of the two general types of configurations being modeled here, we will discover that the disk models appear to have a broader spectrum in their allowed parameter space than the infinite cylinders. In general, the cylinders are more restricted in their allowed geometry. The cylindrical structures are limited to elliptic and slightly deformed elliptic cross-sections. This may be attributed to their infinite extent and, hence, to their effectively logarithmic gravitational potential profile.

Since our two-dimensional models are to be the compressible counterpart of the classical incompressible ellipsoidal sequences (CIES), it is appropriate to compare these new models with the classical works, whenever possible. We will point out the similarities and the differences between the two, and provide insights when the new models depart from the CIES. As was emphasized in chapter 1 these two-dimensional, compressible models sit between the classical works done in the past, and the fully general, three-dimensional models which one would hope to be able to construct in the future.

To emphasize some of the features shared with the CIES, and to draw analogies between them, we briefly review here a portion of the classical literature. We begin with Figure 5.1, (see also Fig. 7.15 Chandrasekhar 1969) which depicts a parameter space containing all possible incompressible ellipsoidal configurations with uniform rotation or with velocities linear in the coordinates. Here, as before, a, b, and c are the semi-major axes of the ellipsoids along the x, y, and z axes, respectively, with b, $c \leq a$. The various curves drawn in Fig. 5.1 are analytically constructed sequences of models having constant $f \equiv \xi/\Omega$ (see the discussion in connection with § 4.8). The models along the $f = 0$ sequence are the uniformly rotating, Jacobi ellipsoids; all other models are Riemann ellipsoids that possess some kind of linear internal flow but with uniform vorticity.

We will choose the dimensionless circulation C as defined in the previous chapter as a straightforward generalization of f for compressible fluids with arbitrary

internal motions. As was shown in chapter 4, in the special case of uniform vorticity, C will reduce to f.

Since we will exclusively be constructing two-dimensional configurations for which the axis ratio c/a has no definition, we will be unable to locate our model sequences in the (b/a, c/a) parameter space shown in Fig. 5.1. However, since the axis ratio c/a generally decreases in more rapidly rotating 3D configurations, the rotation frequency Ω — which also is measureable in our 2D equilibrium figures— may be used in place of c/a as the second parameter. In Fig. 5.2, the analytical CIES are replotted in the (b/a, Ω^2) plane. For comparison, Fig. 5.3 shows several 2D compressible disk sequences that we have constructed using the numerical technique described in chapter 4. Each of the curves in Fig. 5.3 represents a sequence of constant C. The sequences of constant C in Fig. 5.3 qualitatively resemble the sequences of constant f in Fig. 5.2. An important difference, however, is that for all allowed values of f in Fig. 5.2, the Riemann sequences exist for the entire range of the axis-ratios in the (b/a, Ω^2) plane. This is only true for our compressible disk sequences with $|C| < 0.5$. The sequences at higher |C| tend to terminate at smaller axis-ratios along the b/a axis. That is, they do not "connect" with or bifurcate from any axisymmetric sequence. The higher the value of |C|, the smaller the maximum allowed b/a becomes.

We also will construct several uniformly and differentially rotating cylindrical polytropes for various axis-ratios. For these models we are able to identify the

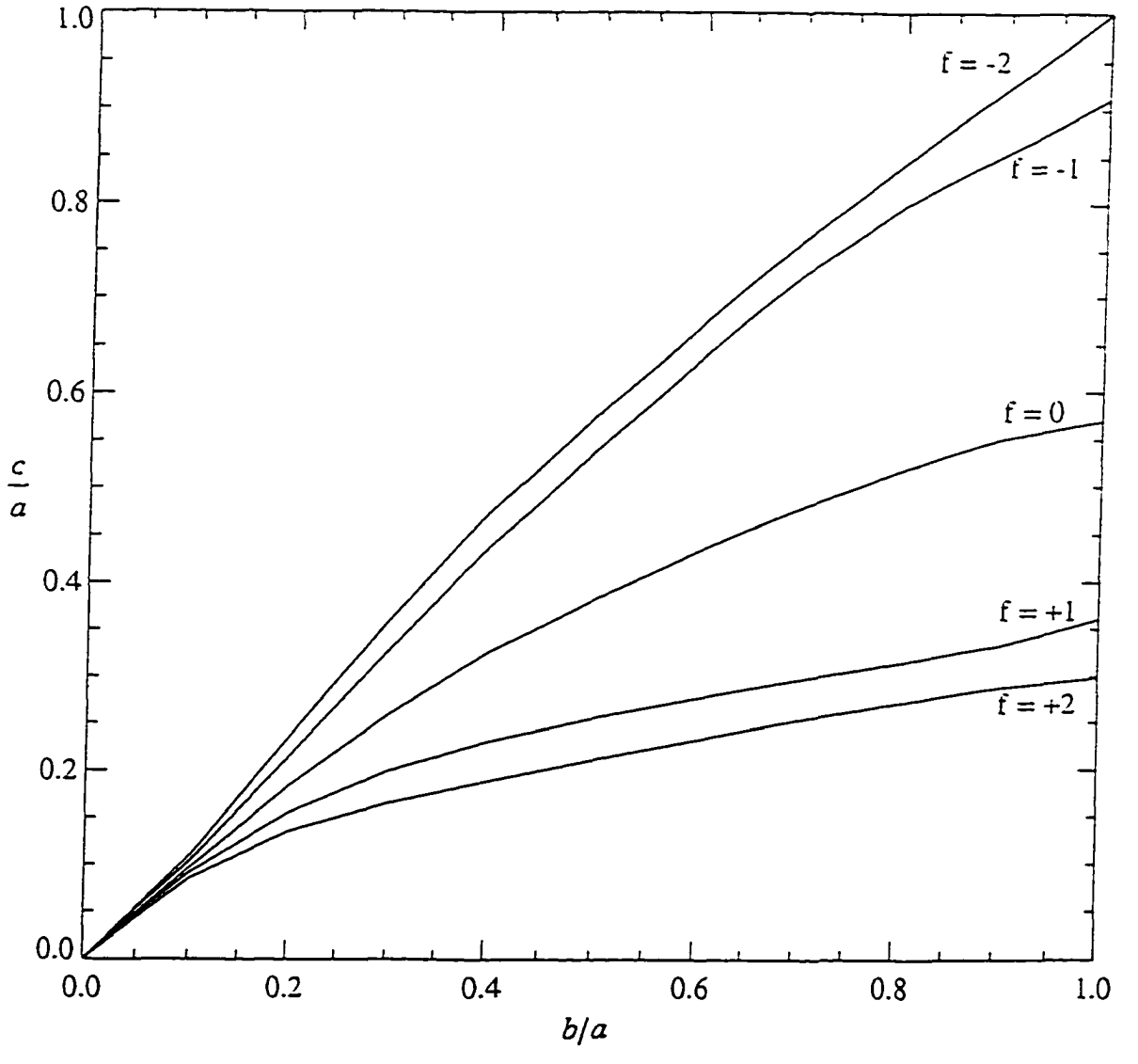

Fig. 5.1 — Several sequences of classical incompressible Riemann ellipsoids derived analytically. In particular, the f = 0 sequence corresponds to solidly rotating Jacobi ellipsoids. The semi-major axes a, b, and c are along the x, y, and z axes respectively with b, c ≤ a. The vertical axis at b/a = 1 represents the Maclaurin spheroids.

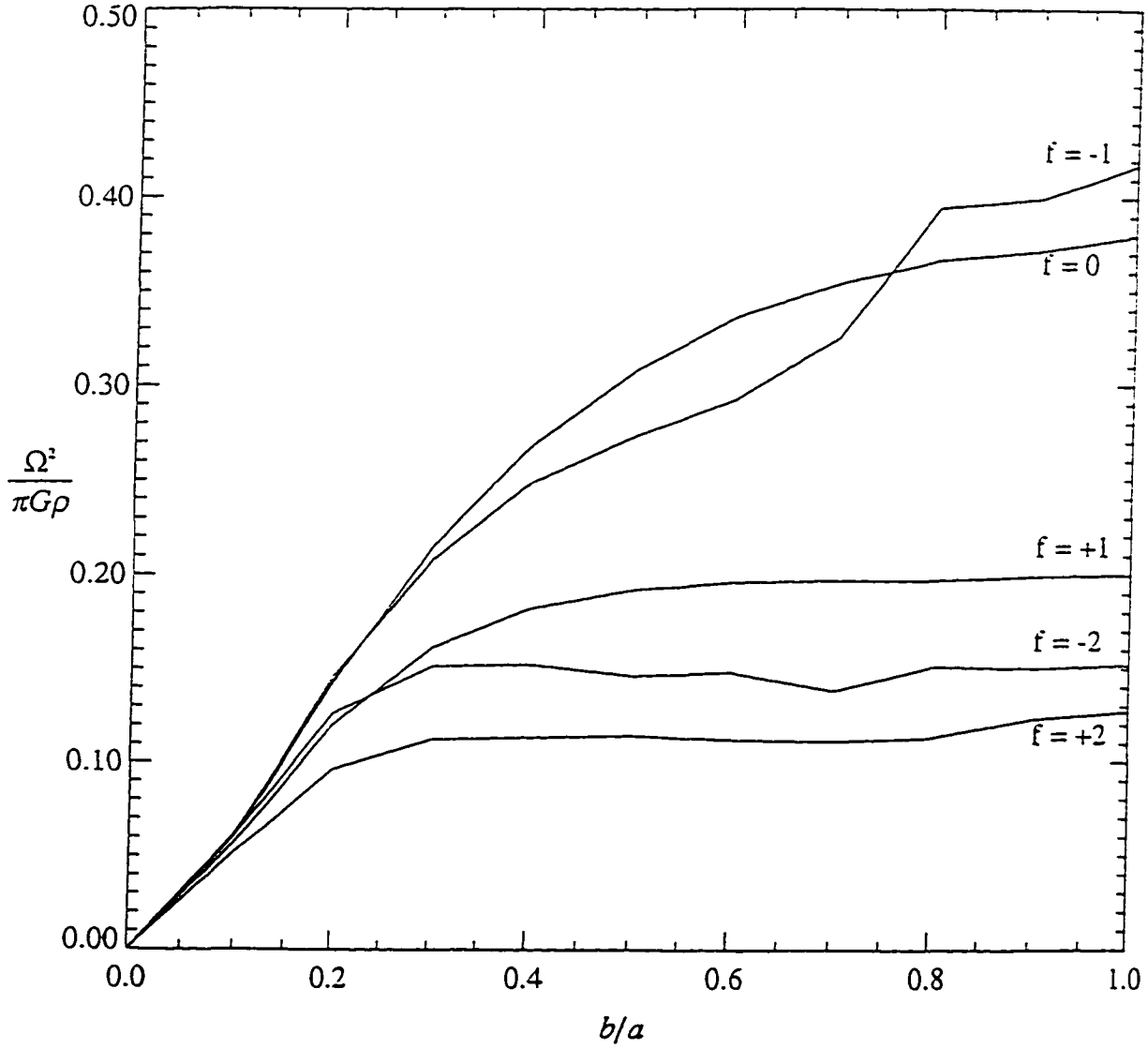

Fig. 5.2 — The same sequences as in fig. 5.1, but the vertical axis c/a has been replaced with $\Omega^2/\pi G\rho$.

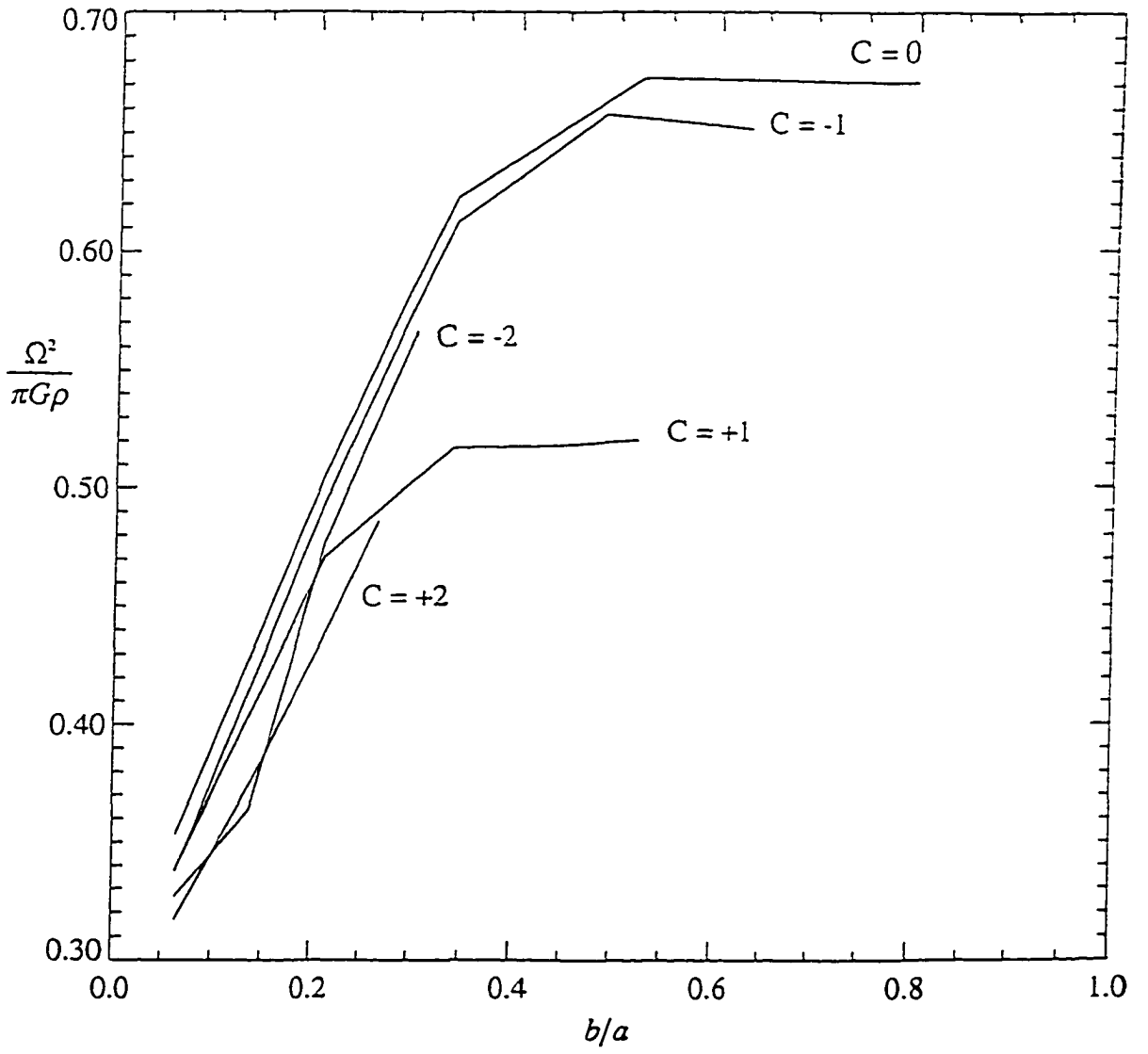

Fig. 5.3 — The two-dimensional compressible disk analog of fig. 5.2. The individual lines are disk sequences with constant circulation C. All sequences have internal motion, including the C = 0 sequence. Here $\rho \equiv M/A$, where M is the mass and A is the area.

point where the nonaxisymmetric sequence bifurcates from the axially symmetric sequence. This will serve as the two-dimensional compressible cylindrical analog of the CIES. For the disk models, we will obtain a similar sequence where dumbbell-shaped configurations seem to bifurcate from the elliptical disks. The sequence won't terminate with dumbbells however, and further down, the binaries will branch off.

Since, as noted above, the cylindrical sequences are restricted to elliptical and slightly deformed elliptical cross-sections, their geometries are more in line with the classical ellipsoidal models in contrast to disk sequences. In presenting the detailed properties of our newly constructed, compressible models, we will start with the infinite cylinders. This will be followed by a discussion of the more complex, two-dimensional disk models.

5.1 Infinite Cylinders

As was reviewed in Chapter 1, the equilibrium structures of uniformly rotating, incompressible cylinders were first investigated by Jeans around the turn of the century. He studied the cross-sections of various cylindrical configurations bounded by a single, continuous curve via analytical techniques. More specifically, he examined the equilibrium and stability criteria of cylinders with circular, elliptical, deformed elliptical, and pear-shaped boundaries along with bifurcation points along various equilibrium sequences.

Here we extend the work of Jeans (1902) by constructing compressible sequences of cylinders with elliptical and deformed elliptical boundaries. We are

concerned primarily with the construction of these two-dimensional equilibrium structures and not with their stability. Additionally, our cylinders will be allowed to have several types of internal motions. We have discovered that cylindrical configurations tend to maintain approximately elliptical boundaries for nearly all axis-ratios b/a, down to very small values. Table 5.1 summarizes the global physical characteristics of our various model cylinders having n = 0.0, 0.2, 0.4, 0.5, 0.6, and 0.7. $C_1 = -0.6$ in the majority of these models. Column 1 of the table gives the assigned model number; columns 2, 3, and 4 list our chosen values of the polytropic index, axis ratio, and vortensity, respectively; and columns 5, 6, and 7 tabulate values of the circulation C, frame rotation Ω, and total angular momentum L that were derived for each converged model.

Figures 5.4 a-e illustrate some of the properties of a cylindrical configuration with n = 0.2, b/a = 0.523, and $C_0 = 3.0$ (model C10 in Table 5.1). Panels (a) and (b) represent the density and stream-line contours, respectively, of the equilibrium fluid configuration. In panel (c), the corresponding retrograde velocity vector-field is plotted. The function v_y (x), that is, the y-component of the internal velocity along the major axis, is shown in panel (d).

In order to put the internal motions into a better perspective quantitatively, we will consider their amplitudes relative to the local sound speed. In polytropic fluids,

TABLE 5.1
VARIOUS CYLINDRICAL CONFIGURATION

(1) #	(2) n	(3) b/a	(4) C_0	(5) C	(6) Ω	(7) L
C01	0.0	0.394	3.3	0.070	1.593	0.379
C02	0.0	0.523	3.3	-0.048	1.691	0.322
C03	0.0	0.817	3.3	-0.136	1.773	0.271
C04	0.0	0.394	3.7	0.319	1.592	0.398
C05	0.0	0.523	3.7	0.185	1.690	0.346
C06	0.0	0.817	3.7	0.085	1.773	0.299
C07	0.2	0.284	3.0	-0.314	1.447	0.469
C08	0.2	0.284	3.5	-0.188	1.441	0.489
C09	0.2	0.284	4.0	0.321	1.415	0.510
C10	0.2	0.523	3.0	-0.525	1.664	0.314
C11	0.2	0.523	3.5	-0.233	1.642	0.342
C12	0.2	0.523	4.0	-0.004	1.667	0.375
C13	0.2	0.523	4.5	0.276	1.655	0.411
C14	0.2	0.761	3.0	-0.593	1.729	0.261
C15	0.2	0.761	3.5	-0.347	1.749	0.293
C16	0.2	0.761	4.5	0.151	1.755	0.364
C17	0.2	0.817	3.3	-0.371	1.680	0.272
C18	0.2	0.817	3.5	-0.273	1.682	0.286
C19	0.2	0.817	3.7	-0.172	1.687	0.300
C20	0.4	0.523	4.0	-0.219	1.604	0.379
C21	0.5	0.523	4.5	-0.349	1.570	0.409
C22	0.6	0.523	4.0	-0.368	1.529	0.360
C23	0.6	0.523	4.4	-0.179	1.539	0.399
C24	0.7	0.523	4.7	-0.090	1.559	0.420

n is the polytropic index, b/a is the axis ratio, C_0 is the vortensity parameter, C is the internal circulation, Ω is the uniform frame angular velocity, and L is the total angular momentum.

c_s^2 = H/n, where H is the enthalpy of the fluid. Since, generally speaking, the enthalpy has its maximum at the center of our cylindrical configurations and tends towards zero at the surface, the sound speed also exhibits a maximum at the center and decreases monotonically toward the surface. The velocities derived from our converged equilibrium stream function generally have the opposite behaviour. They start near zero amplitude around the center and exhibit a maximum close to the surface. Therefore, in regions sufficiently close to the boundary, the internal flow may cross the sound barrier and become supersonic. Figure 5.4 (e) shows the magnitude of the internal flow relative to the sound speed for model C10. The dimensionless ratio v/c is plotted as a function of the radial distance along the major axis.

Figure 5.5 illustrates some of the properties of model C11, a cylinder with the same axis ratio as model C10, but with a higher measure of internal motion (C_0 = 3.5). The vortensity of the fluid generally dictates the type of the internal motions (flow pattern and their topologies) and their relative amplitudes. In model C11, the flow topology is governed by the presence of vortices and stagnation points.

Figure 5.6 illustrates the properties of model C13 which has an even higher value of the vortensity, C_0 = 4.5. The fluid flow is similar to the flow in figure 5.3 except that now it is entirely prograde.

As is evident from these figures, we may identify three types of internal flow topologies corresponding to different ranges of the vortensity C_0. Low and high

values of C_0 correspond to retrograde and prograde flow, respectively, over the entire configuration as shown in Figures 5.4 and 5.6. Intermediate values of C_0 are characterized by vortical flows across several disjoint components: In the central most region of the fluid, motion is prograde around a central vortex. Two retrograde flows enclose two off-centered vortices which are located symmetrically about the origin on the x-axis. Three stagnation points are associated with these three vortices and two others are located symmetrically about the origin, on the y-axis. A portion of the flow (a narrow band located near the surface) encloses all three vortices and the five stagnation points in a retrograde motion. It extends to the boundary of the fluid. The volume of the configuration that is occupied by this retrograde flow near the boundary is sensitive to the vortensity of the fluid. At relatively high values of C_0, it is pushed away towards the boundary and will essentially disappear from the view as has been illustrated in figure 5.6.

The five stagnation points identified above for configurations like model C11 constitute the critical points where the internal fluid velocity vanishes. The location of the off-axis vortex on the positive x-axis can also be identified where $v_y = 0$ in the plot of v_y (x) - Fig. 5.5c.

Figure 5.7 shows another cylindrical model (C07) with the same parameters as model C10 shown in Fig. 5.4, except with a smaller axis-ratio: b/a = 0.284. Hence, for a fixed value of the vortensity, the topology of the flow can be changed by varying the axis ratio of the configuration.

Figure 5.8 shows model C20. In Fig. 5.9 the same cylinder is plotted at a higher polytropic index n = 0.6 (model C22).

Cylindrical models at higher polytropic indices generally exist either at larger axis ratios or with the presence of internal differential motion. Model C24, for example, describes a cylindrical structure with n = 0.7 and a vortensity parameter C_0 = 4.7 and b/a = 0.523. The corresponding uniformly rotating cylinder terminates at n = 0.4. To obtain a model with no internal motion at n = 0.7, one must go to axis ratios $b/a \geq 0.71$. For very round cylinders ($b/a \geq 0.8$), the existence of an equilibrium is more dependent on the axis ratio and less on the internal flow. In general, the presence of internal motion is more critical in cylinders with smaller axis ratio at higher polytropic indices.

Figure 5.10 shows two sequences of incompressible cylinders with uniform rotation where the nonaxisymmetric sequence bifurcates from the axisymmetric sequence. In this figure $\Omega^2/\pi G\rho$ is plotted vs. angular momentum L. In this figure Ω^2 reaches its maximum at 6.3. At L = 0.28 the incompressible sequence bifurcates from the axisymmetric sequence. It terminates at L = 0.6. This sequence was also derived by Jeans and it is the analog of the Maclaurin/Jacobi bifurcation.

Fig. 5.11 shows the same sequence for polytropic index n = 0.2 models. This is the compressible analog of Fig. 5.10. Both sequences terminate at smaller values along the horizontal and vertical axes. In particular the angular momentum terminates at L = 0.38.

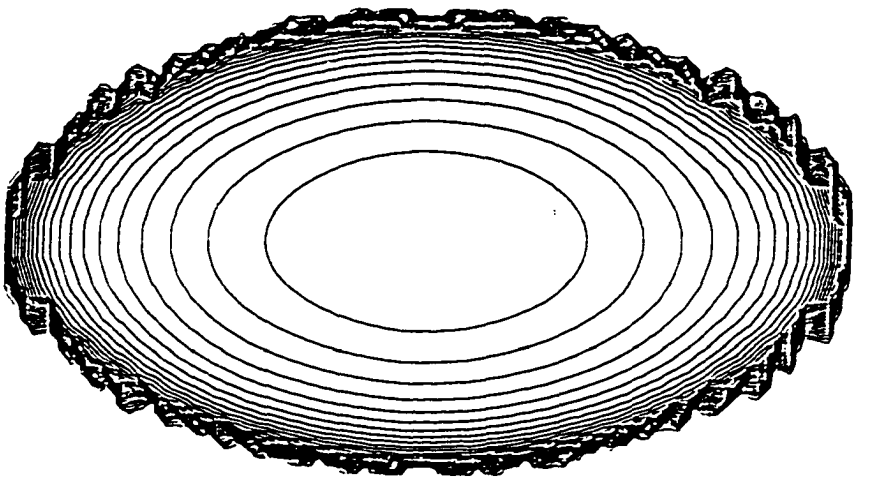

(*a*)

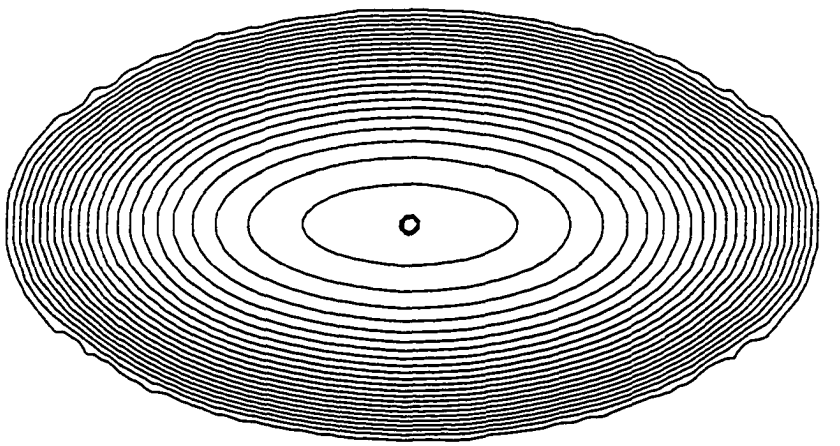

(*b*)

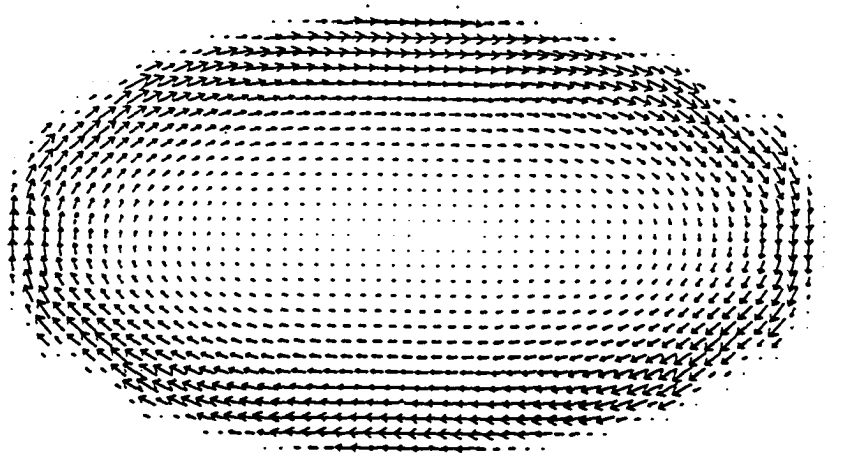

(*c*)

Fig. 5.4 — (Model C10) A low vortensity cylindrical polytrope with (a) isodensity contours, (b) the streamlines, and (c) the corresponding retrograde velocity vector field. In addition to the internal notion, the cylindrical configuration also rotates counter clockwise with a constant angular frequency Ω.

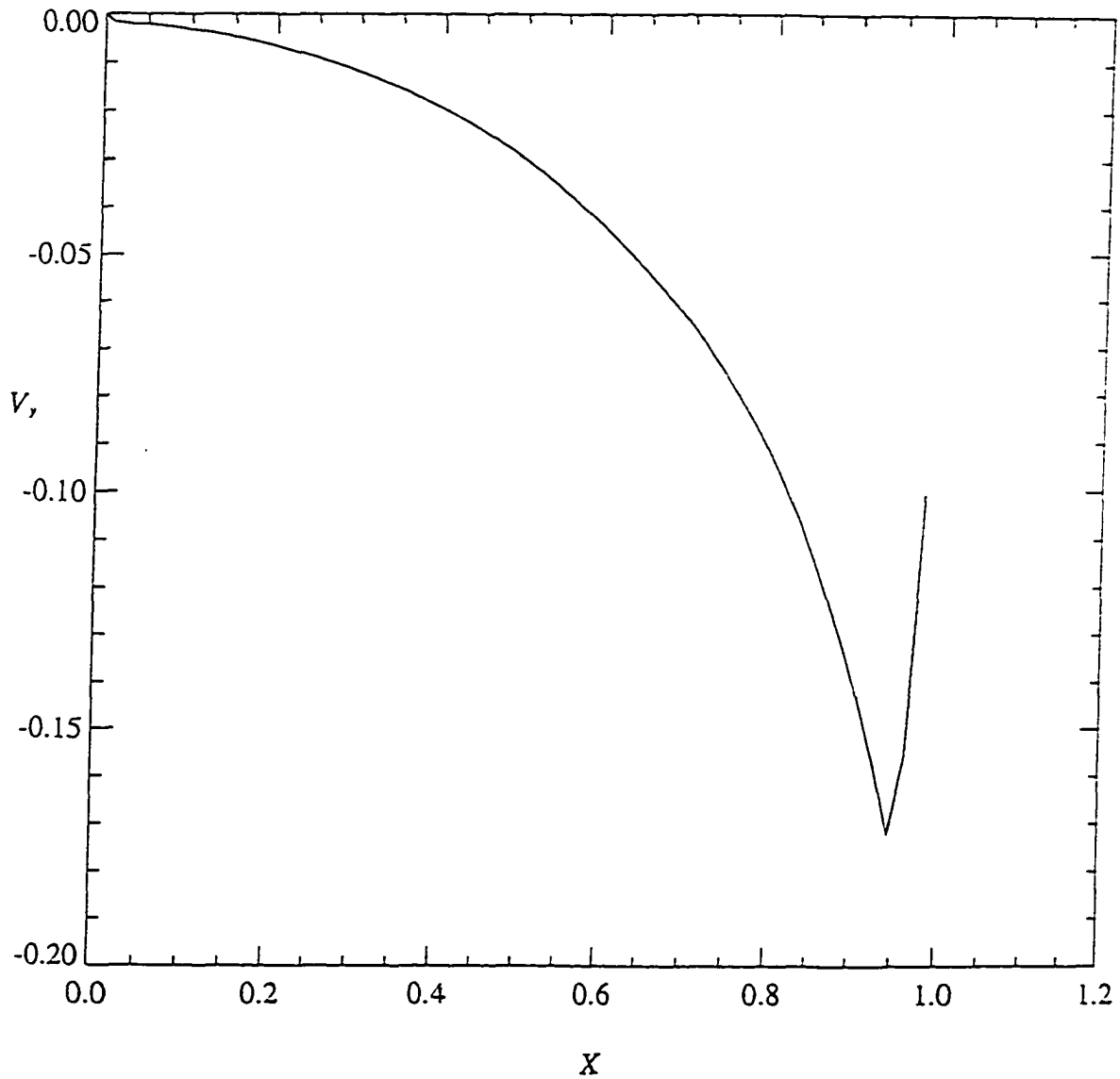

(*d*)

Fig. 5.4 — The y-component of the internal velocity along the x-axis as seen by an observer in the rotating frame of reference with constant angular frequency Ω.

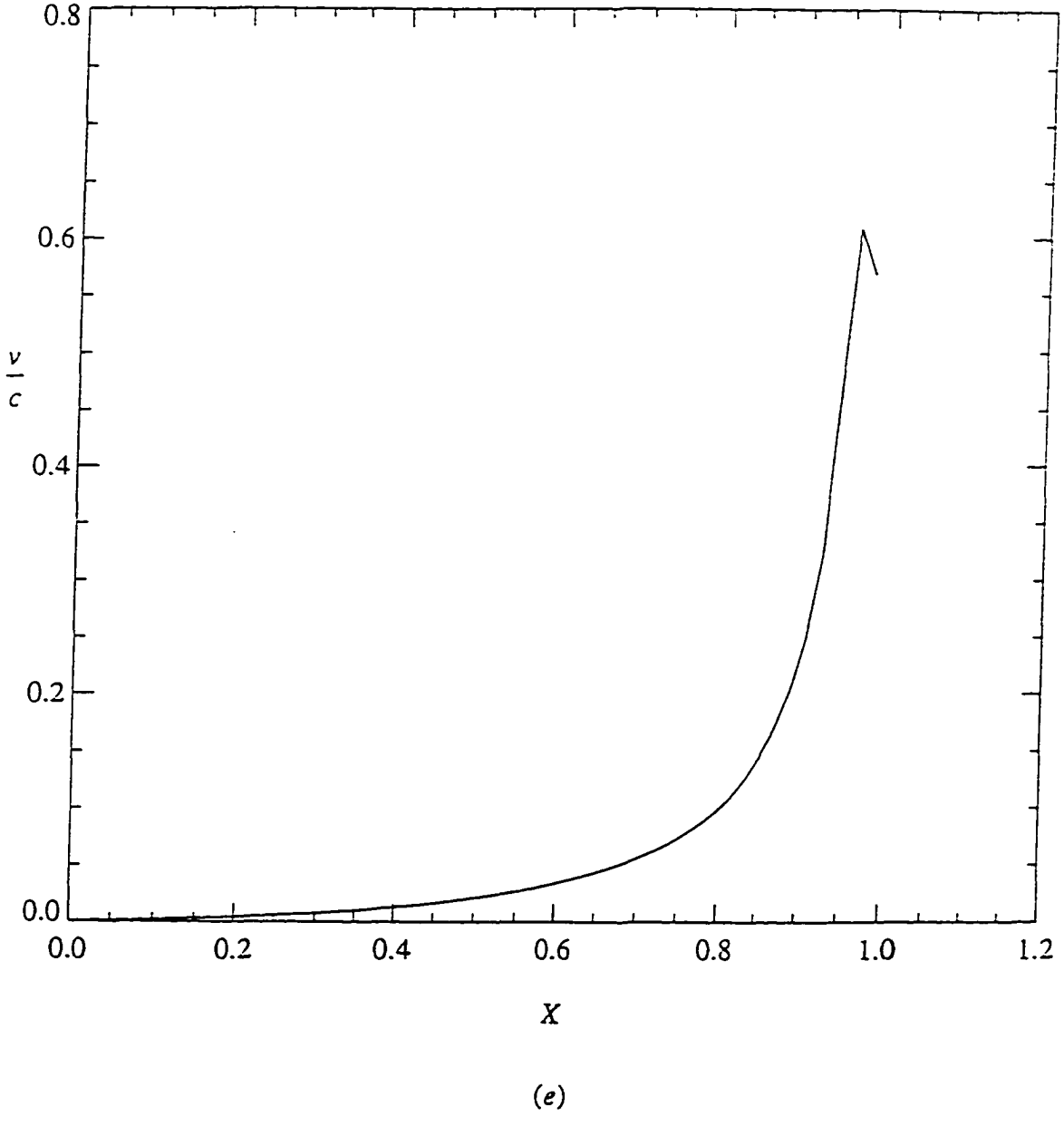

Fig. 5.4 — The dimensionaless v/c, where v is the magnitude of the internal flow and c is the speed of sound, is plotted along the x-axis.

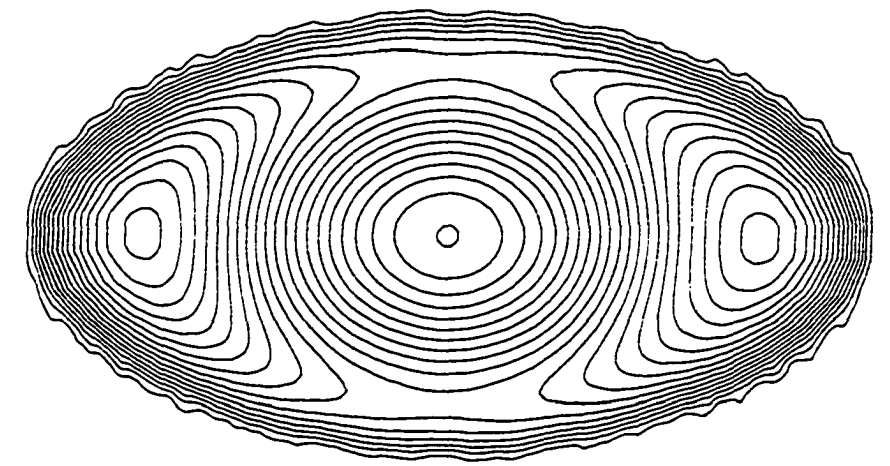

(*a*)

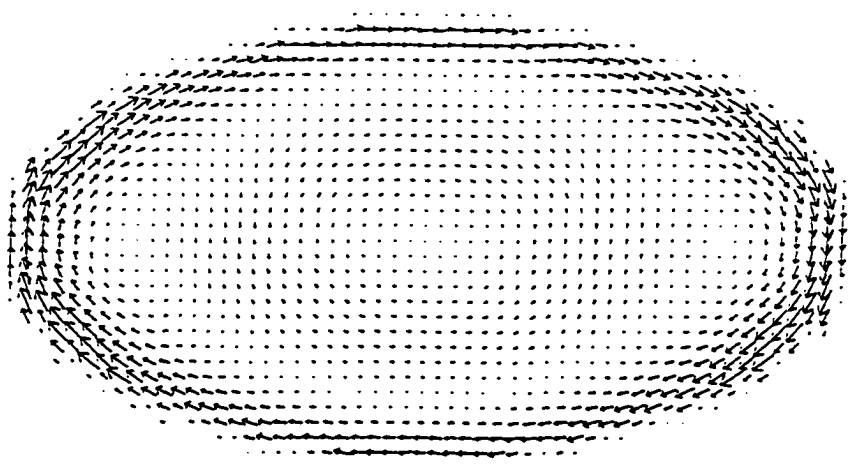

(*b*)

Fig. 5.5 — (Model C11) The same as in fig. 5.4 but with intermediate value of vortensity: (a) the streamlines, and (b) the corresponding vortical velocity field. The internal flow contains several critical points (vortices and stagnation points).

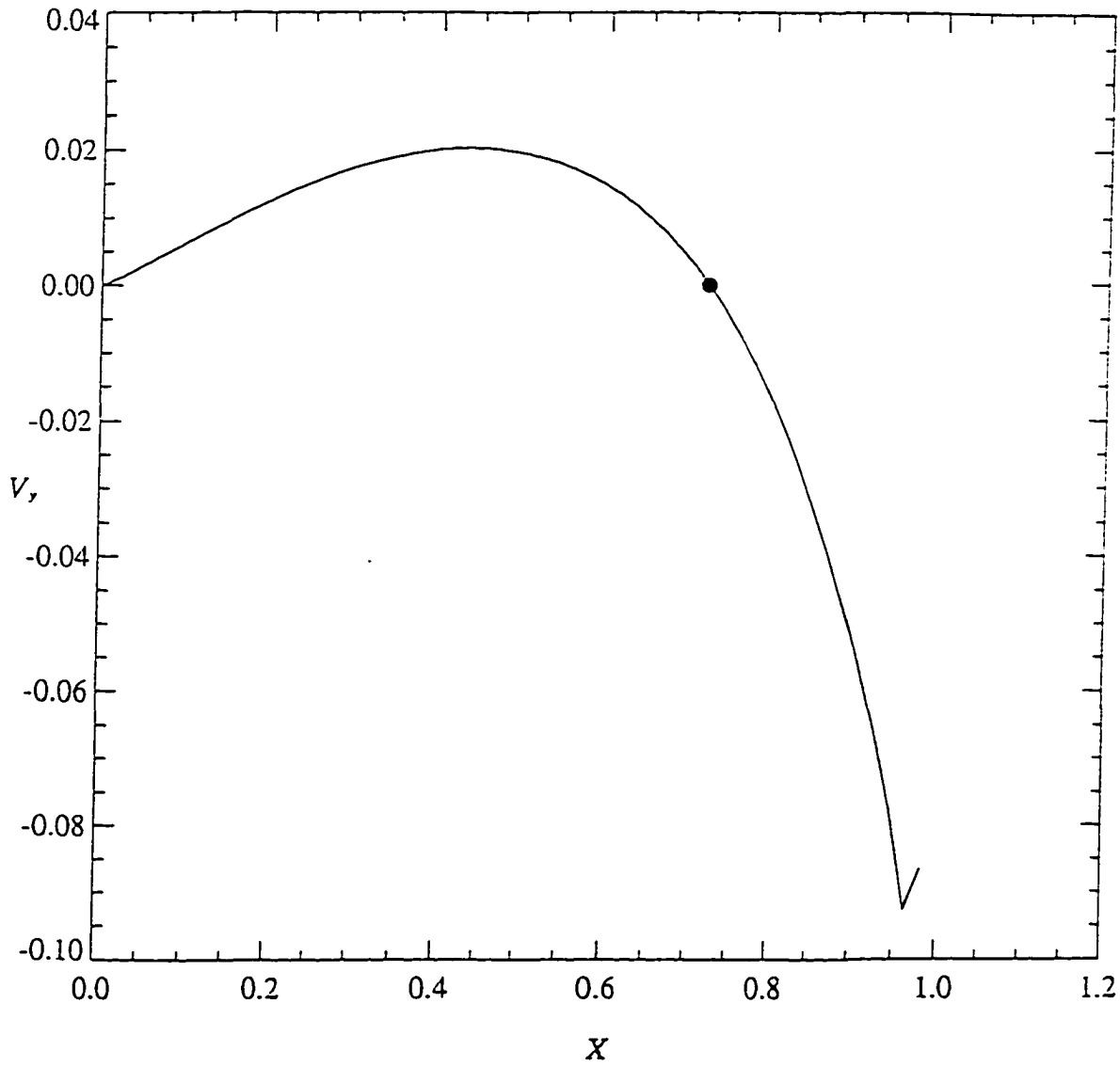

(c)

Fig. 5.5 — The y-component of the internal velocity along the x-axis. The solid circle corresponds to the off-centered vortex on the x-axis, where the internal flow vanishes.

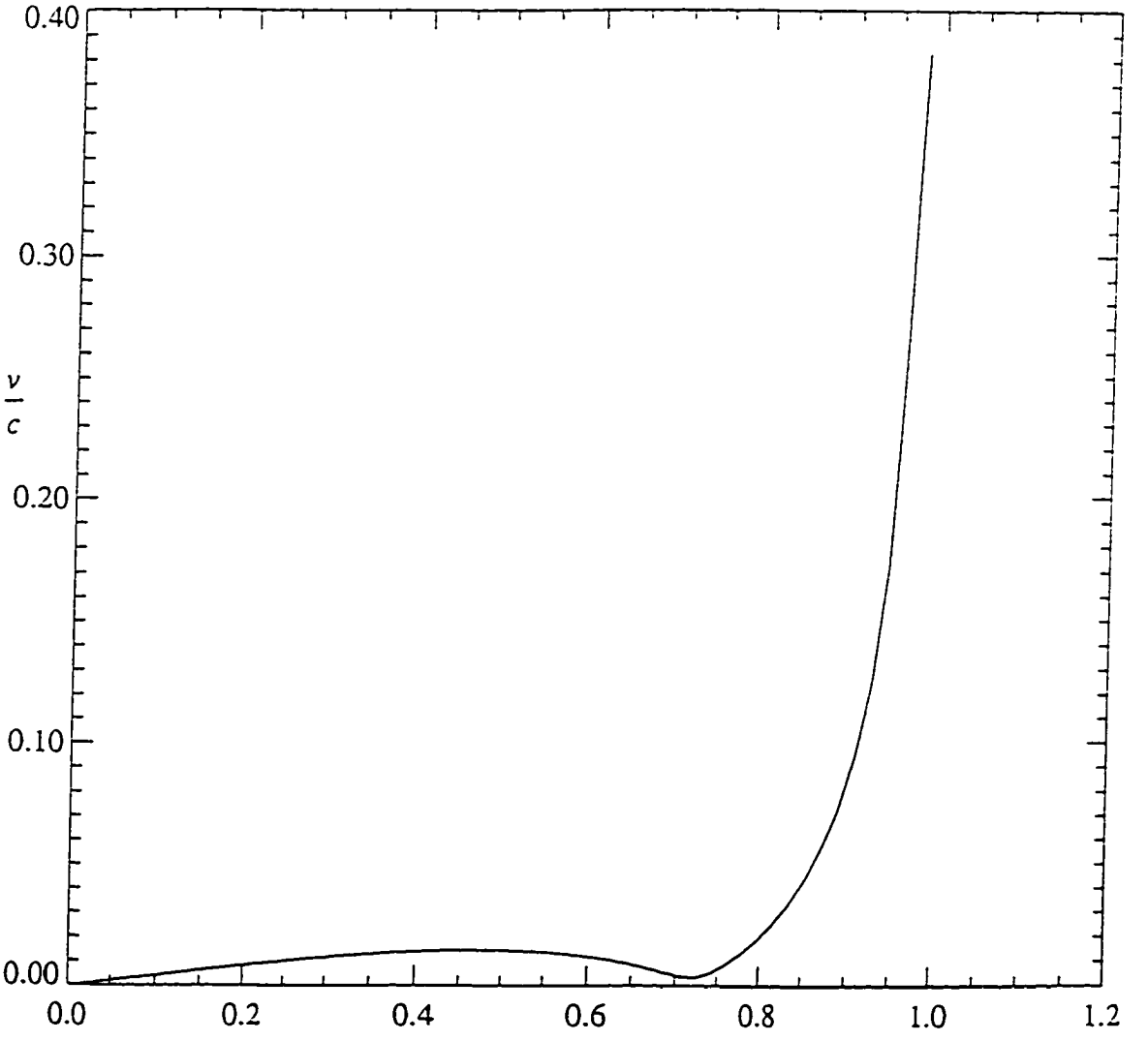

Fig. 5.5 — The dimensionless ratio v/c along the x-axis.

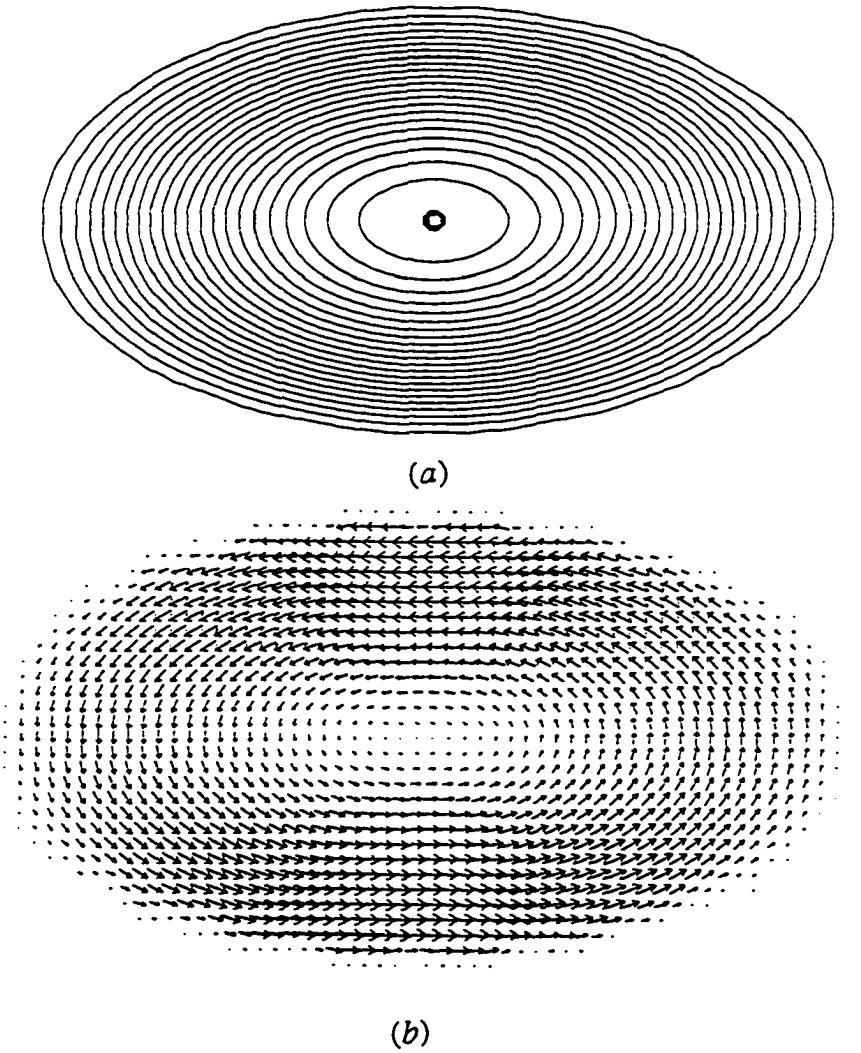

(*a*)

(*b*)

Fig. 5.6 — (Model C13) The same as in fig. 5.4 but with high value of vortensity parameter. The internal velocity is prograde everywhere. (a) and (b) are the streamlines and velocity field respectively.

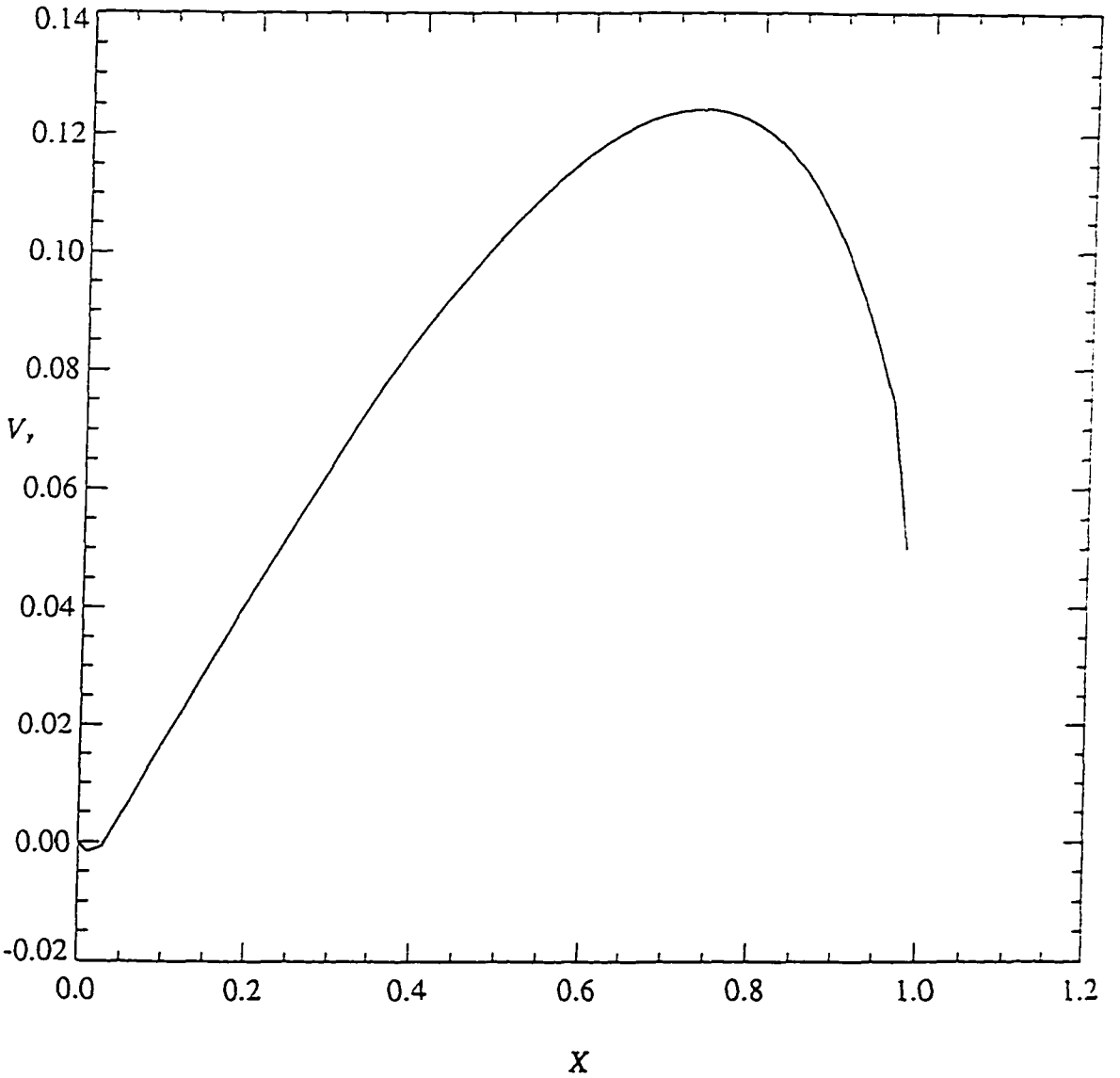

(c)

Fig. 5.6 —The y-component of the flow on the x-axis.

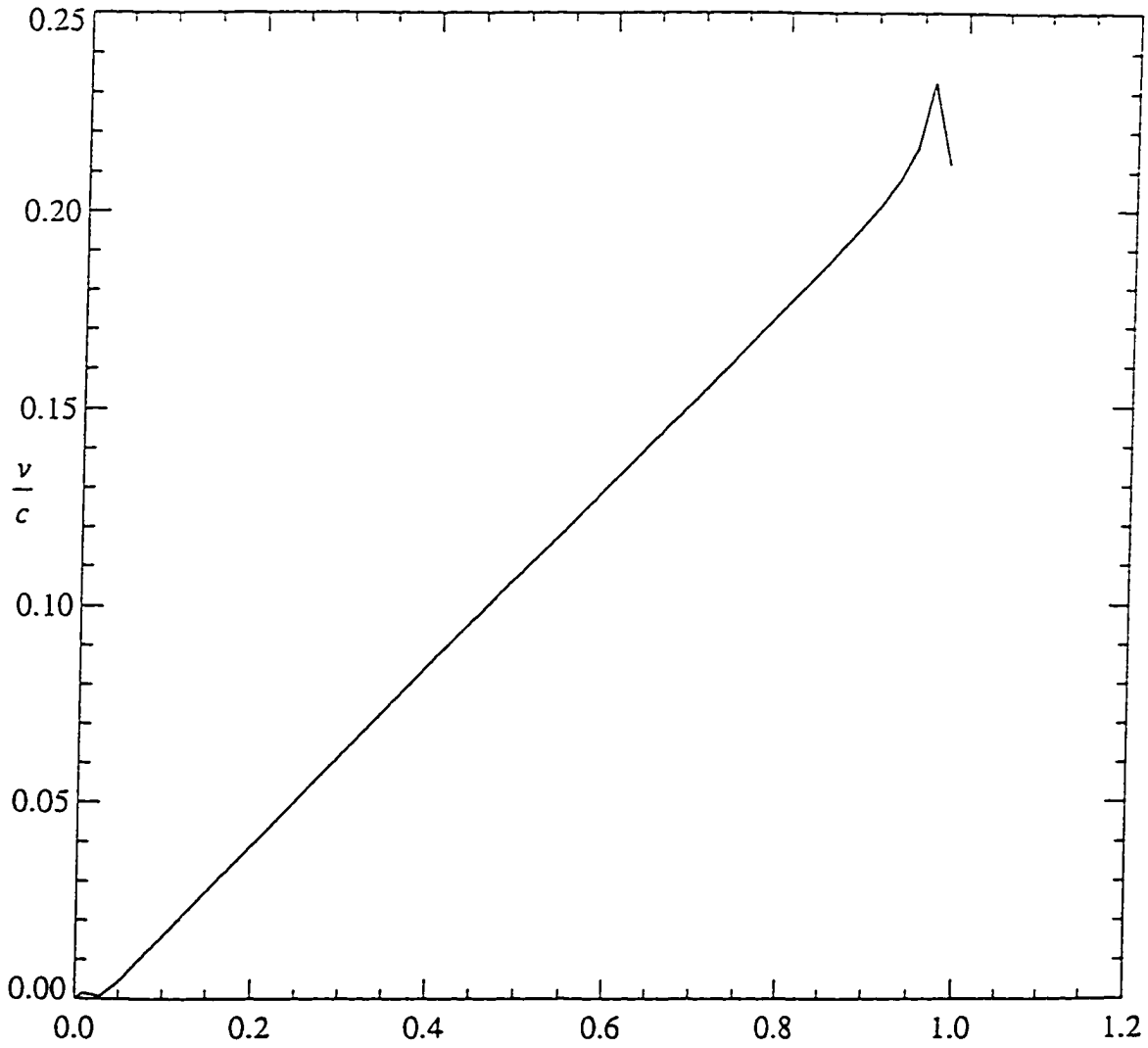

Fig. 5.6 — The dimensionless ratio v/c on the x-axis.

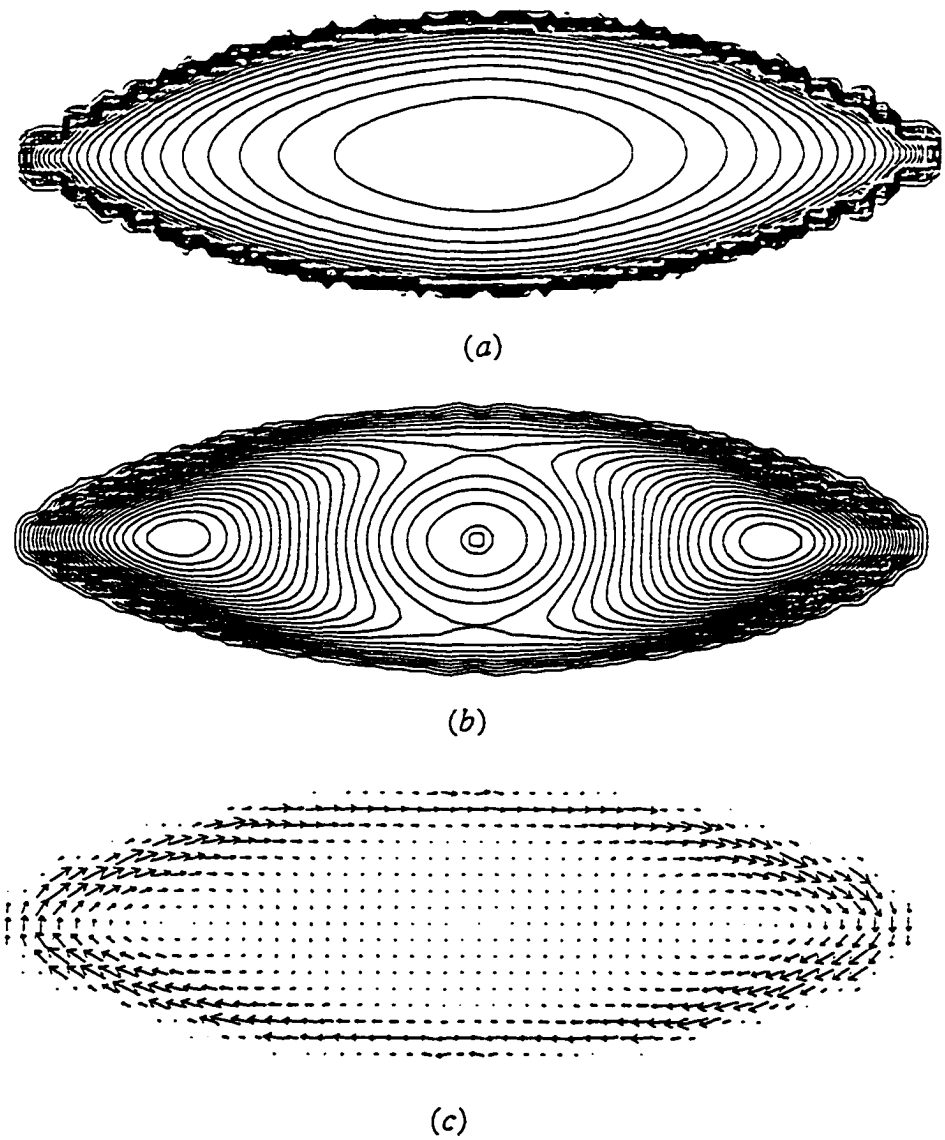

Fig. 5.7 — (Model C07) A cylindrical polytrope at a smaller axis ratio. (a), (b), and (c) are as before the density, streamlines and the flow respectively.

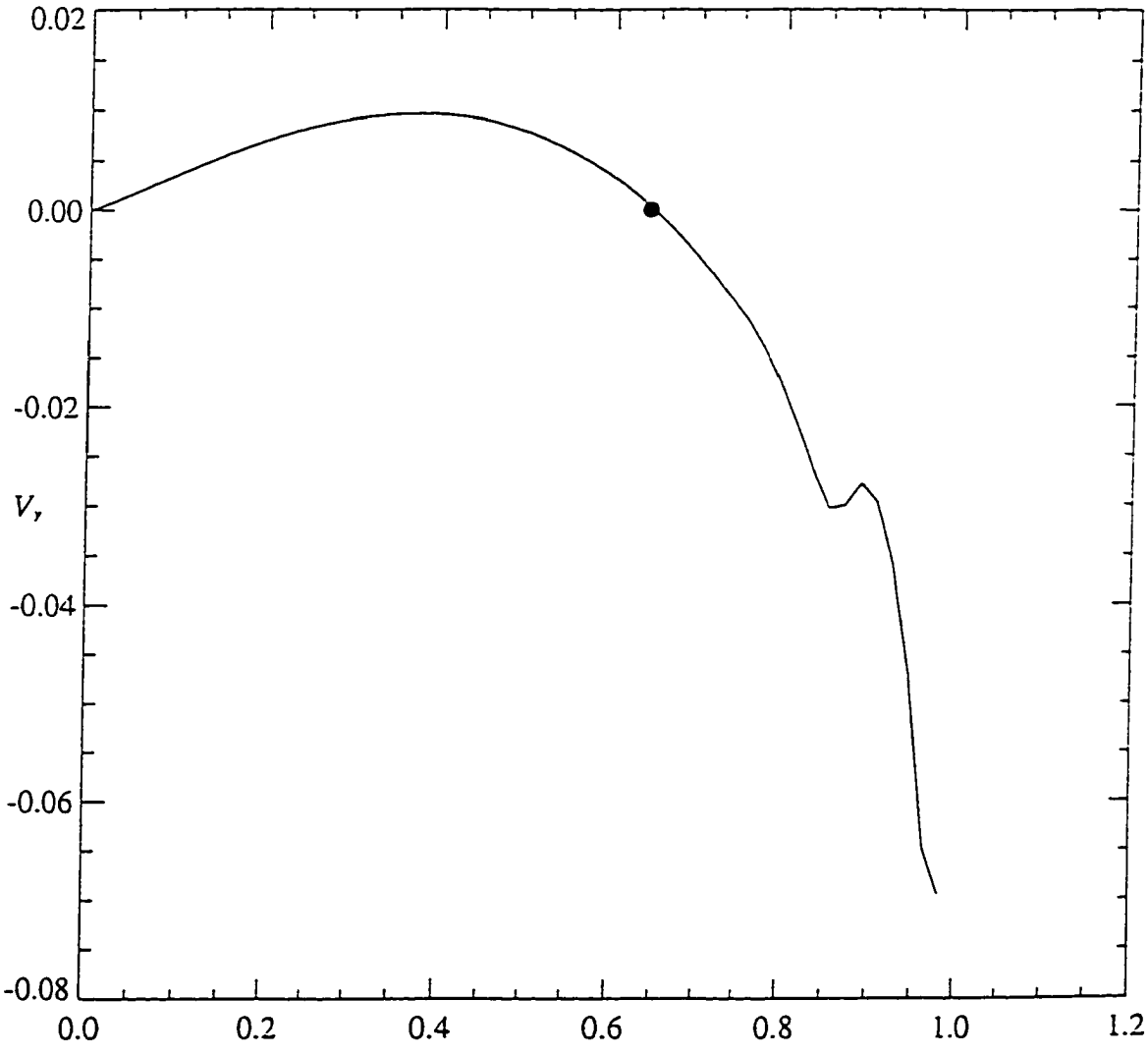

Fig. 5.7 — The y-component of flow on the x-axis.

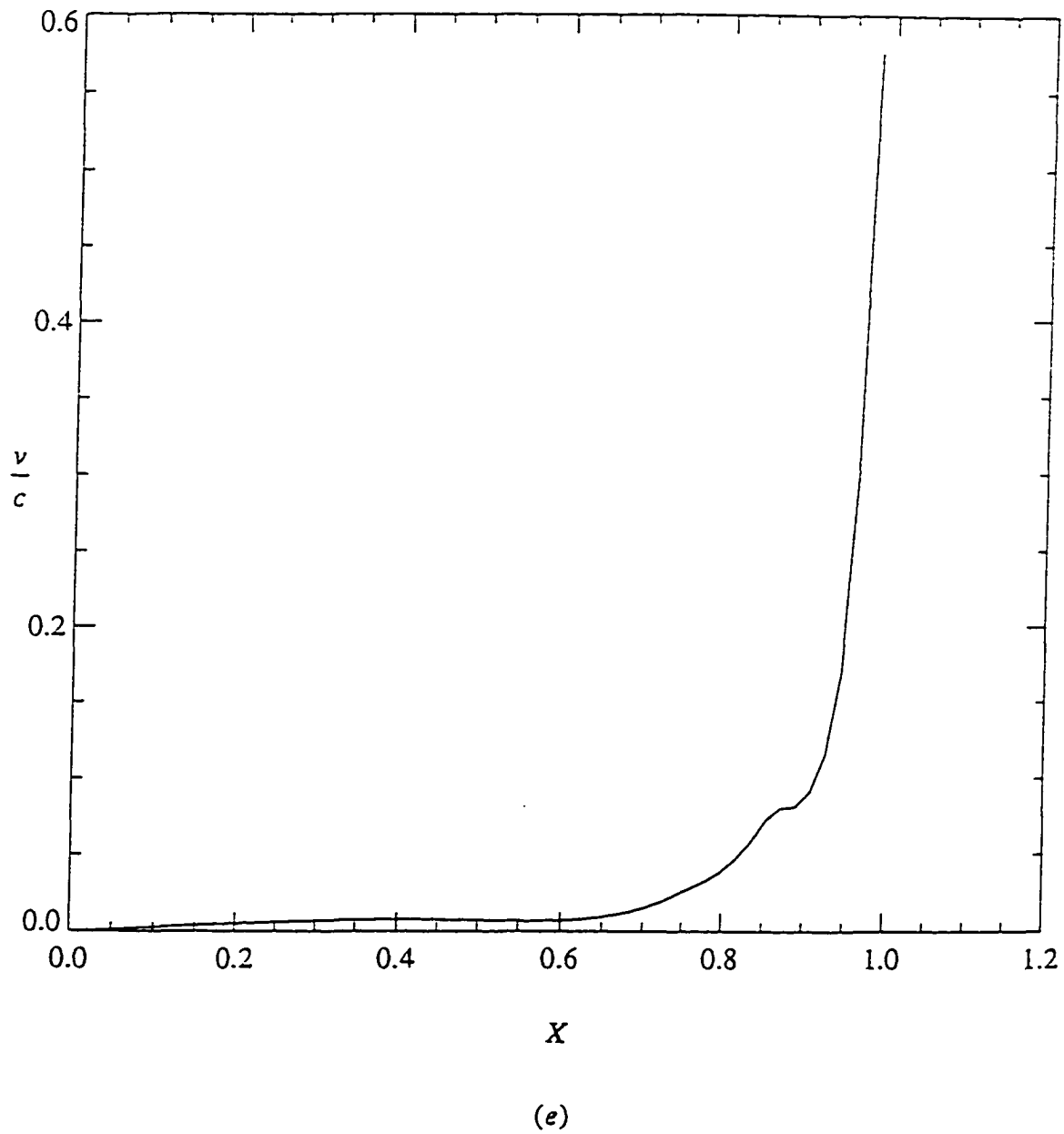

Fig. 5.7 — The dimensionless ratio v/c on the x-axis.

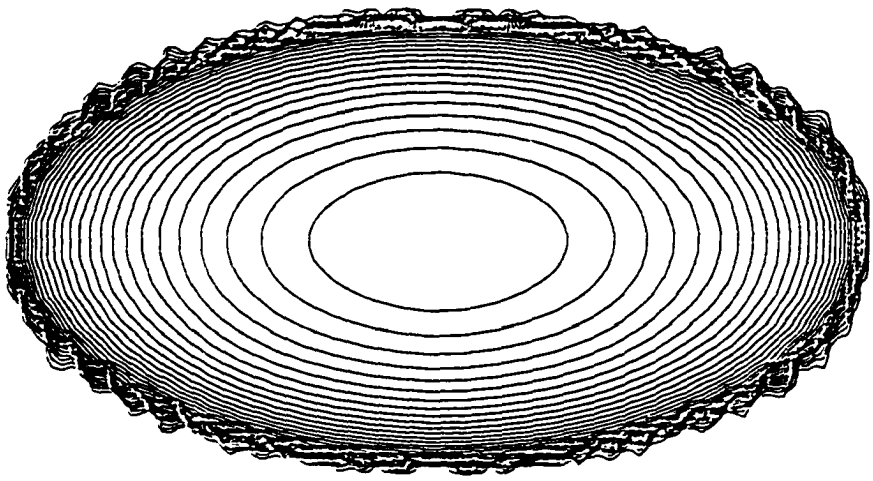

(*a*)

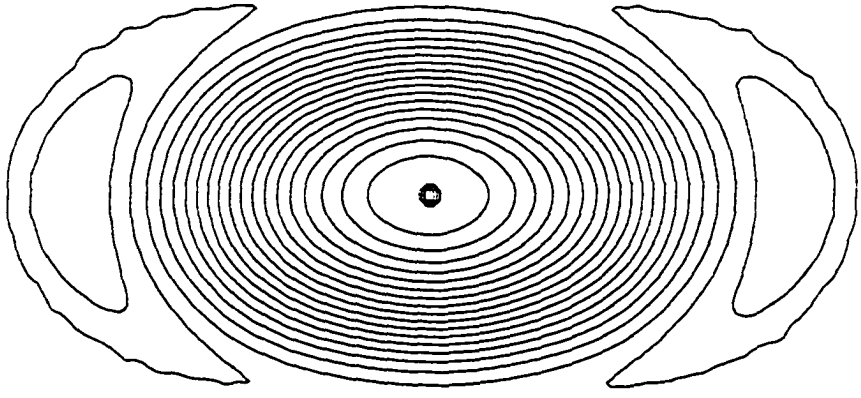

(*b*)

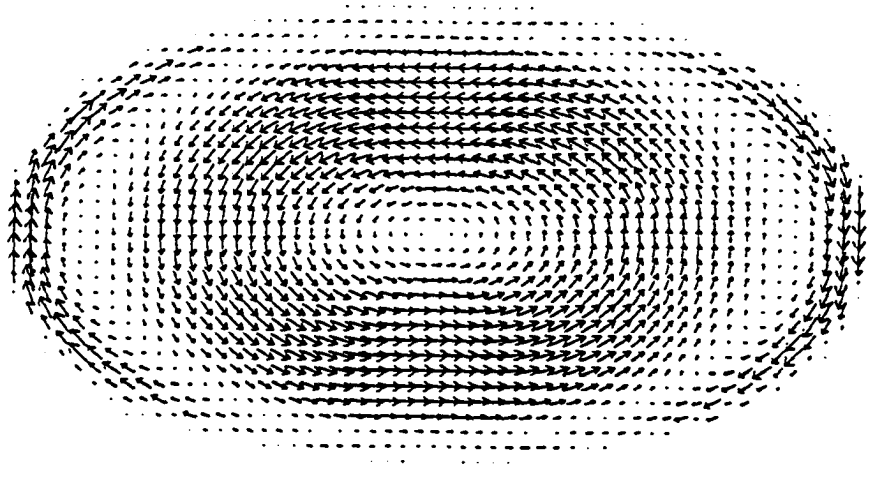

(*c*)

Fig. 5.8 — (Model C20) A cylindrical configuration with polytropic index n = 0.4, and vortensity parameter $C_0 = 4.0$.

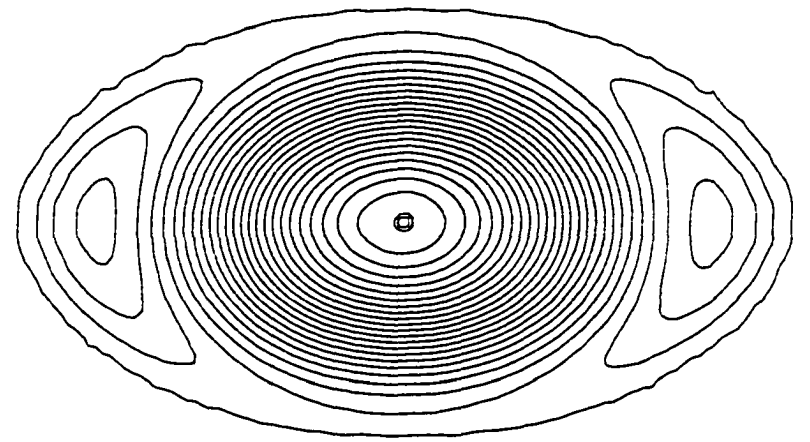

(*a*)

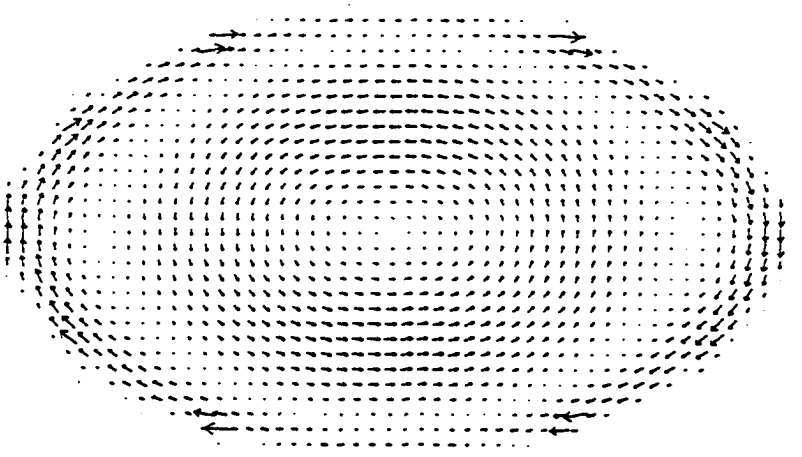

(*b*)

Fig. 5.9 — (Model C22) The same as in fig. 5.8 but with higher polytropic index n = 0.6.

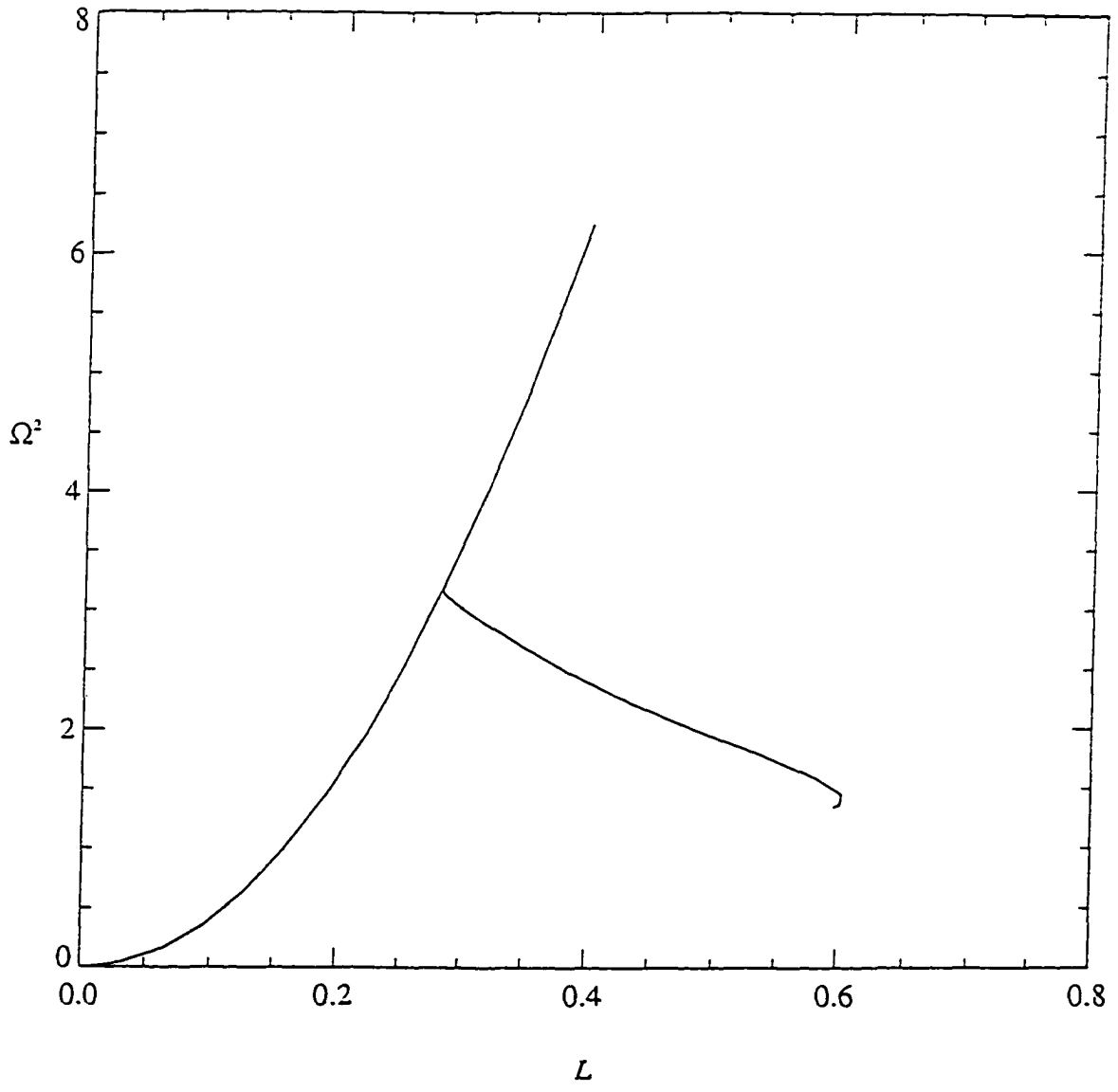

Fig. 5.10 — Two sequences of uniformly rotating, incompressible cylinders in the (Ω^2, L) - plane, where L is the total angular momentum. At L = 0.28 the nonaxisymmetric sequence bifurcates from the axially symmetric sequence.

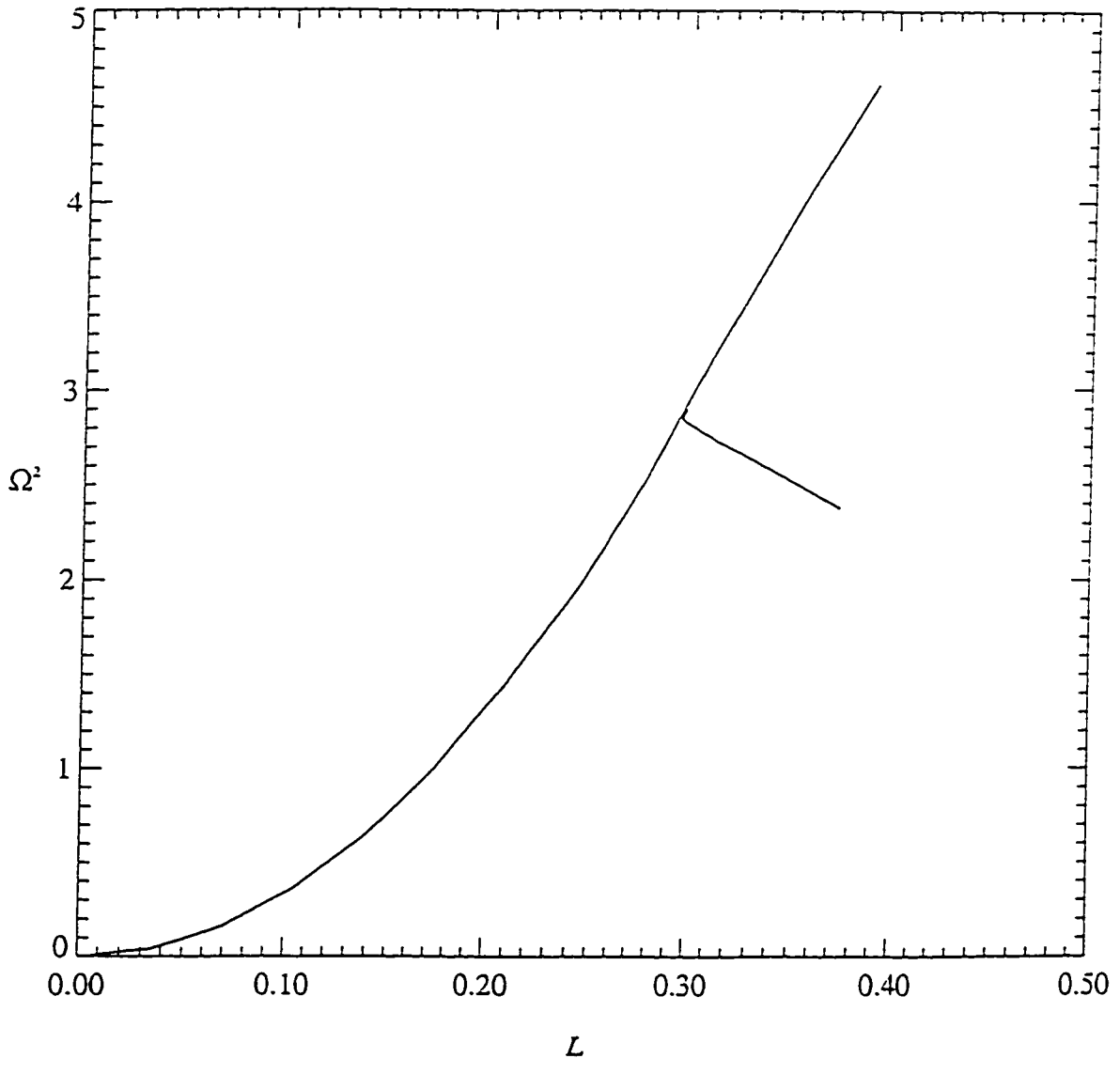

Fig. 5.11 — The compressible analog of fig. 5.10 with polytropic index n = 0.2. Both sequences terminate at smaller values along the horizontal and vertical axes.

5.2 Two-Dimensional Disks

The equilibrium structure and stability analysis of a special class of two-dimensional disks were studied by Weinberg and Tremaine (1983). They considered two-dimensional analogs to Riemann S-type ellipsoids as simple fluid models for galactic bars. They studied their equilibrium and evolution under the effect of various forces and other galaxy components. In a related work, Weinberg (1983) identifed their normal modes and carried out their stability analysis. In these analyses, the fluid density and gravitational potential were prescribed by analytical expressions and the internal flow was linear in the coordinates.

Our two-dimensional equilibrium disk structures, on the other hand, are not derived in any relation to the classical ellipsoidal works. They are, instead, solutions to the nonlinear momentum equation governing the flow of general two-dimensional compressible fluid systems. None of the global physical quantities are known in advance and are determined after the models have converged. They are the generalization of the previous methods.

We will proceed by constructing several compressible disk sequences as we did with cylinders. The disk sequences, although similar to the Riemann sequence, differ in some significant aspects. The internal flow in the Riemann sequence is always a simple linear function of the coordinates. As we have seen above in the cylindrical models, the flow in our compressible structures could become highly nonlinear and complex due to presence of vortices and stagnation points. As we construct the

TABLE 5.2
TWO-DIMENSIONAL DISK CONFIGURATIONS

#	n	b/a	C_0	C	Ω	L	T/|W|
D01	0.0	0.064	4.0	1.613	1.102	0.571	0.282
D02	0.0	0.064	5.0	2.533	1.097	0.595	0.321
D03	0.0	0.156	4.0	1.375	1.181	0.566	0.279
D04	0.0	0.229	4.0	0.998	1.329	0.454	0.287
D05	0.0	0.339	4.0	0.940	1.355	0.413	0.273
D06	0.0	0.523	1.0	-1.268	1.412	0.173	0.083
D07	0.0	0.523	2.0	-0.564	1.402	0.231	0.126
D08	0.0	0.523	3.0	0.137	1.402	0.289	0.194
D09	0.0	0.523	4.0	0.843	1.399	0.348	0.285
D10	0.4	0.064	1.5	-0.755	0.880	0.438	0.139
D11	0.4	0.064	2.0	-0.371	0.898	0.457	0.152
D12	0.4	0.064	4.0	1.336	0.906	0.563	0.223
D13	0.4	0.229	4.0	0.821	1.109	0.491	0.236
D14	0.4	0.339	3.0	-0.151	1.245	0.383	0.182
D15	0.4	0.523	2.0	-0.808	1.235	0.232	0.099
D16	0.4	0.523	3.0	-0.211	1.266	0.292	0.159
D17	0.4	0.523	4.0	0.572	1.205	0.348	0.236
D18	0.4	0.633	3.0	-0.210	1.258	0.263	0.157
D19	0.4	0.798	3.5	0.133	1.265	0.279	0.218
D20	0.4	0.798	4.0	0.835	1.101	0.311	0.273
D21	0.7	0.193	3.0	-0.338	1.129	0.614	0.203
D22	0.7	0.523	2.0	-1.037	1.165	0.232	0.082
D23	0.7	0.523	3.0	-0.615	1.228	0.297	0.133
D24	0.7	0.523	3.5	-0.340	1.214	0.325	0.164
D25	0.7	0.523	4.0	0.492	1.167	0.355	0.204
D26	0.8	0.229	4.0	0.249	1.023	0.546	0.210
D27	0.8	0.229	4.5	0.359	1.080	0.381	0.229
D28	1.0	0.229	4.0	-0.046	0.950	0.573	0.195
D29	1.0	0.523	4.5	-0.241	1.147	0.398	0.210
D30	1.0	0.523	5.0	0.168	1.096	0.397	0.233
D31	1.3	0.229	4.0	-0.231	0.712	0.595	0.155

n is the polytropic index, b/a is the axis ratio, C_0 is the vortensity parameter, C is the internal circulation, Ω is the uniform frame angular velocity, and L is the total angular momentum.

corresponding disk models below, we will see that these internal fluid motions will become even more complex as the axis-ratio drops towards zero.

In sharp contrast to the infinite cylinders described in § 5.1 the two-dimensional disks show a wide variety of configurations. The global physical quantities for those disks parameterized by n, b/a, and C_0 have been summarized in Table 5.2.

In Figure 5.12 we show some properties of disk model D15 with n = 0.4, b/a = 0.523, and C_0 = 2.0. The internal flow is retrograde. Figures 5.13 and 5.14 show two additional disk models (D16 and D17) with the same values of n and b/a as model D15, but with C_0 = 3.0 and 4.0, respectively. These models exhibit a behavior that is very similar to the cylinder model shown earlier (Figs. 5.4-5.6). The three types of flow topologies reappear as we go from low values of the vortensity, to intermediate, then to high values. The corresponding flow patterns are reflected in the retrograde, vortical, and the prograde internal motions.

The vortensity of the fluid correlates well with the internal kinetic energy of these fluid configurations in the sense that low and high vortensity configurations correspond to configurations with smaller and larger T/|W|, respectively. As mentioned earlier, the disks span a larger parameter space than do the cylinders. We are able to construct disk sequences with higher polytropic indices and also different geometries as we will see in the next several figures.

As the axis-ratio decreases, the disks do not seem to maintain their elliptic-like boundaries. This is evident in figure 5.15 which shows a model (D14) with the same parameters as model D16 (Fig. 5.13) but with b/a = 0.339. The boundary has

assumed a more rectangular, box-shaped geometry with round corners. As we go to even smaller axis-ratios this change in geometry becomes even more extreme. For example, Figure 5.16 shows a disk (D13) with b/a = 0.229. (This model otherwise has the same parameters as model D17, shown in Fig. 5.14.) This equilibrium configuration has a dumbbell geometry with two off-center density maxima. Figure 5.17 (model D28) shows another dumbbell with the same axis ratio and value of C_0 as model D13 but with a polytropic index n = 1.0. In this more compressible system, the internal flow is modified to accommodate two off-centered vortices close to the surface.

The next three figures, 5.18, 5.19, and 5.20, illustrate even more extreme dumbbell configurations (models D10, D11, D12, respectively). Indeed, the depicted objects are more properly described as loosely connected, equal-mass binary disks. In each of these systems, n = 0.4 and b/a = 0.064, but the vortensity C_0 = 1.5, 2.0, and 4.0 respectively. As before, the three internal flow topologies show up, but in this group of models the vortex patterns appear well-defined separately in each "binary" mass component. The flow topology shown in figure 5.19, in particular, is quite complicated. The two components of the dumbbell seem almost independent with their own set of vortices and stagnation points orbiting around a mutual axis of rotation. The components are not completely independent however, as they still share the origin where there is still a small exchange of fluid between the two components. The fluid in the outer-most layers, near the surface,

moves around both components in a retrograde fashion as it encloses all the vortices and the stagnation points.

Figures 5.21 and 5.22 show two disks (D23 and D29) with b/a = 0.523 but with different degrees of compressibility and different values of the vortensity: n = 0.7 and 1.0; C_0 = 3.0 and 4.5, respectively. In general, for a given disk geometry, the internal flow decreases quantitatively as the compressibility increases.

Although elliptic disks with very small axis-ratios may indeed exist, they appear to be nonexistent in our simulations. Instead, our configurations with very small axis ratios all converge to dumbbells, to the exclusion of elliptical configurations. This may indicate that, in general, dumbbells are more energetically favorable than elliptical disks. Similarly, the dumbbells themselves may be less favorable than the binaries and may become susceptible to breakup into binary systems.

The two-dimensional nature of the disk models and the change in their geometry as we move to smaller axis-ratios may provide an explanation to the differences we saw earlier in figures 5.2 and 5.3. In the CIES, the ellipsoidal boundaries are maintained at all axis-ratios. Clearly, this is not the case with the two-dimensional disks. For sufficiently small axis-ratios they tend to become deformed and dumbbell shaped. This change in the geometry at smaller axis ratios coupled with the nonlinear nature of the internal flow, especially at high |C|, will cause the sequence to behave differently from a purely ellipsoidal sequence. Even at larger axis ratios, the boundary may not be an exact ellipse. In fact, these objects are unlikely to possess

surface boundaries that can be described by quadratic or, in general, a polynomial based boundary.

In figure 5.23, Ω^2 is plotted as a function of the total angular momentum L for a sequence of models with n = 0.4 and fixed vortensity C_0 = 3.5. This ellipse-dumbbell sequence is the two-dimensional disk analog of the three-dimensional incompressible dumbbell-binary sequence (Christodoulou, Kazanas, Shlosman, and Tohline, 1995). The larger axis-ratios represent the elliptical disks, while the smaller values are dumbbells. As the axis-ratio approaches zero, the binary sequence bifurcates from the dumbbell sequence which is not shown in the plot. The maximum total angular momentum L = 0.55 occurs at Ω = 1.0.

Throughout this chapter a variety of differentially rotating polytropes has been constructed by varying the vortensity C_0 to obtain several types of internal motions with varying degrees of amplitudes and topologies. The higher order vortensity parameter (C_1) in general, tends to have much less impact on the dynamics of the internal flow. Only at high C_0 and polytropic indices ($n \geq 0.8$) does it assume a more critical role. At lower values of n (≤ 0.5) a rather large variation of C_1 will be necessary to make a visible change in the flow and the total circulation. The internal flow is further affected by the compressibility of the fluid. In general, for a given configuration, the global parameters such as T/|W|, L, and total circulation C will have smaller values at higher polytropic index n.

The fluid vortensity cannot increase to arbitrarily large values irrespective of other physical parameters. The high vortensity values are largely restricted to models with small axis ratios. Furthermore, the maximum allowed vortensity drops at higher polytropic indices.

The presence of internal motions, in general, effects the global physical quantities in equilibrium structures. Uniformly rotating polytropes, for instance, typically have smaller T/|W| for a given polytropic index n compared to the differentially rotating models. For a given axis ratio, there is a maximum polytropic index beyond which the uniformly rotating sequence terminates. To obtain any equilibrium structure beyond the critical value n, it is necessary to have some type of internal motions. This would also allow for higher T/|W| without the need for higher Ω. This is illustrated in table 5.2 for an elliptical disk with b/a = 0.523 (model D27). The corresponding uniformly rotating model terminates at n = 0.8 with T/|W| = 0.071 and Ω = 1.135. The same model with internal flow and a vortensity C_0 = 4.5, and the total circulation C = 0.359, has T/|W| = 0.229, a substantial increase at a slightly smaller frame angular velocity Ω = 1.08. At an even higher vortensity (C_0 = 5.0), T/|W| = 0.235. In this model, the angular momentum from the internal flow accounts for 30% of the total angular momentum. Additionally, with the presence of the internal motions, we are able to go beyond the critical n = 0.8 polytrope and obtain a model with n = 1.0, (model D28). Model D31 shows yet another dumbbell with n = 1.3 and vortensity C_0 = 4.0.

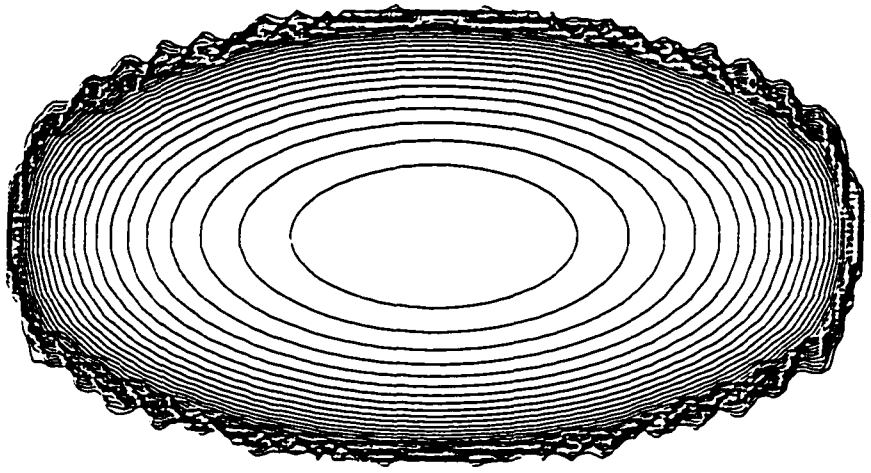

(*a*)

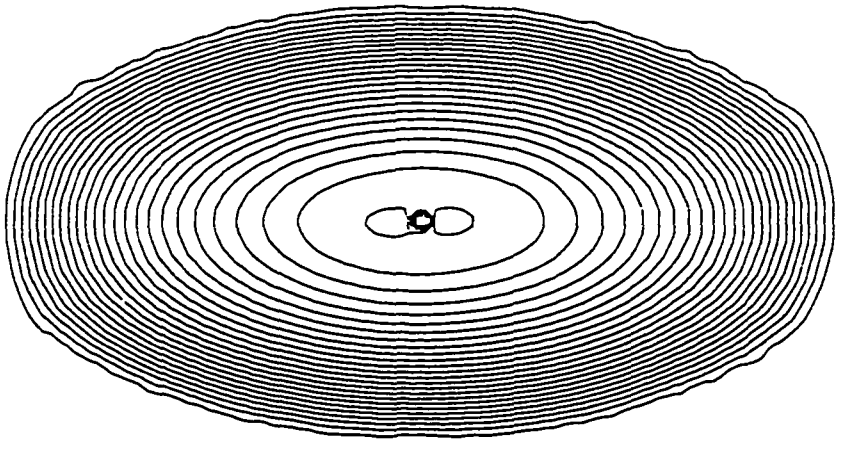

(*b*)

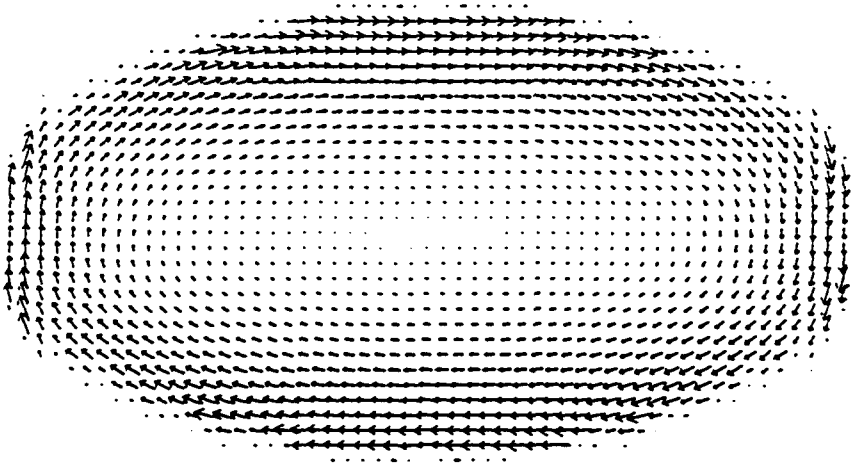

(*c*)

Fig. 5.12 — (Model D15) A two dimensional disk with polytropic index n = 0.4 and low vortensity. (a) the density contours, (b) the streamlines, and (c) the retrograde velocity vector field.

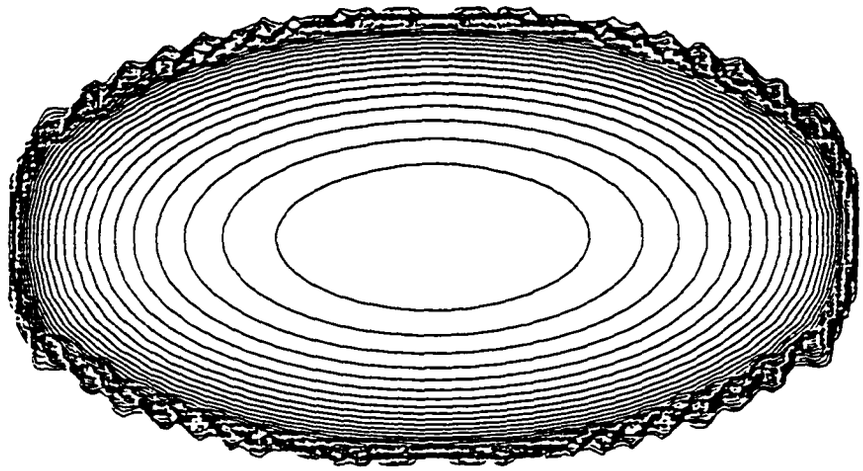

(*a*)

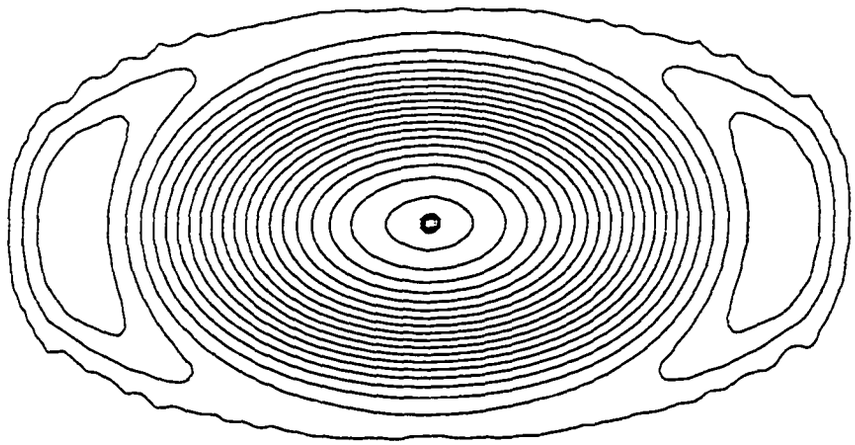

(*b*)

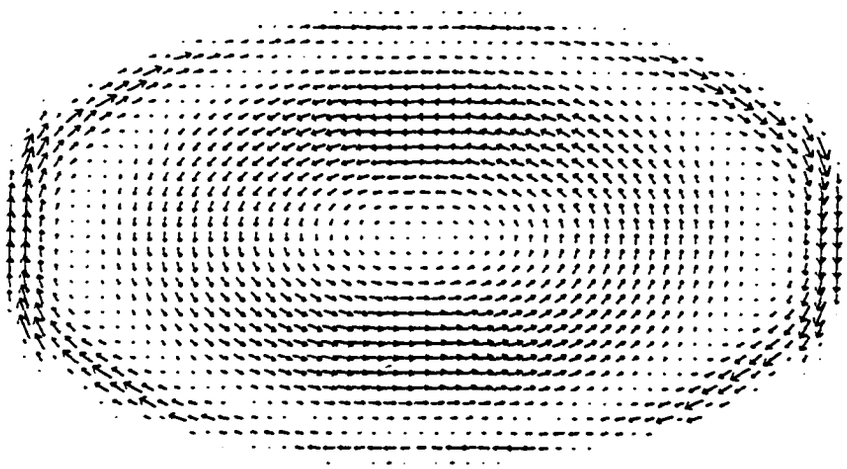

(*c*)

Fig. 5.13 — (Model D16) The same disk as in fig. 5.12 but at higher vortensity. The resulting vortical flow pattern is shown in panels (b) and (c).

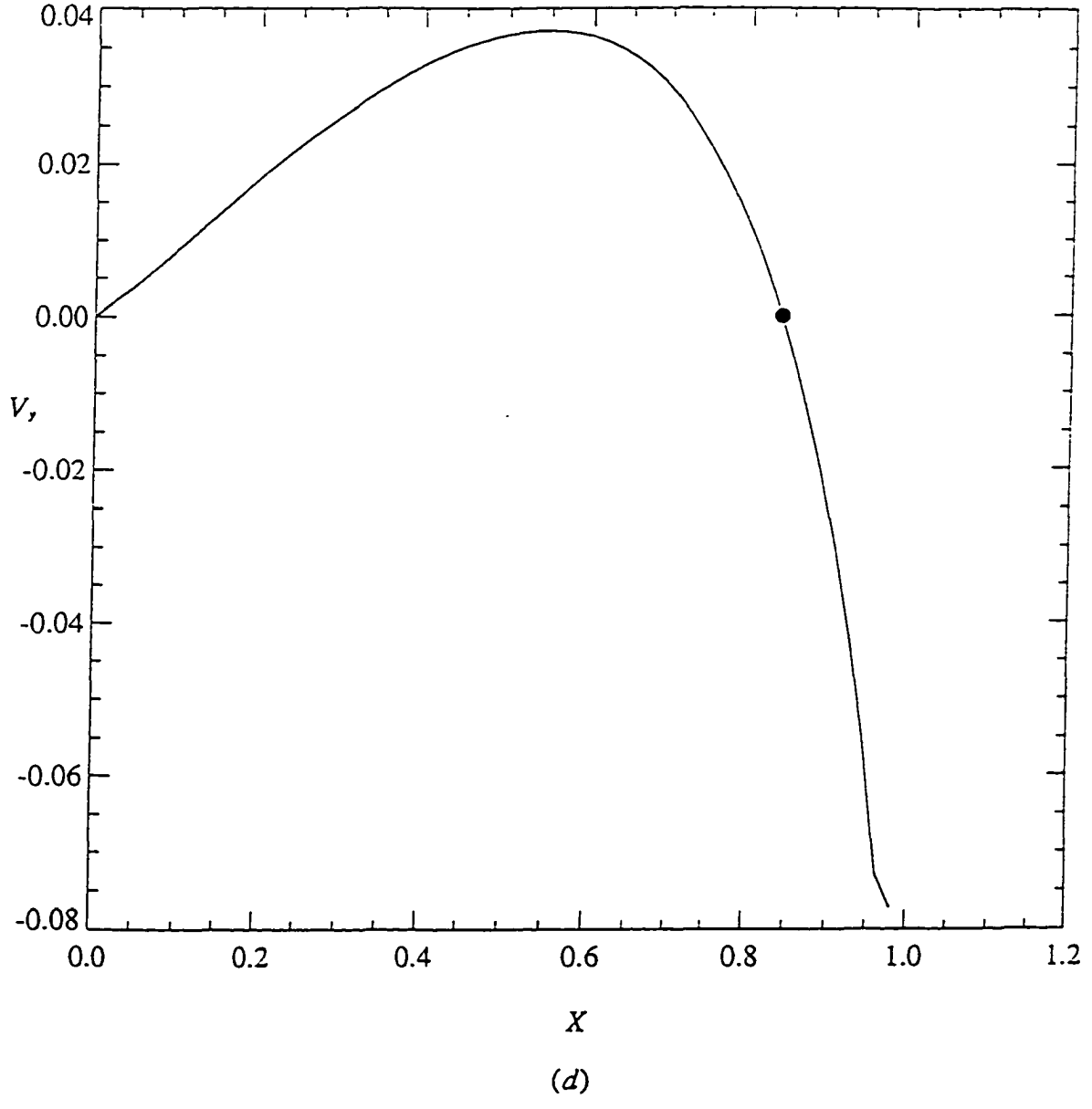

Fig. 5.13 — The corresponding y-component of the flow along the x-axis. The solid circle is the location of the critical point (the off-centered vortex) on the x-axis where internal flow vanishes.

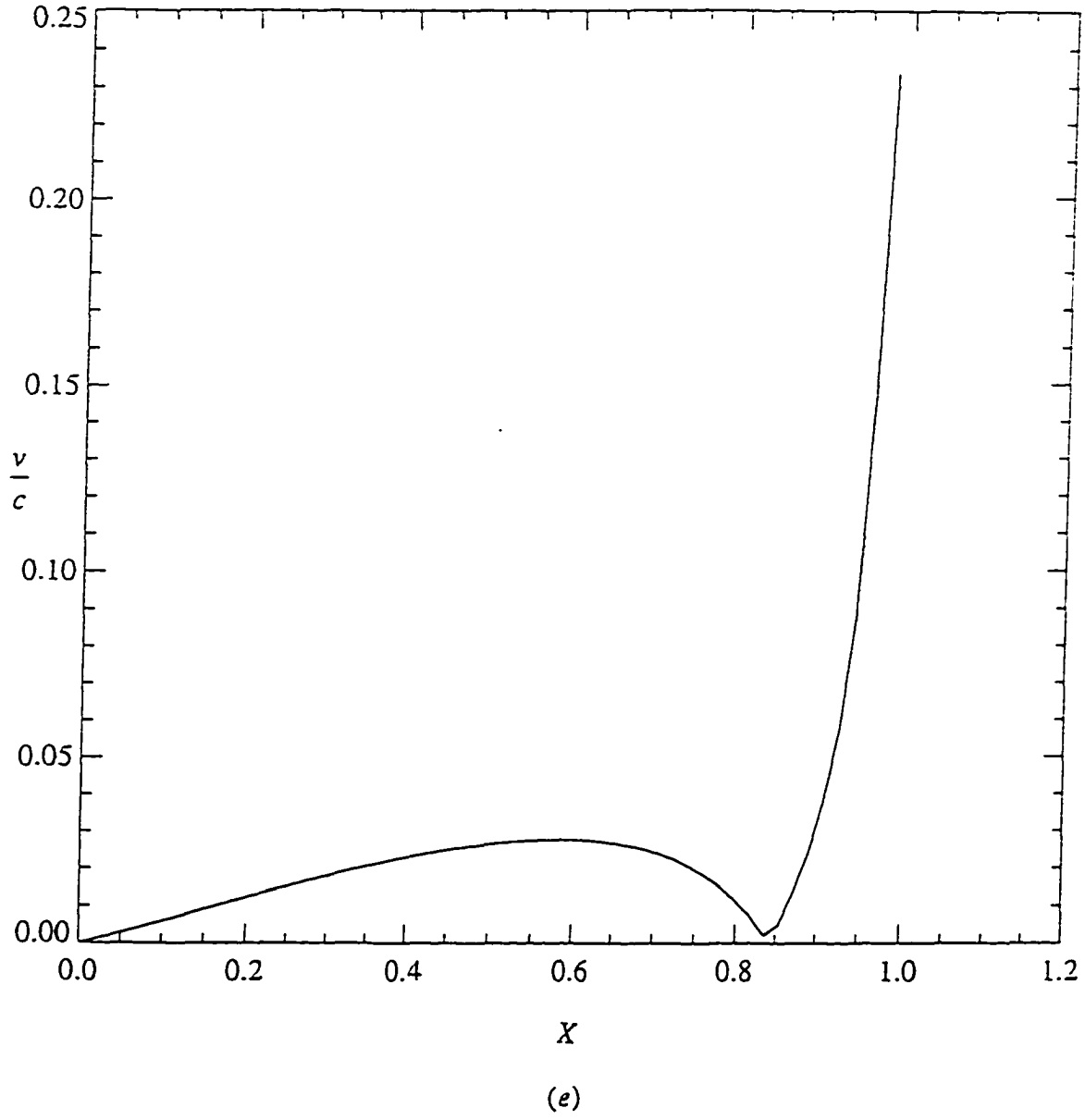

Fig. 5.13 — The dimensionless ratio v/c on the x-axis.

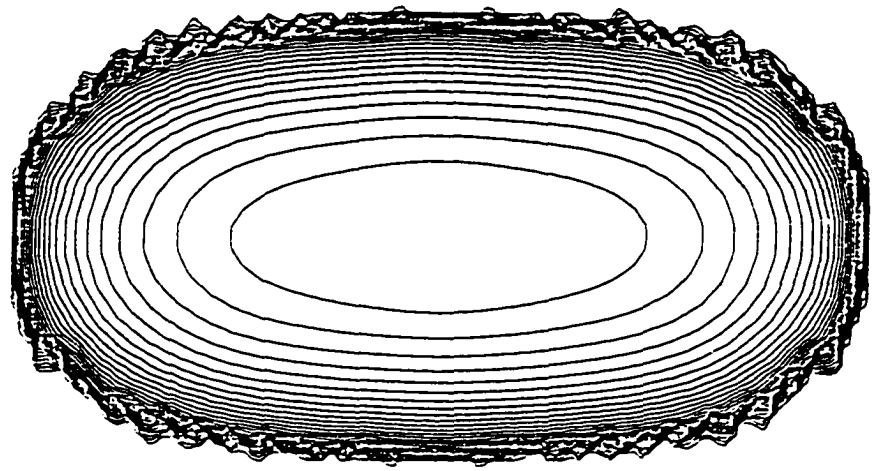

(*a*)

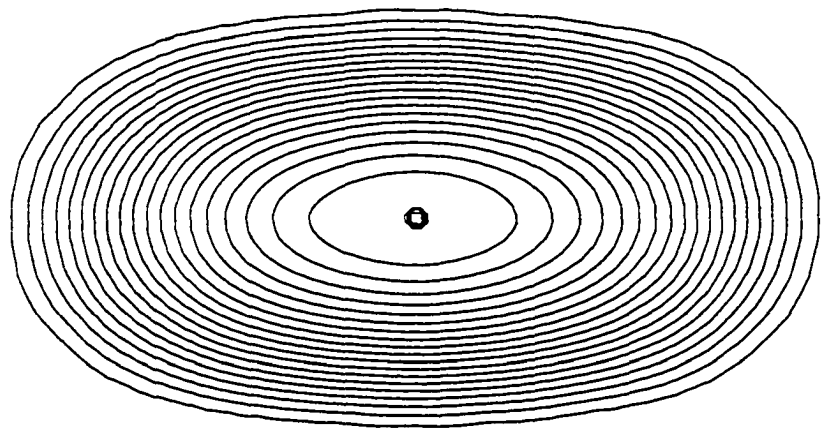

(*b*)

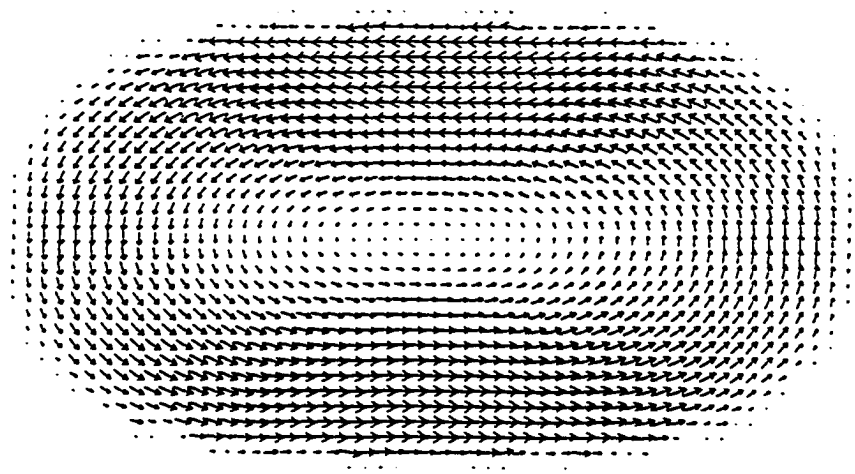

(*c*)

Fig. 5.14 — The same as in fig. 5.13 but at high vortensity. Panel (c) shows the corresponding prograde flow.

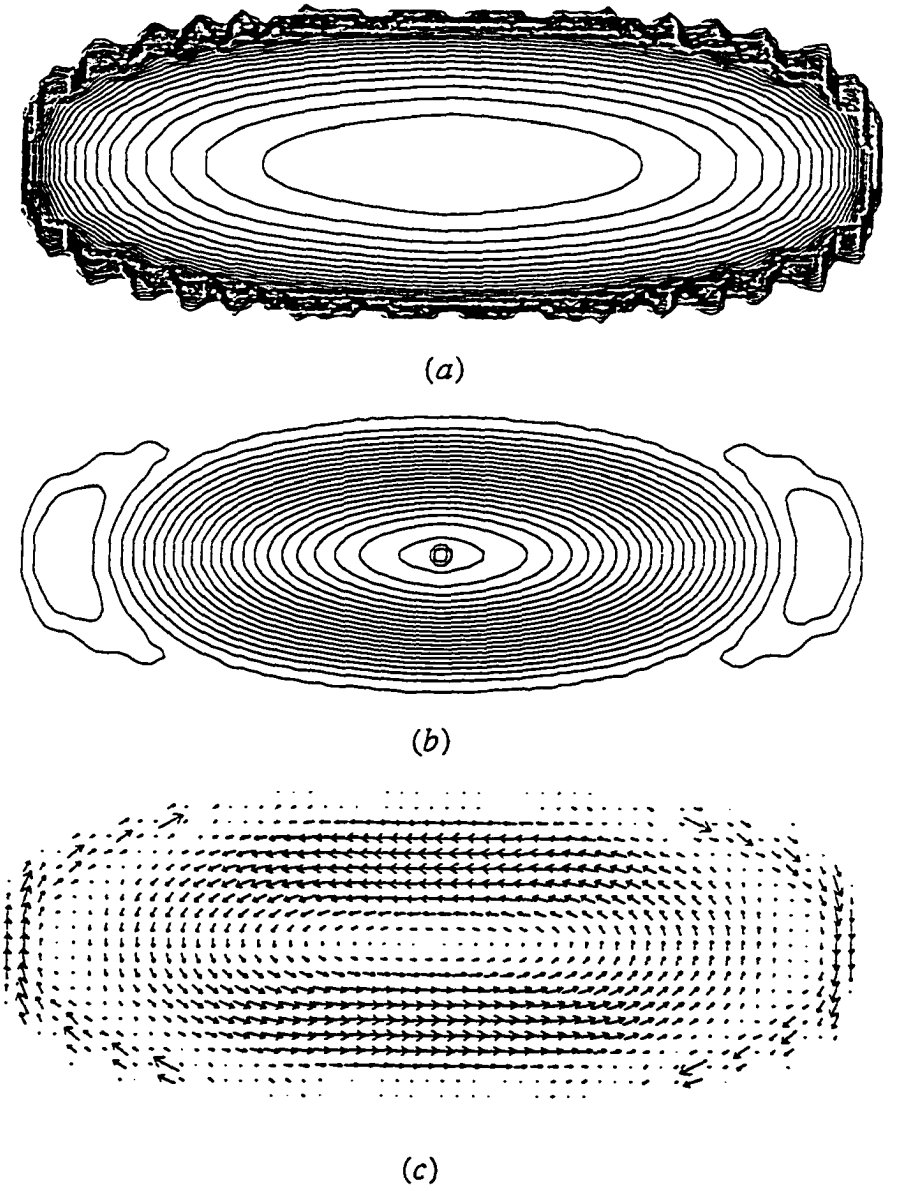

Fig. 5.15 — (Model D14) A disk with a rectangular box geometry and intermediate value of the vortensity parameter.

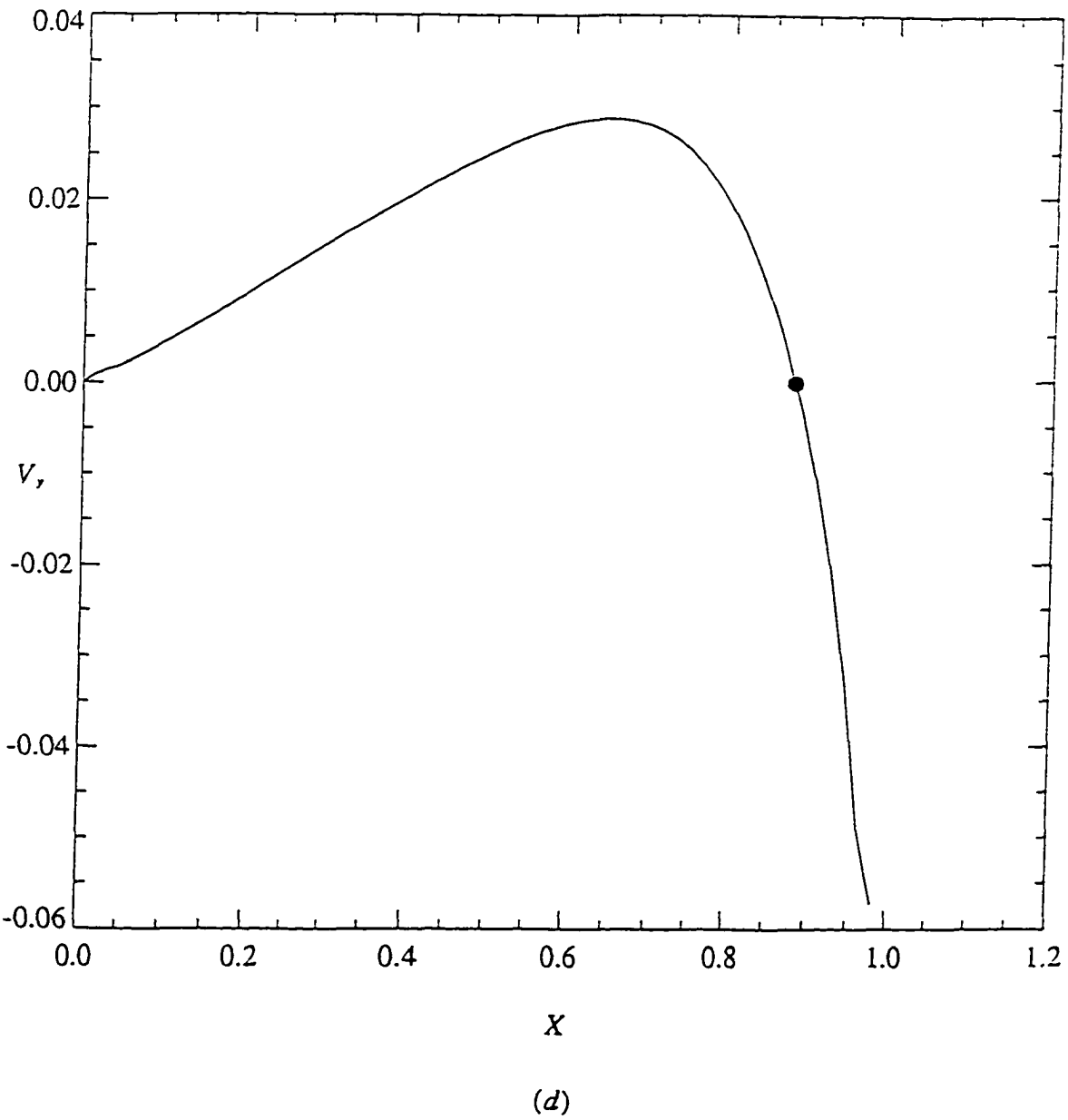

Fig. 5.15 — The y-component of the internal flow on the x-axis.

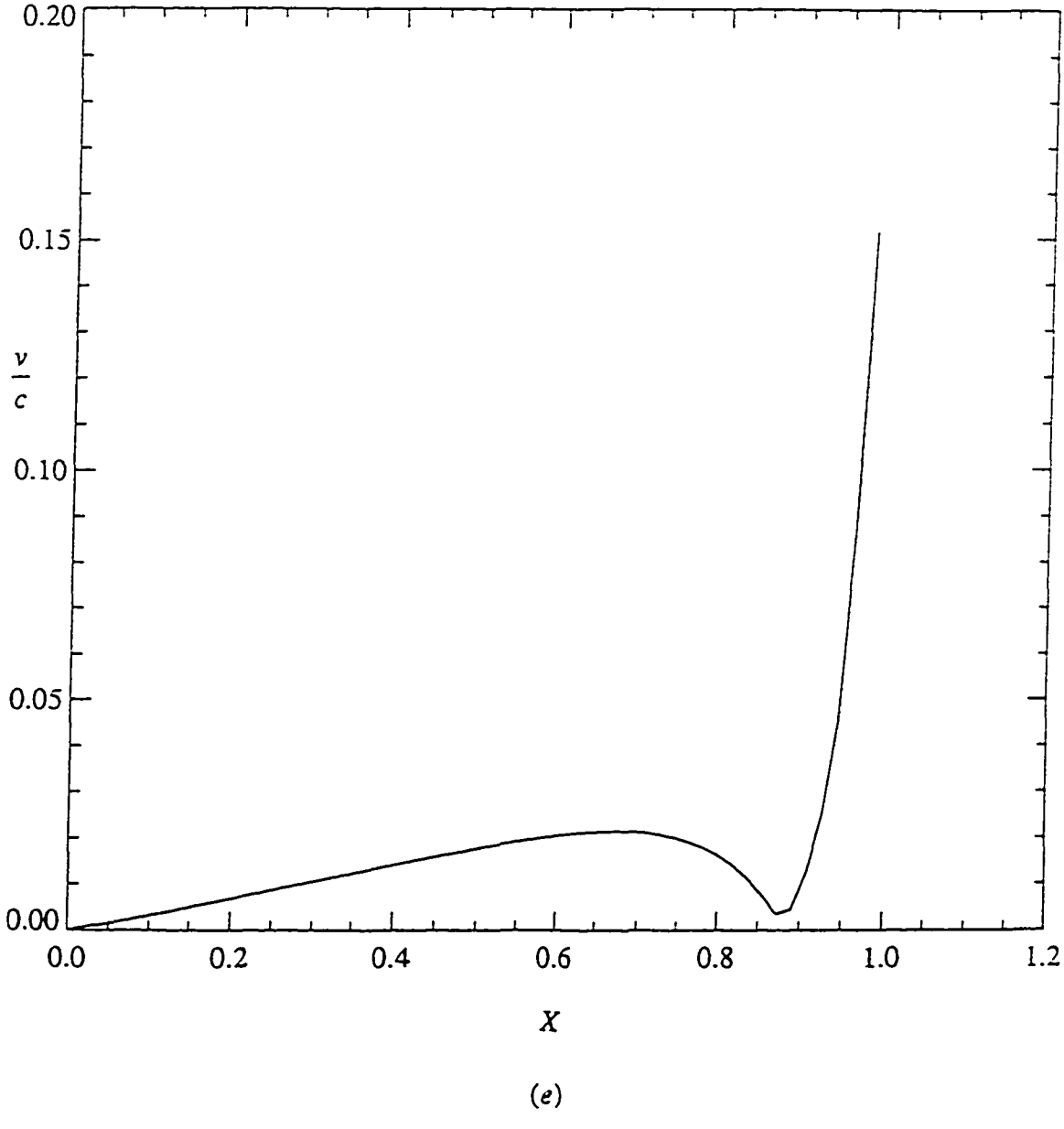

Fig. 5.15 — The dimensionless ratio v/c on the x-axis.

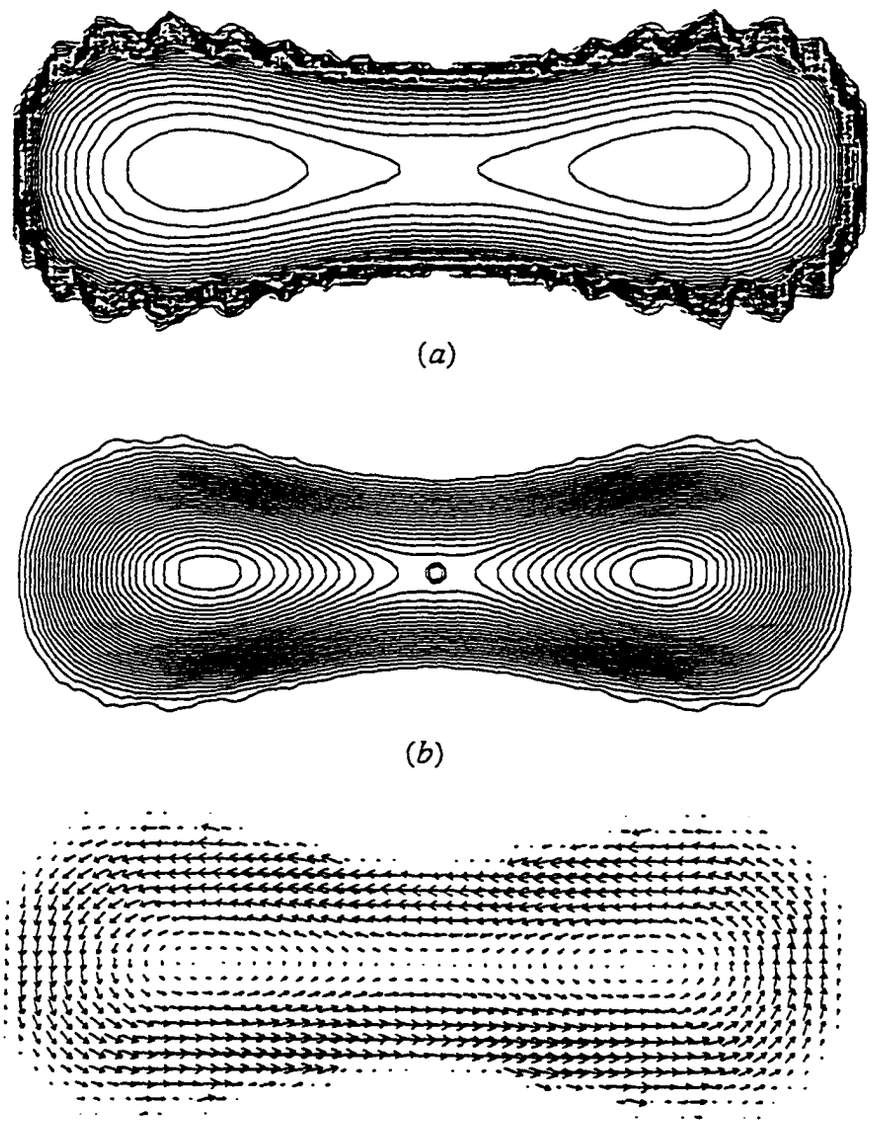

Fig. 5.16 — (Model D13) A disk with a dumbbell geometry and prograde internal flow.

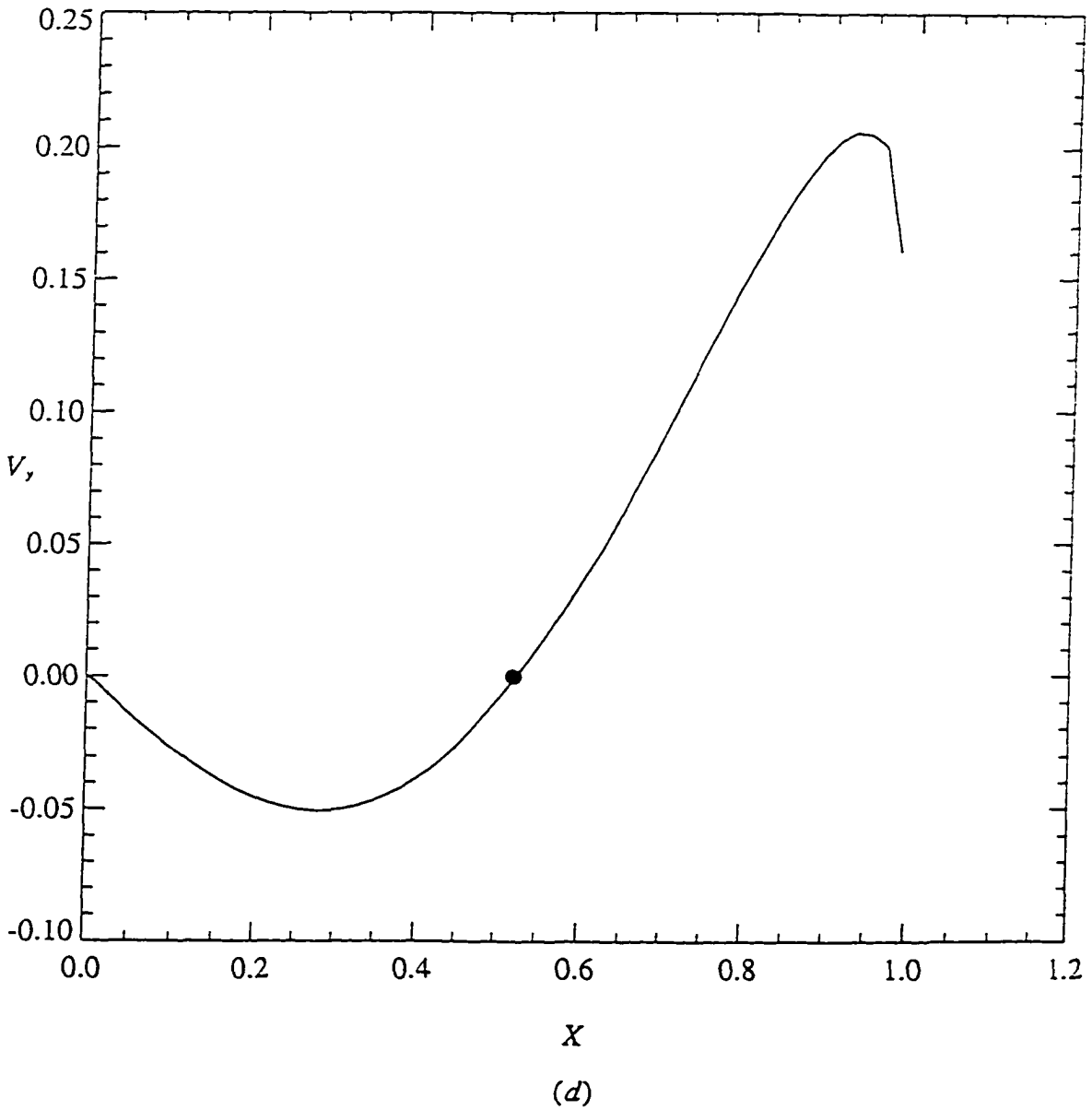

Fig. 5.16 — The y-component of the internal flow on the x-axis

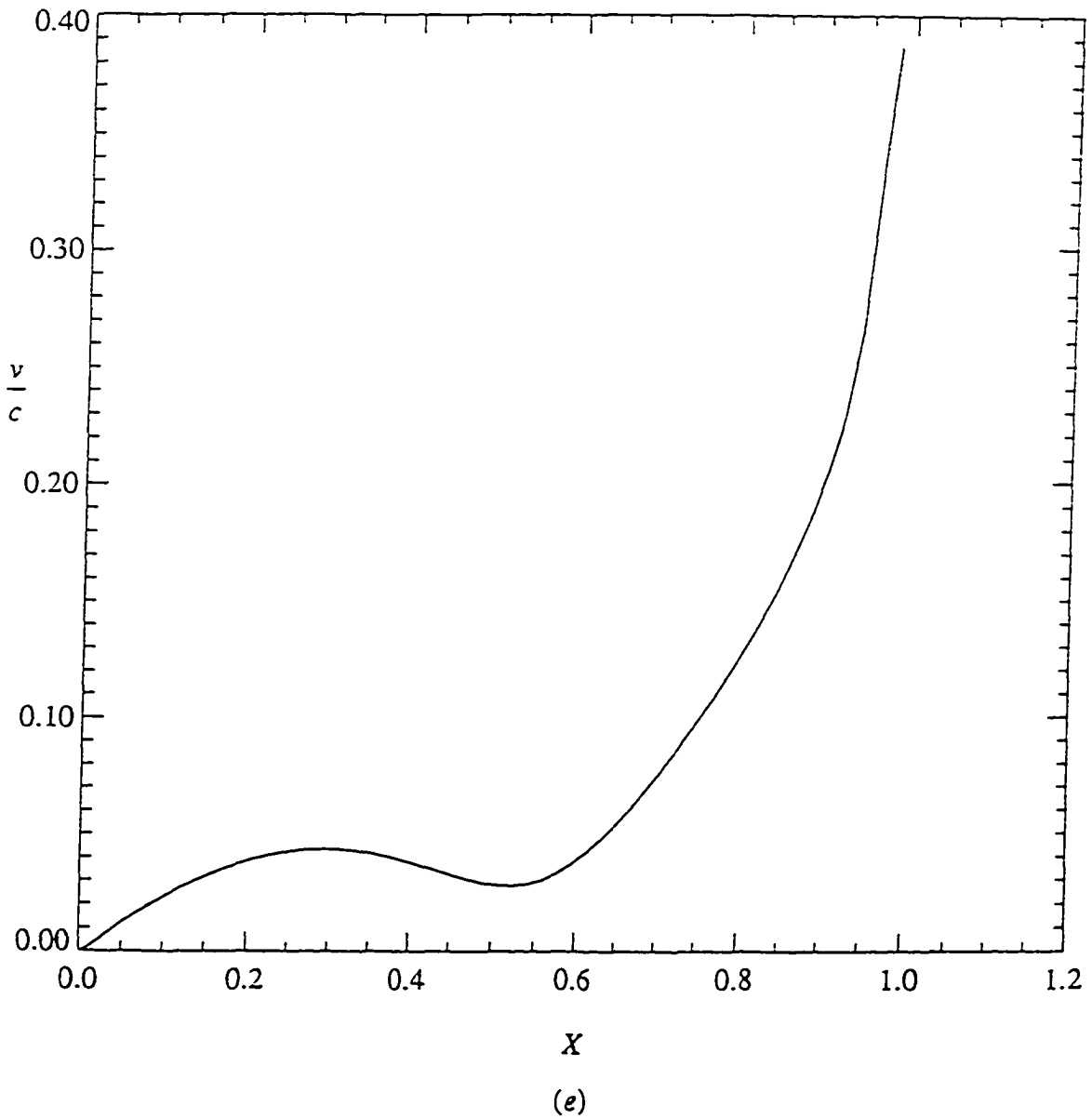

Fig. 5.16 — The dimensionless ratio v/c on the x-axis.

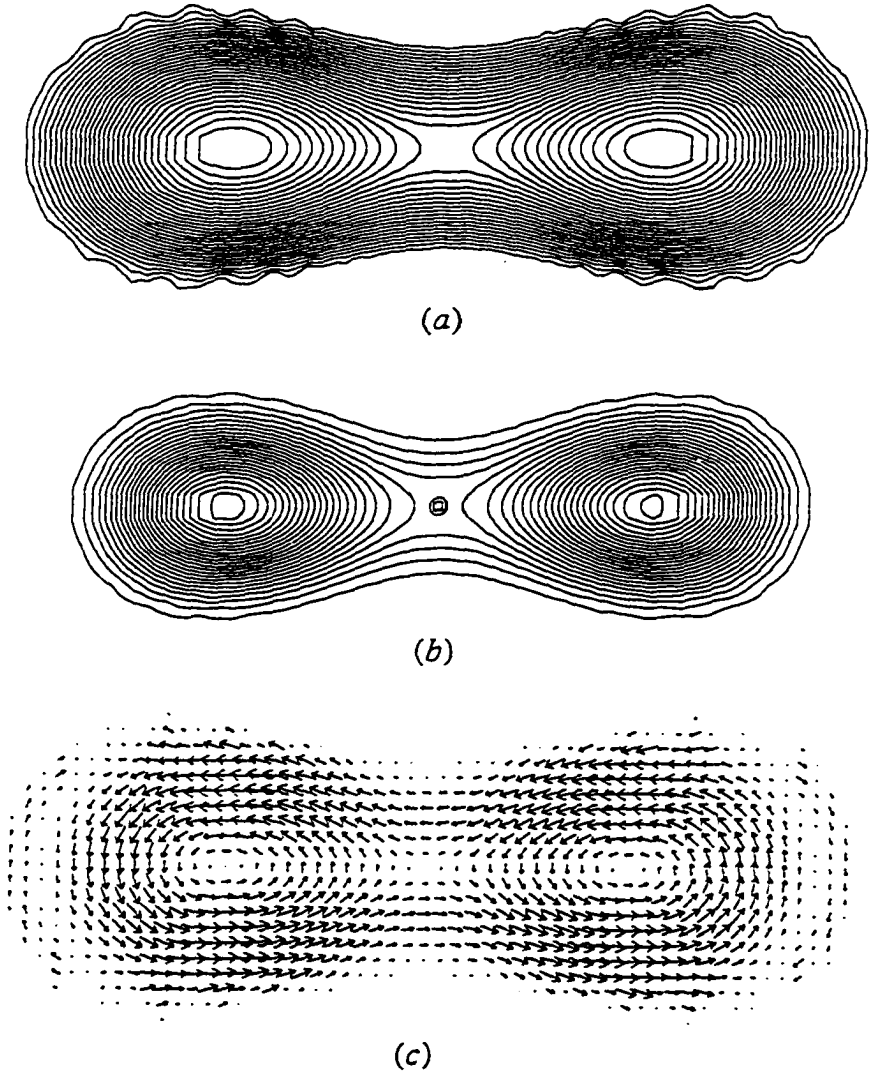

Fig. 5.17 — (Model D28) The same as in fig. 5.16 at an intermediate vortensity. The off-centered vortices appear in panel (c).

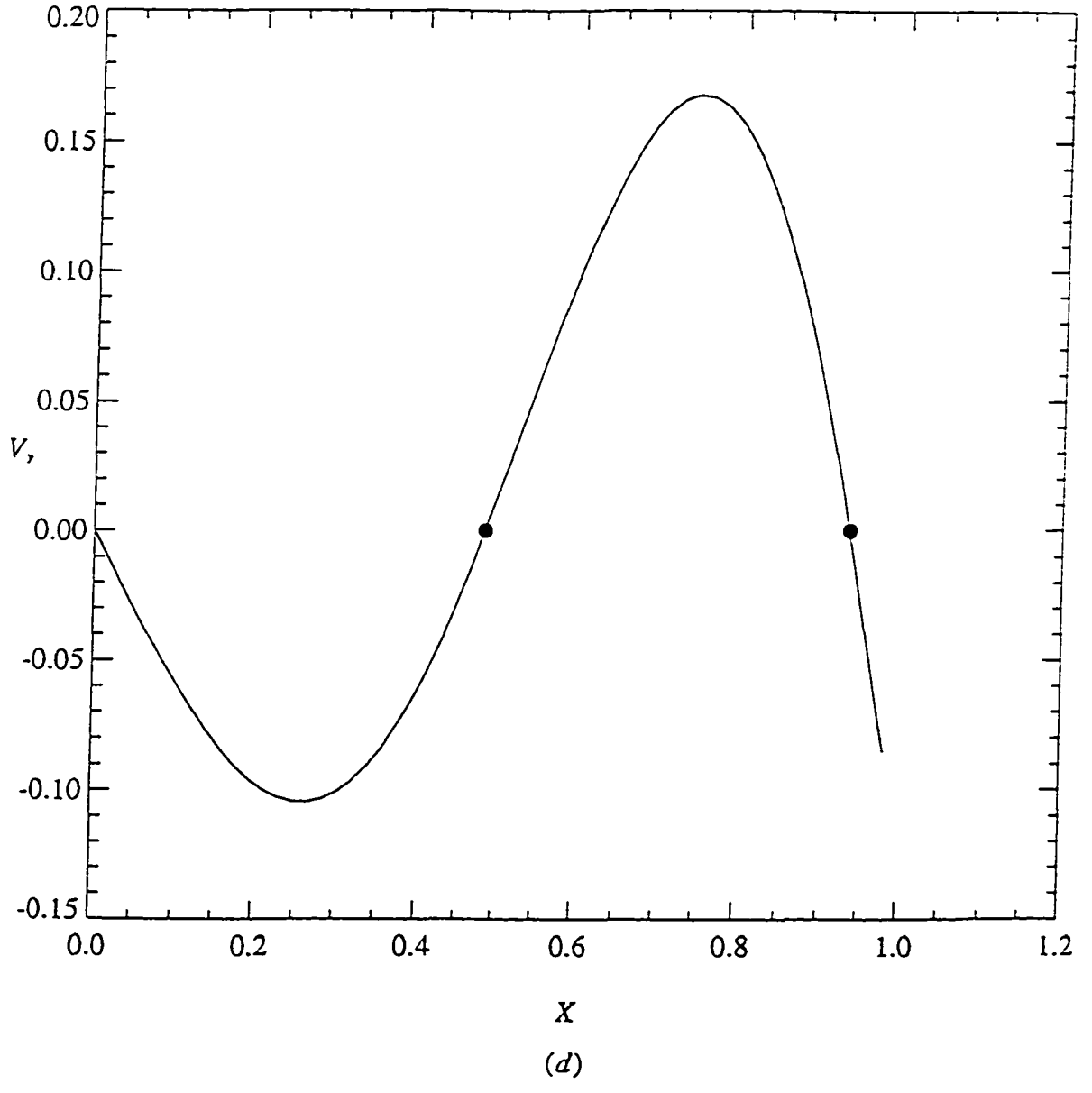

Fig. 5.17 — The y-component of the flow on the x-axis with two critical points (solid circles).

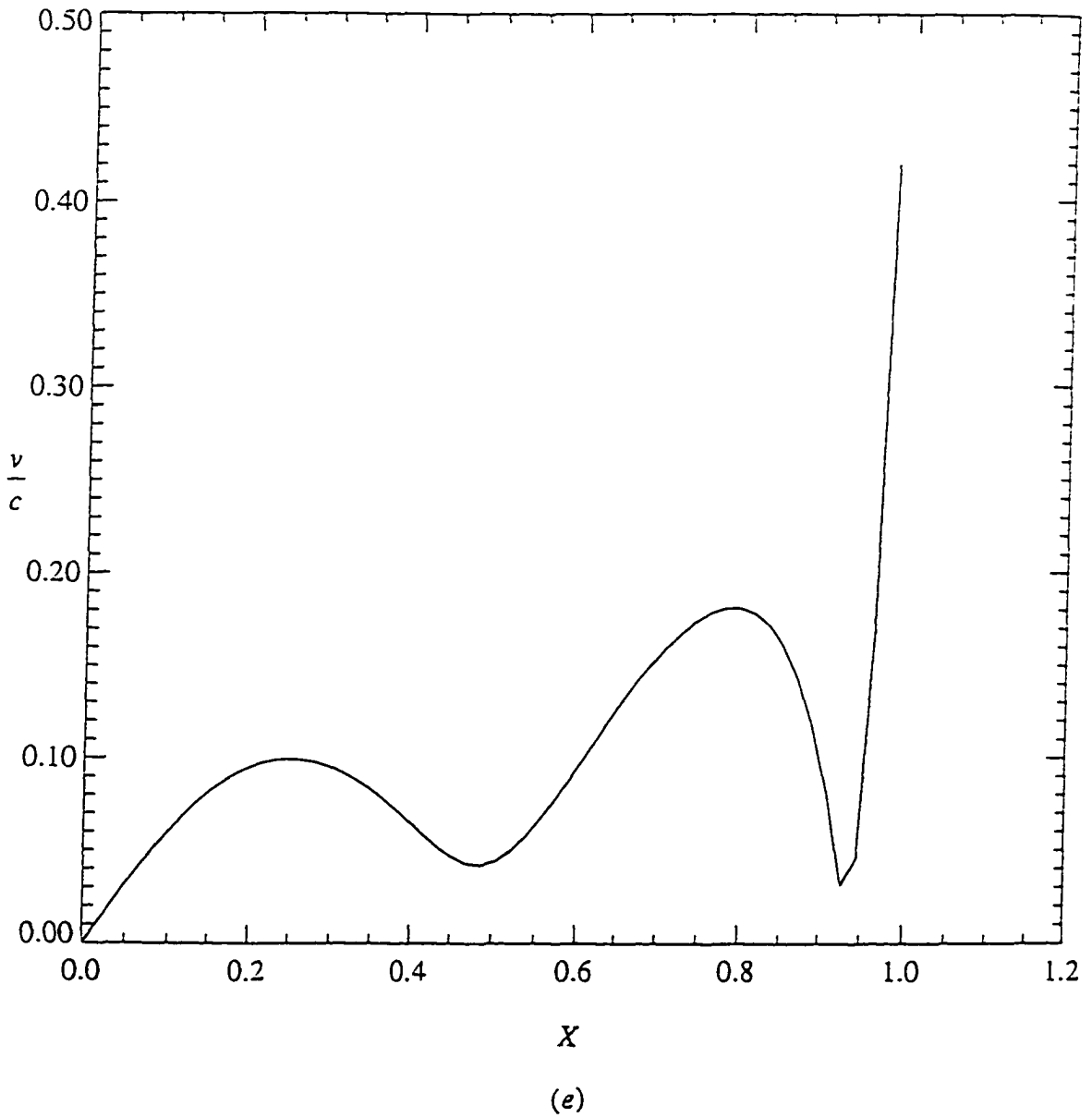

Fig. 5.17 — The dimensionless ratio v/c on the x-axis.

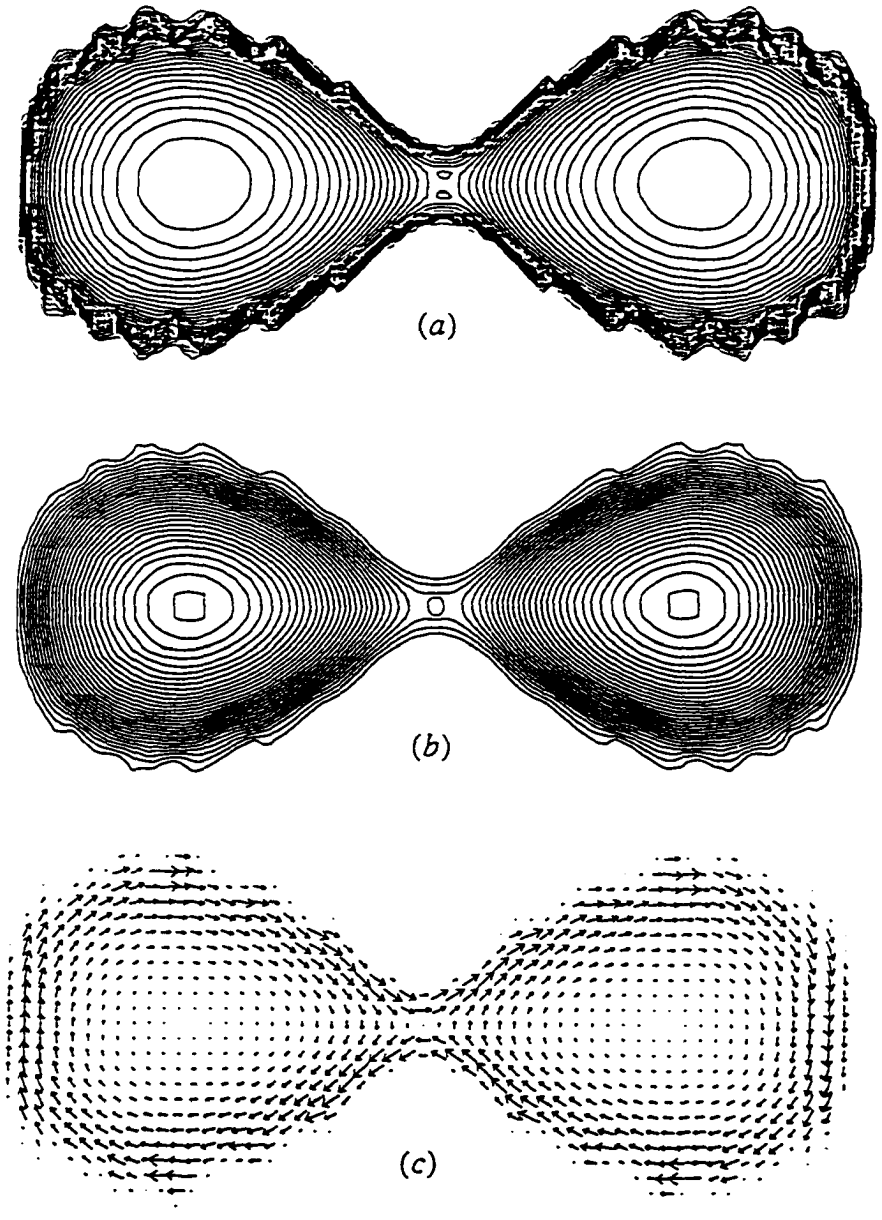

Fig. 5.18 — (Model D10) A loosely coupled binary disk at low vortensity.

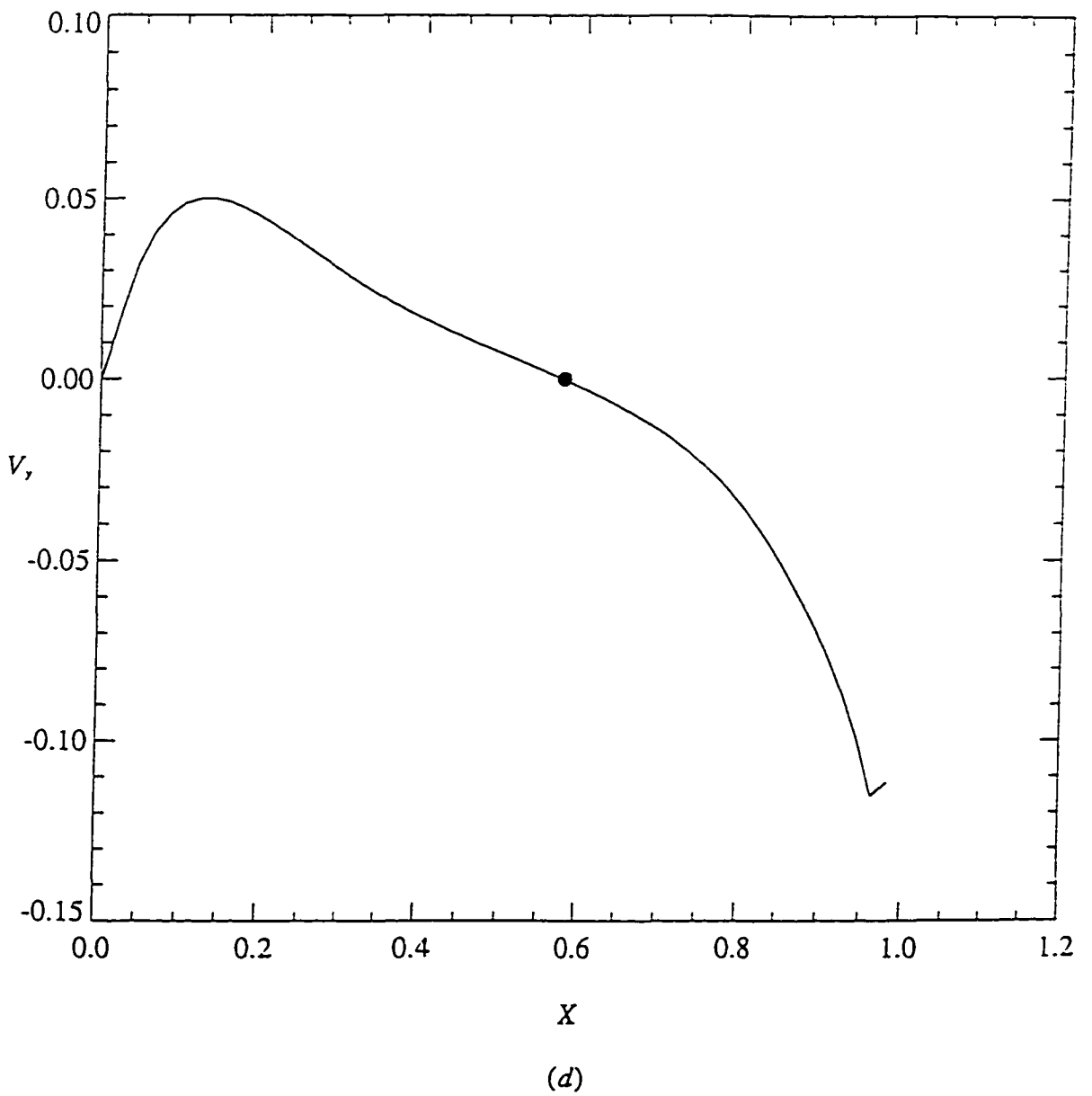

Fig.5.18 — The y-component of the flow. The solid circle corresponds to the off-centered vortex in the right half component.

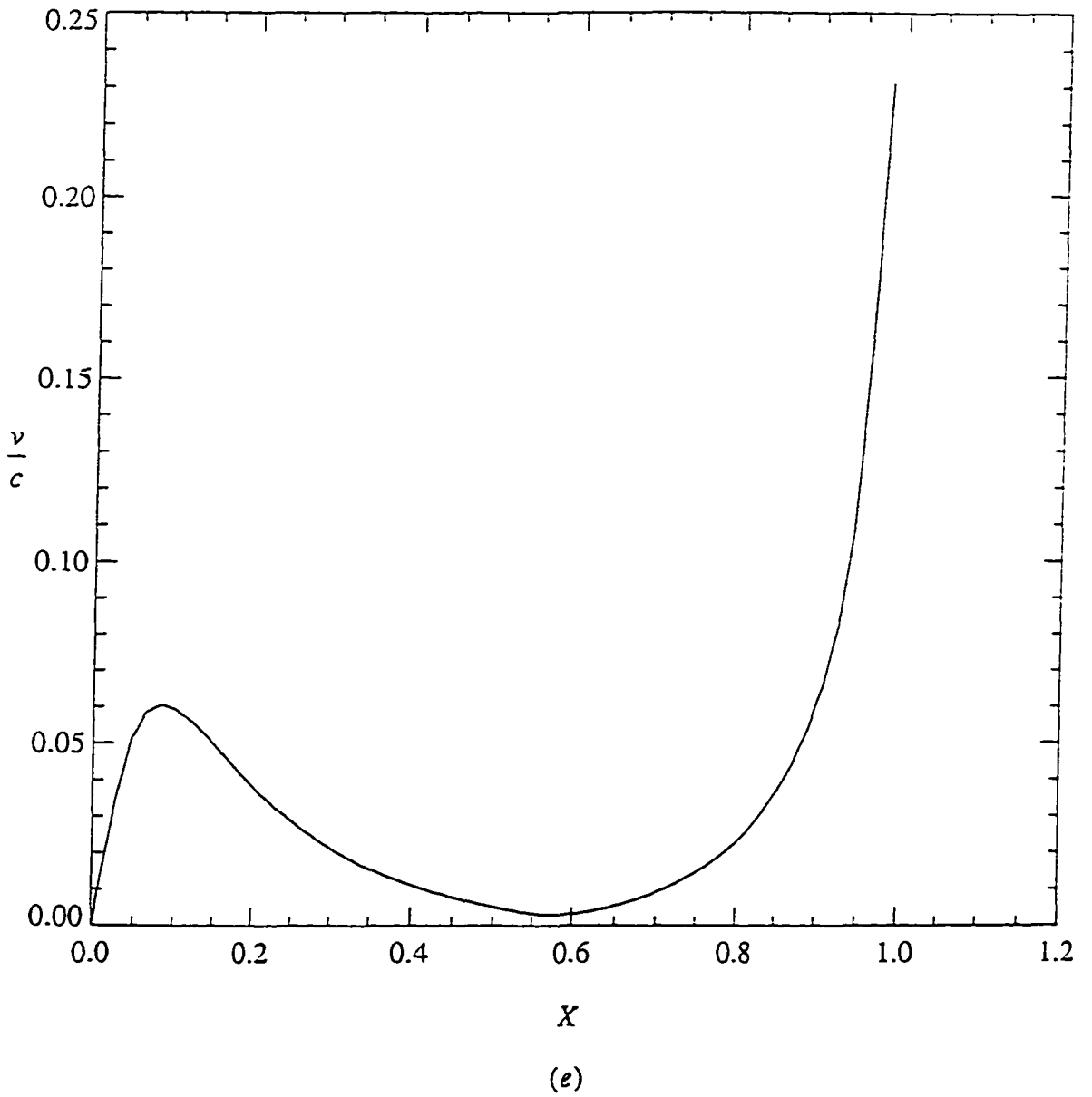

Fig. 5.18 — The v/c ratio on the x-axis.

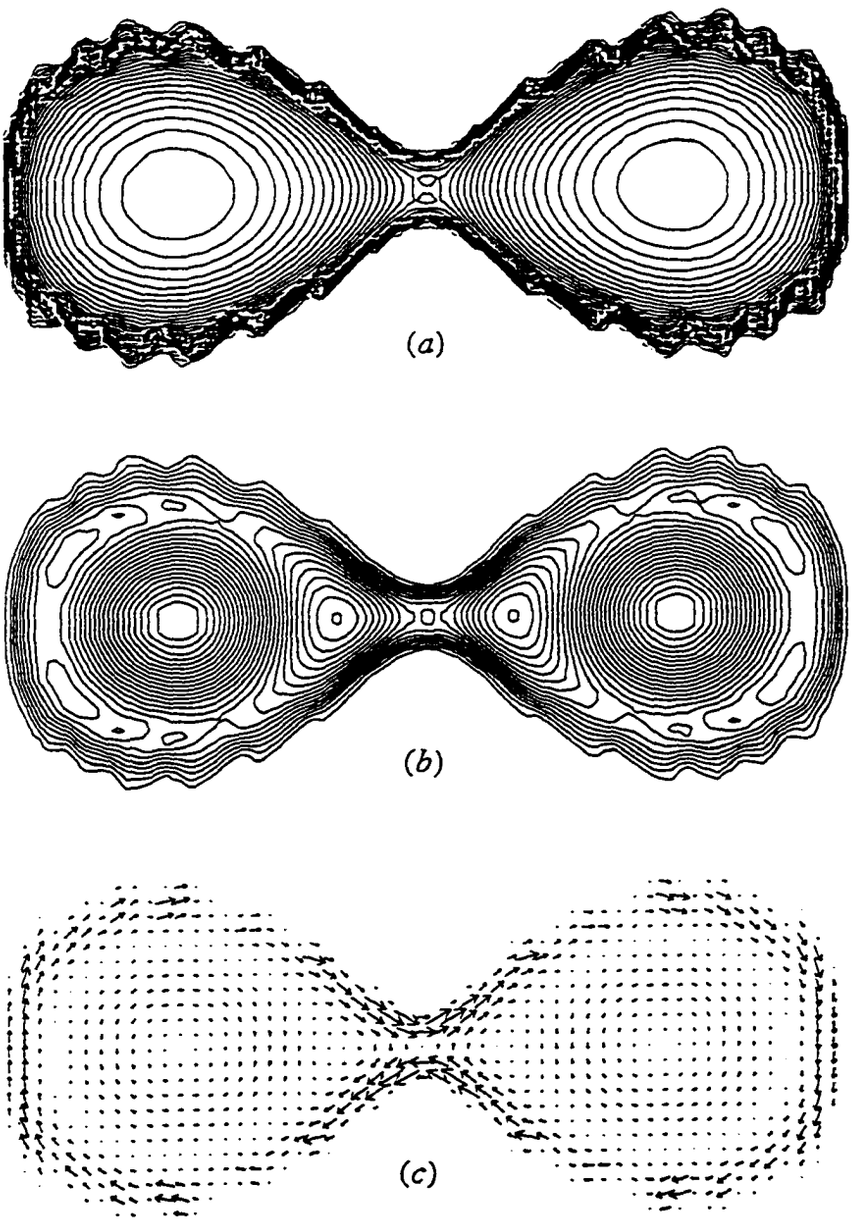

Fig. 5.19 — (Model D11) The same as in fig. 5.18 but at intermediate vortensity. The two components have their own independent sets of vortices and stagnation points (critical points). A small amount of fluid flow circulates around both components near the boundary.

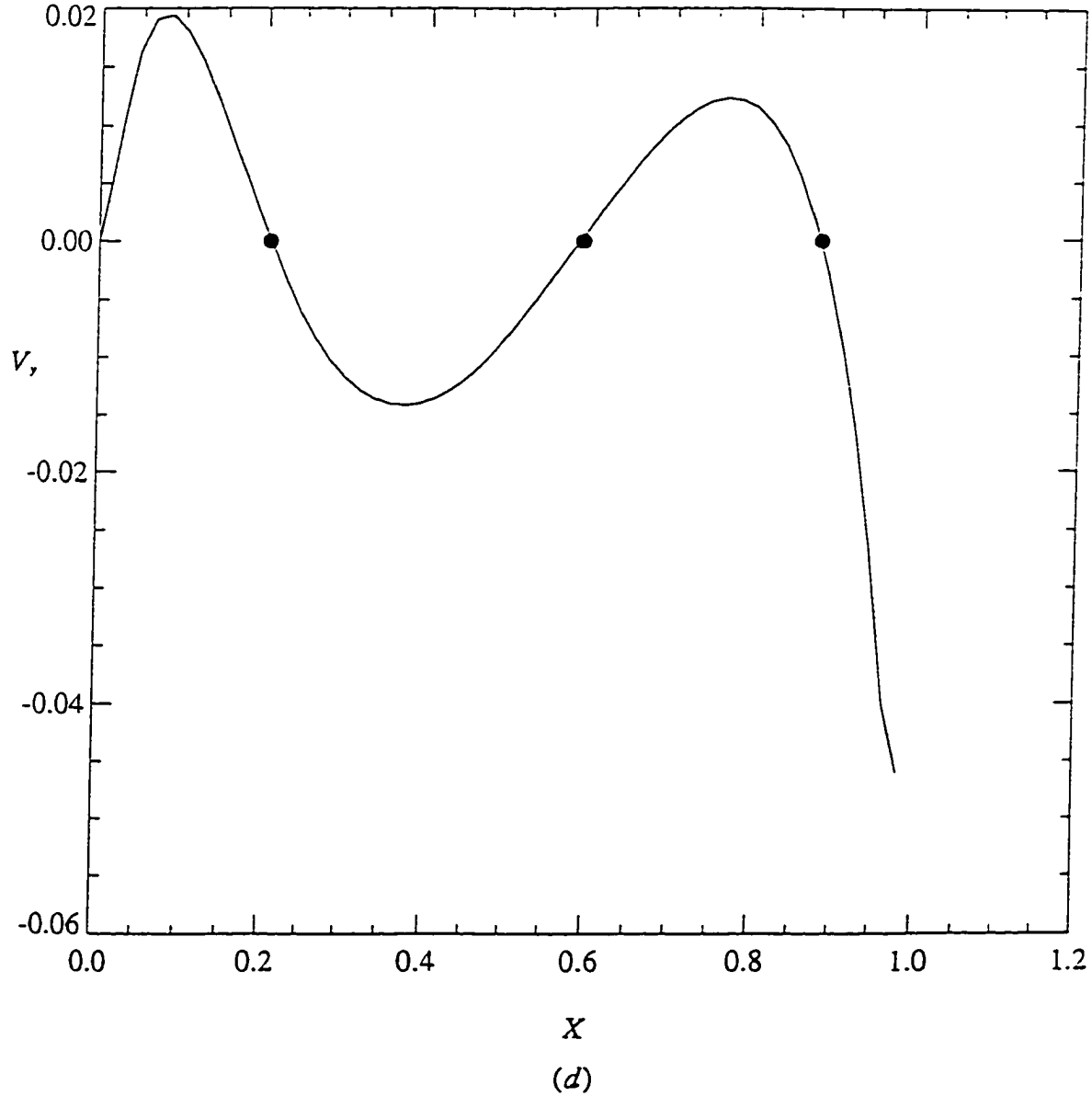

Fig. 5.19 — The y-component of the flow and the critical points (solid circles) on the x-axis.

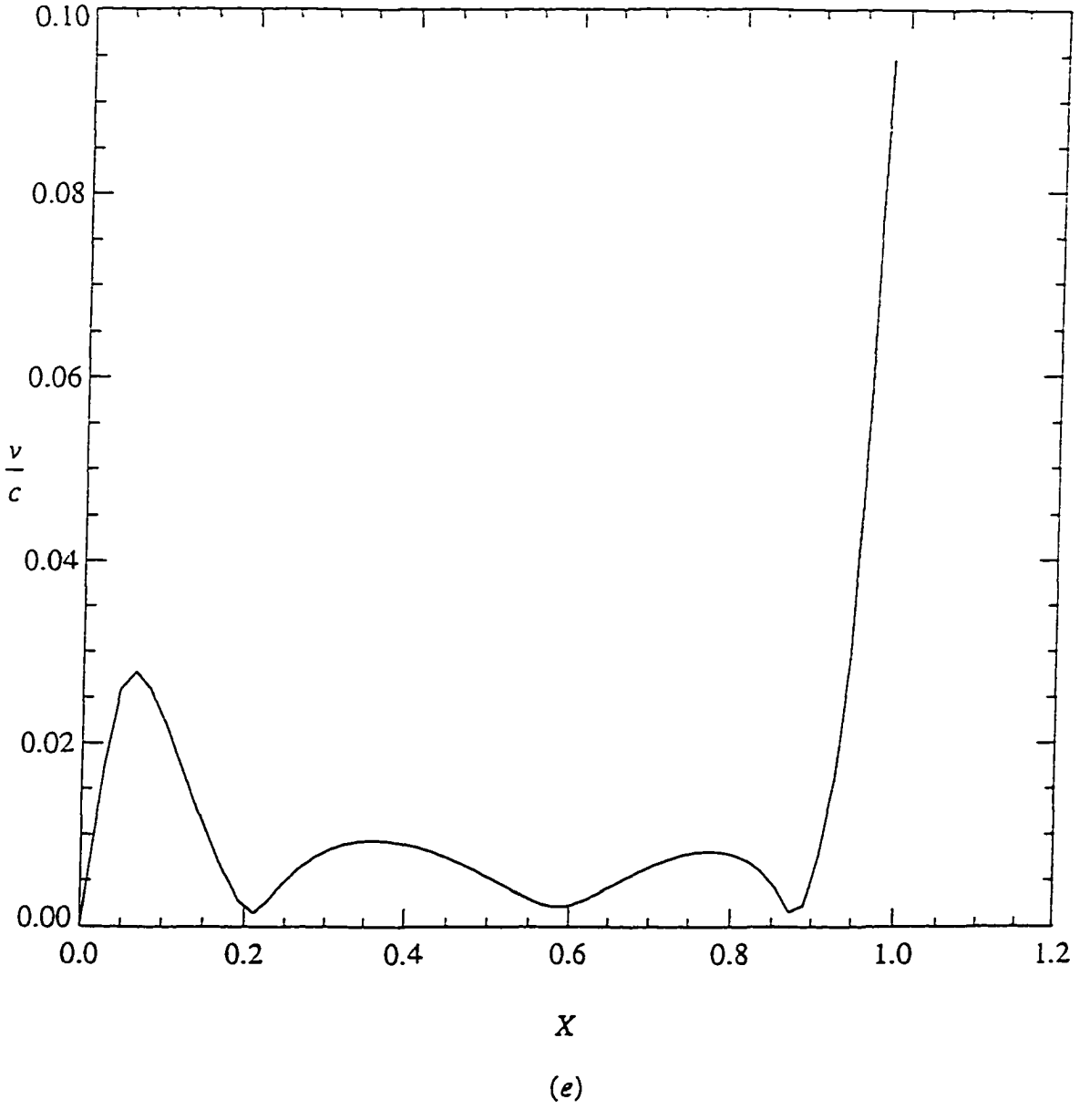

Fig. 5.19 — The v/c ratio on the x-axis.

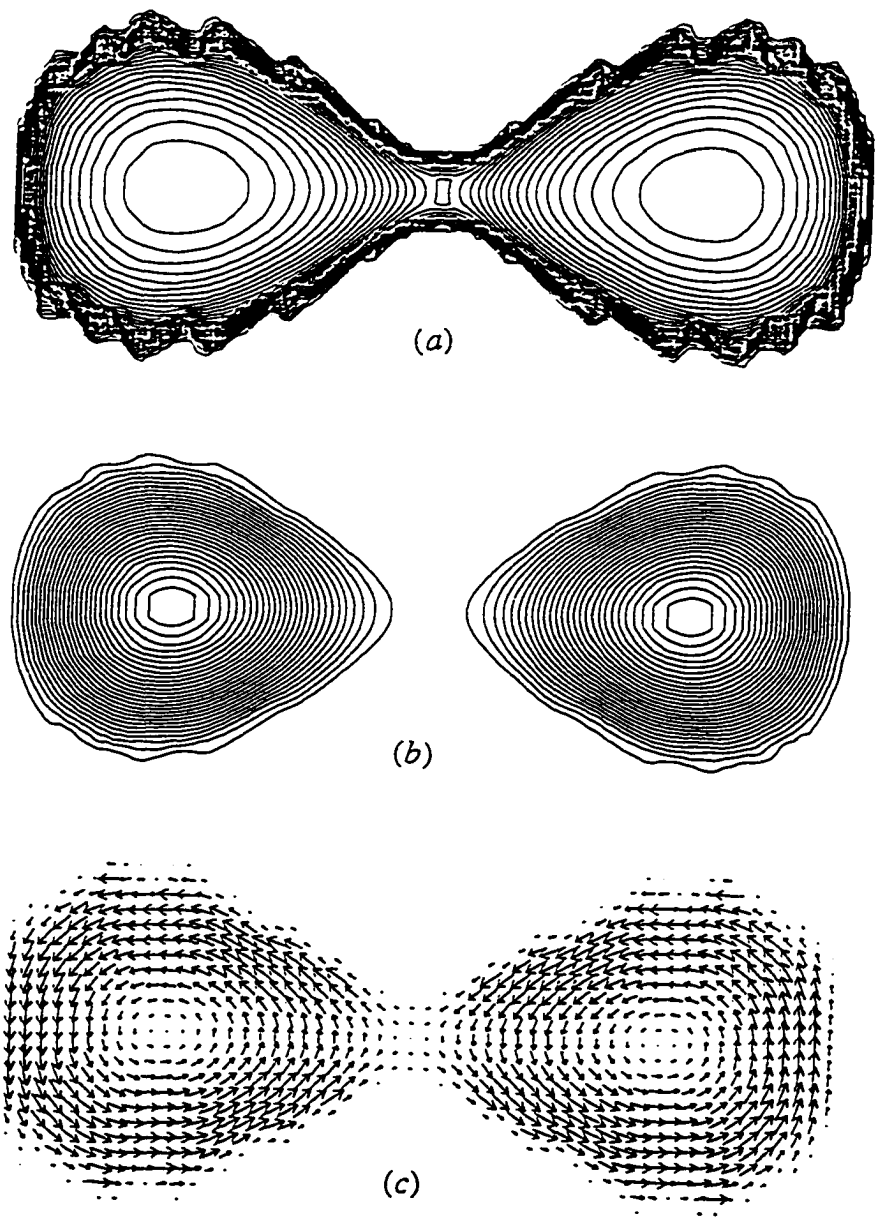

Fig. 5.20 — (Model D12) The same as in fig. 5.18 but at higher vortensity. The flow now is prograde everywhere.

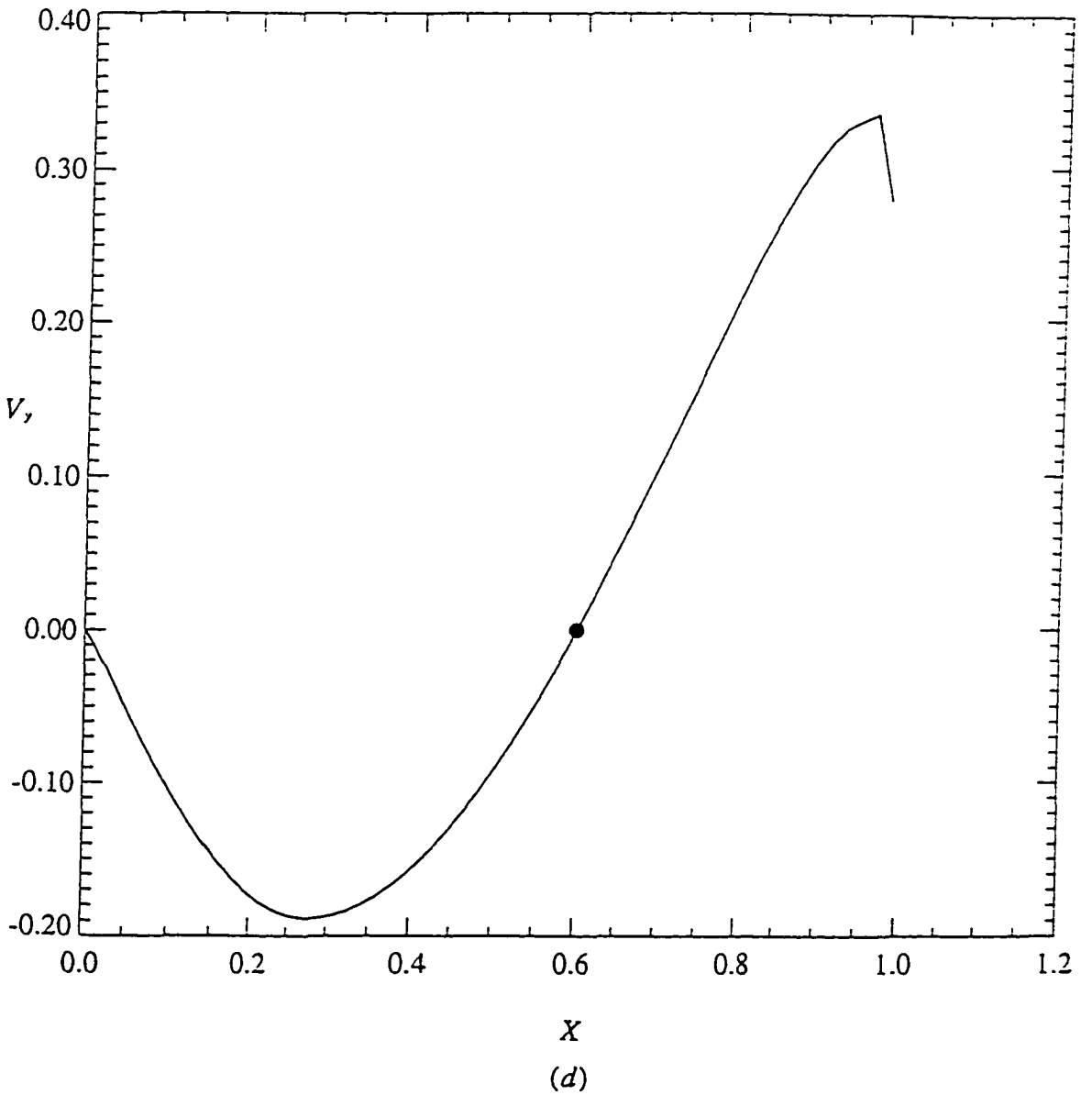

Fig. 5.20 — The y-component of the flow on the x-axis.

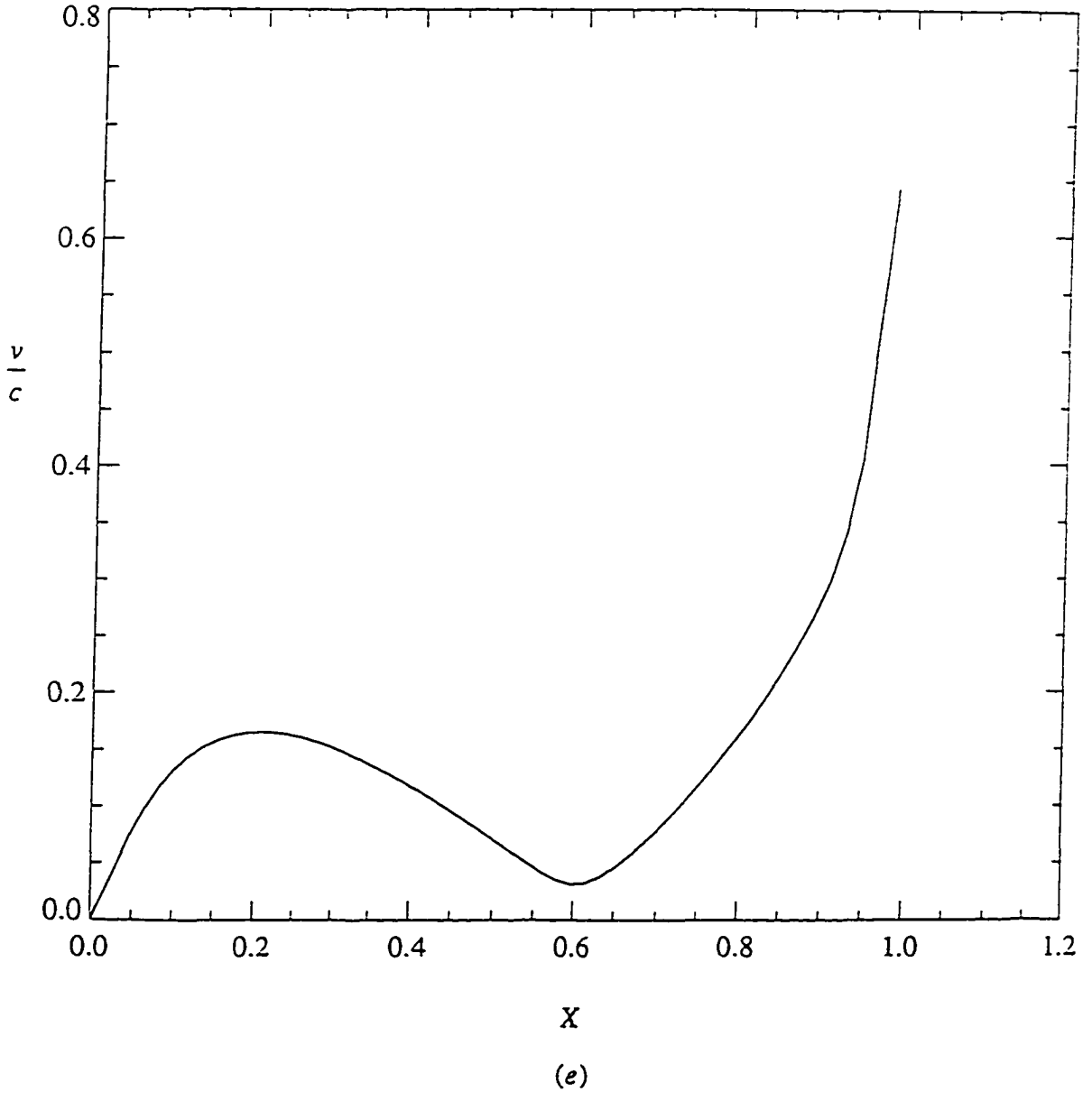

Fig. 5.20 — The v/c ratio on the x-axis.

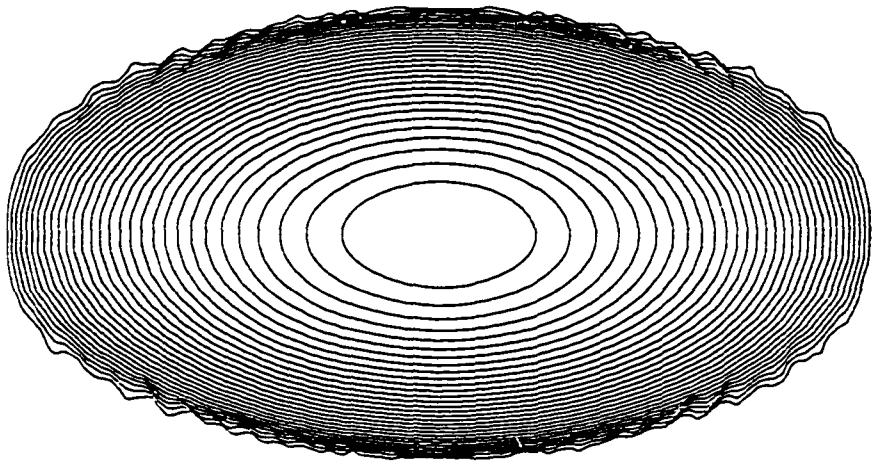

(*a*)

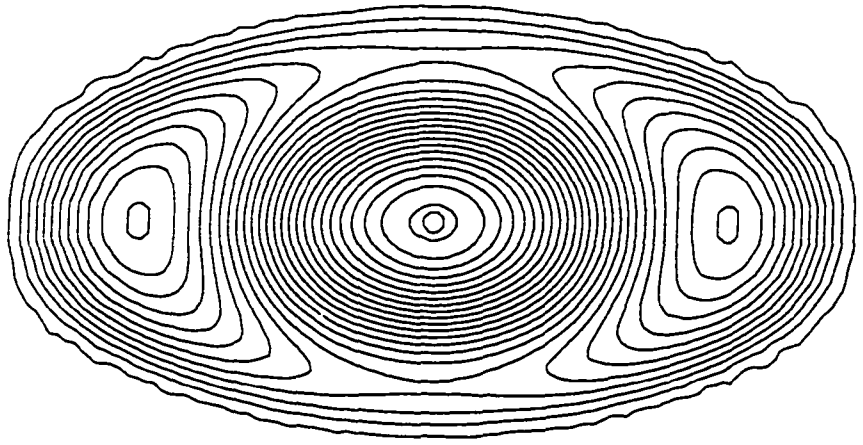

(*b*)

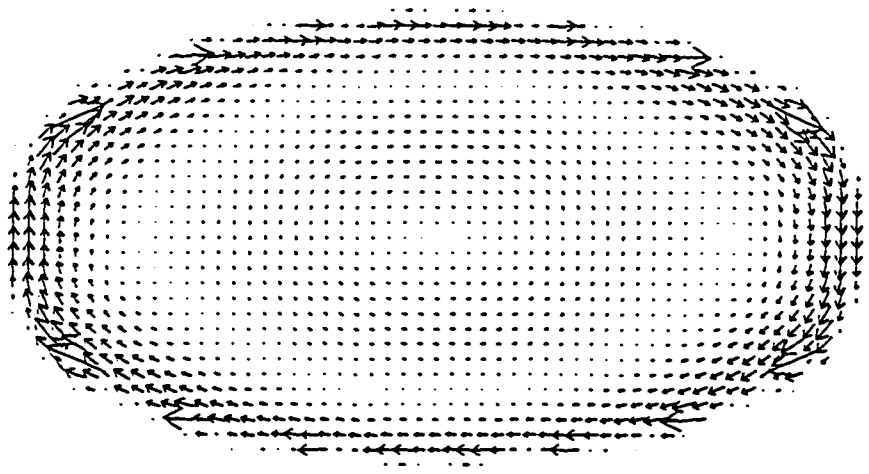

(*c*)

Fig. 5.21 — (Model D23) An elliptic-like disk with an intermediate amount of vortensity and with polytropic index n = 0.7.

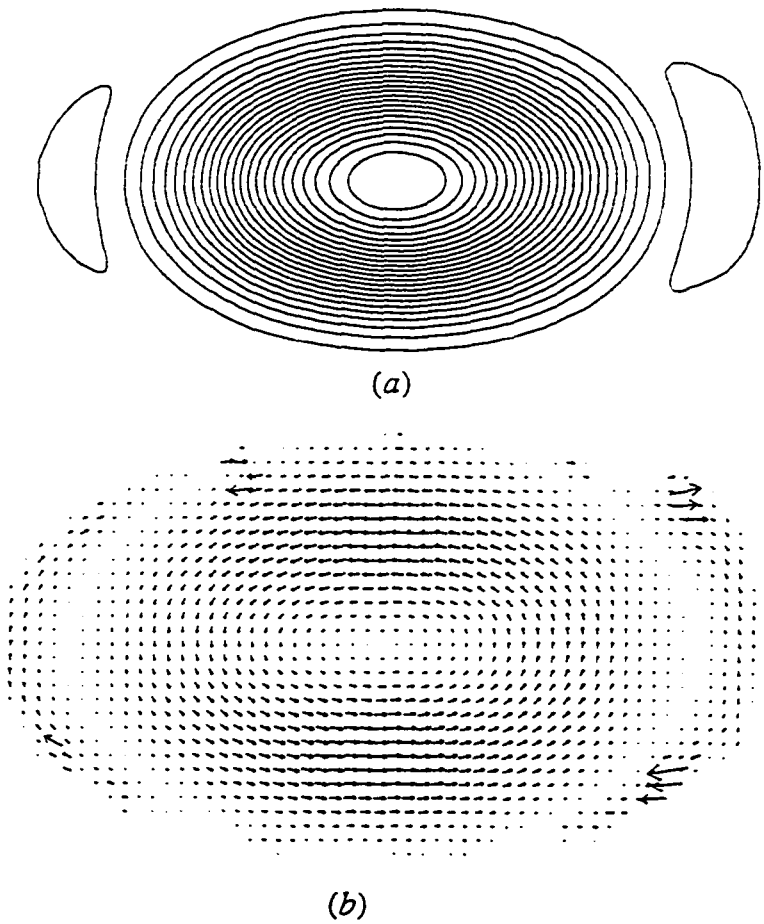

(*a*)

(*b*)

Fig. 5.22 — (Model D29) A disk at higher polytropic index n = 1.0.

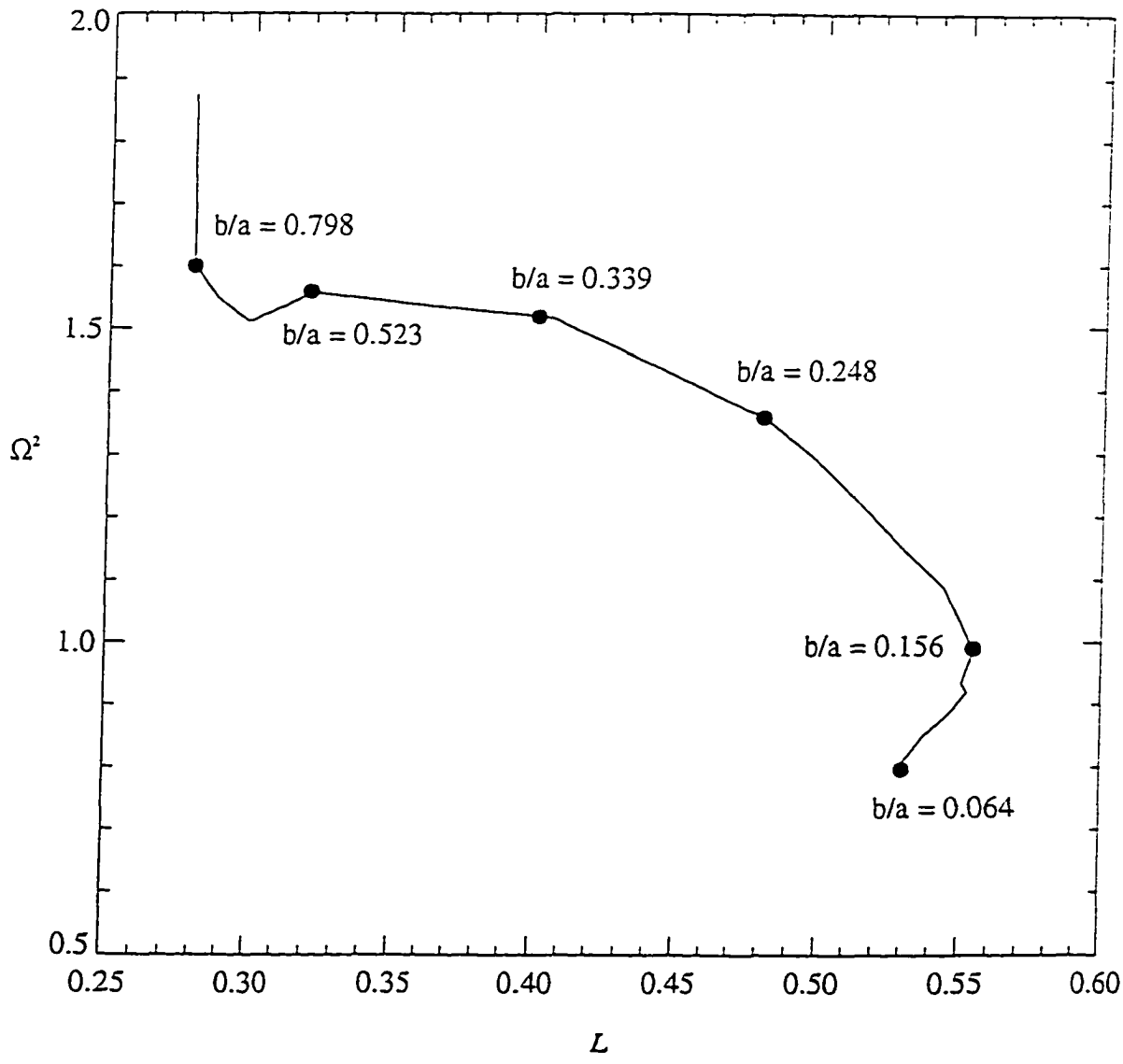

Fig. 5.23 — A sequence of two dimensional disks in the (Ω^2, L) - plane with n = 0.4 and C_0 = 3.5. The higher Ω-values (smaller L-values) correspond to rounder models (e.g. model D19). At larger values of L, the models become more like dumbbells. The tail end of the plot (L = 0.52) corresponds to loosely coupled binary system (e.g. models 5.18–5.20).

5.3 Present Numerical Restrictions

At present we can construct models with a star-convex geometry, that is, the radial line extending to the boundary must reside entirely inside the region of the fluid motion. Strictly speaking this is not a limitation of the numerical technique but rather has been adopted here as a matter of computational convenience to obtain a subset of the possible geometries. As a result, some configurations with multiple components such as binary disks are not obtainable with our present numerical algorithm.

In obtaining these models, we began each model iteraction by guessing an elliptic geometry with a uniform density distribution and no internal motion. Although the final converged equilibrium model has in most cases been very different from the initial guess, this choice of the initial guess does not seem to have been critical in almost all circumstances except in extreme cases. In those cases (e.g., very high vortensity, close to zero or one axis-ratios, high polytropic index) a better initial guess would be important. In those situations, if the initial and the final models are too far apart, a convergence path may not exist between them.

CHAPTER 6

SUMMARY AND CONCLUSION

More than a decade after the pioneering work of Papaloizou & Pringle (1984) led to the discovery of the P-modes in zero-mass disk models orbiting around a central object, we are beginning to realize that these unstable modes may not play a role in the dynamics of real accretion disks because they generally exist only in models with extremely low mass ratios ($M_D/M_C << 1$) and extremely small disk aspect ratios ($\varepsilon << 1$). Our analysis of the three principal modes of instability in reasonably slender incompressible tori with constant specific angular momentum and nonzero mass M_D shows that the P-modes are eliminated by the introduction of a small amount of self-gravity in the initial equilibrium models. This result is not in contradiction with previous investigations that have detected strong P-modes only in models with massless tori in which the self-gravity of the orbiting matter was not included for simplicity. On the contrary, this difference indicates that the results obtained for massless disks do not extend to disks with small but nonzero masses. We also note that the P-modes do survive in some low-mass, radially slender models but the disk masses and the aspect ratios of these models are so small that the unstable modes cease to be of any interest for both protostellar and AGN accretion disks.

As the self-gravity of the disk is increased relative to the external gravity due to the central object or as the thickness of the disk is decreased at constant component masses, the I-modes appear first and before the J-modes. These self-gravity-driven

modes of instability were originally studied by Goodman & Narayan (1988) and our work is a direct extension of their investigation to models with any reasonable amount of self-gravity (i.e., $0 < M_D/M_C \leq \infty$). In practice, the J-modes can dominate in strongly self-gravitating disk systems in which the rapidly rotating gas is necessarily distributed in slender rings. If nature experiments with such massive narrow structures, their imminent and violent breakup from the action of J-modes may provide a physical mechanism for the formation of multiple star systems from protostellar self-gravitating rings whose mass content grows dramatically by infall/accretion processes. However, with regard to the dynamics of conventional accretion disks around stars and protostars, we should focus our attention on the I-modes because these are the only unstable modes which are not restricted to limited regions of the parameter space but operate over a wide range of disk/star mass ratios and over a wide range of disk aspect ratios.

Our results support the previously proposed idea in the context of star formation that long-wavelength I-modes may be of fundamental importance in the formation of binary stars and small groups of stars from the breakup of accretion disks into few fragments. On the other hand, they indicate that low-mass circumnuclear disks surrounding supermassive black holes in AGN are in no danger of breaking up due to the action of P-modes, I-modes, or J-modes because they are not expected to be sufficiently slender or sufficiently massive. Therefore, in the context of purely hydrodynamical instabilities in AGN disks, we believe that the old

ideas about fat accretion tori providing the "funnel" to guide axial outflows and assisting the collimation of jets may still have merit or, at the very least, they are not threatened by the existence of unstable P-modes in models with low-mass narrow rings around massive central objects.

We have formulated a new computational technique (2DSCF) to obtain a new class of equilibrium structures which could not be obtained with previously existing self-consistant-field methods. The numerical method formulated in the preceeding chapters is a generalization of the HSCF method and is appropriate for obtaining two-dimensional equilibrium structures with self gravity. The HSCF method has been tested and successfully applied to construct a wide variety of astronomical models.

The 2DSCF technique shares with HSCF several features. Both methods adopt an integral representation of the Euler's momentum equation (ME) instead of the differential equations, and they allow for the presence of self-gravity. In both methods, the same three quantities—maximum density, R_A on the x-axis, and the gravitational constant G are normalized to unity. However, the two methods differ in several important ways. Whereas in the HSCF method the internal flow is specified via a power-law distribution in advance, this is not the case with the 2DSCF method. The internal flow was derived from a scalar function known as the stream function. For each model, the stream function was obtained through the solution of a self-adjoint, elliptic partial differential equation (PDE) obtained from the vorticity equation. Since the internal flow was derived from the stream function,

which itself depended indirectly on other dynamical parameters, it was possible to obtain highly complex and nontrivial flows.

Another important feature of the 2DSCF was that the fluid was allowed to be compressible and nonaxisymmetric, in addition to having nontrivial internal flow. The lack of azimuthal symmetry coupled with the presence of internal flow and compressibility called for the inclusion of the equation of continuity to the set of simultanuous coupled equations governing the motion of the fluid.

The mathematical settings describing the general compressible fluid motions were derived in chapter 2. The general Euler's momentum equation for inviscid, isentropic (and ideal) fluids was derived. The fluid motion was constrained to the x-y plane. The thermodynamic properties of the fluid were incorporated into the equations of motions through the polytropic equation of state.

The resulting set of coupled nonlinear PDEs was solved for a special class of two-dimensional flows and for two types of two-dimensional systems: infinite cylindrical polytropes and finite, two-dimensional disks. The latter spanned a larger parameter space and proved to be more flexible in terms of the allowed configurations, geometries, and internal flow topologies.

These compressible models with non-linear internal vortical flow are intended to serve as an intermediate step between the classical, incompressible ellipsoidal models and the fully general, triaxial solutions to be developed in the future. They provide a more realistic framework within which to model and study astronomical structures.

With the method developed in the proceeding chapters, we were able to construct various equilibrium configurations by varying a small set of free parameters. In particular, by choosing different values of the vortensity (defined as the ratio of vorticity to density) parameter, we could vary the topology of the flow considerably. For small values of vortensity, the flow was retrograde and of relatively small amplitude. For some intermediate values, the dynamics and topology of the flow was governed by the presence of several vortices and stagnation points. The outer portion of the flow near the surface was always opposite the frame rotation due to the constraint placed on the vorticity, as explained below. The streamlines in the interior region were partitioned into topologically disjoint regions enclosing several vortices. The dynamics of the vortical flow was governed by the interaction among these critical points. In the special case of dumbbells with very small axis ratios, the internal flow was highly non-linear and complex. At higher values of the vortensity, the flow would gradually shift toward prograde as the two off-centered vortices moved away from the central vortex toward the boundary until they would disappear entirely leaving the flow prograde around the central vortex.

The geometry of the configuration was determined by the position of the boundary point on the y-axis. With the cylindrical models, this axis ratio would result in various elliptic-like sequences from very elongated to very round models. The disks, on the other hand, behaved very differently for smaller axis-ratios. Below a certain point they lost their elliptic geometry and became rectangular-boxed with

round corners and eventually turned into dumbbells. It seemed these dumbbell-shaped structures were preferred over their elliptical counterparts in our 2DSCF.

Although the dumbbells were always perferred in our 2DSCF over the elliptical disks for small axis ratios, this may not indicate that there are no elliptical configurations with very small axis ratios. It simply illustrates that in our 2DSCF, the boundary of the fluid is free to change and move during each iteration except at the two fixed points A and B. And when the iteration converges, the boundary will settle on some closed contour which may be quite different from the initial guess. If, however, we hold the entire boundary fixed during the iteration (not just at two points A and B), then it may be possible to construct elliptical geometries with very small axis ratios.

Although the models studied were primarily restricted to disks and cylinders, the computational technique derived is not limited to only these topologies. The method applies equally well to configurations with multiple components such as binaries so long as the flow is constrained to two dimensions.

In obtaining the two-dimensional solutions to the general momentum equation for the ideal fluids, we sought solutions where the vortensity had certain properties. This in turn had an effect on the flow pattern near the boundary. In its general form the vortensity was expanded in a power series in the stream function that was unbounded in both directions. The expansion coefficients were free parameters and, in principle, could be chosen arbitrarily. Each different set of coefficients would uniquely correspond to its associated nonlinear PDE leading to a specific stream

function. Hence, in principle, there was an infinite family of stream functions with varrying degrees of topological flows.

In general, it is not required for the vortensity to be expanded explicitly in terms of a power series in the stream function. The set of coupled nonlinear PDEs could have been solved directly with some appropriate boundary conditions. However, this method would have been far more difficult and less likely to lend itself to a numerically stable solution. There are no general, standard methods of solving a set of nonlinear PDEs.

The impact of the vortensity expansion in a power series in the unknown function was two fold. First, it allowed us to readily integrate the PDEs and obtain an exact solution in closed analytic form resulting in the scalar momentum equation which was a major component of the 2DSCF method. Second, but of lesser importance, was that the fluid vorticity was always a specific constant on the surface. Due to the physical requirement that the density and pressure vanish on the boundary, this constant was -2Ω. As a result, the fluid had the tendency to go opposite to the constant frame rotation in regions very close to the surface. However, this behaviour due to the boundary effect was not a limitation on the possible fluid motions. The boundary region affected, in general, depended on the internal kinetic energy of the fluid. At low energies, the fluid motion was retrograde everywhere and thus in agreement with the boundary requirement. At some intermediate energies the presence of several vortices and stagnation points would generate a flow which would also conform to the flow on the boundary. The flow

around the off-centered vortices and near the boundary was always retrograde, and, around the central vortex, prograde. The retrograde flow in the boundary region was always confined to a narrow strip just inside the surface. At higher energies the narrow strip would gradually shrink towards the surface until it would completely disappear, leaving the flow prograde everywhere.

We chose to incorporate only the zeroth and the first order terms (C_0 and C_1) in the vortensity series, and set the rest of the coefficients equal to zero. The primary reason for choosing only the linear terms in the expansion series was to have the resulting PDE for the unknown stream function to be linear. Although, the higher positive order terms in the series are probably of negligible importance in the flow pattern, that may not generally hold true for the negative power terms. The inclusion of terms with negative order in the vortensity would result in additional terms in the scalar momentum equation that, in general, are of logarithmic form or terms involving negative powers of the stream function. As a result, the stream function may not vanish anywhere inside or on the boundary. It is possible then, that a solution to such a nonlinear PDE, if it exists, will be very different from those studied in the previous chapters, possibly with different flow topologies. Whether or not these types of solutions are of any physical significance or if they are just pure mathematical remains to be seen.

REFERENCES

Adams, F. C., Ruden, S. P., & Shu, F. H. 1989, ApJ, 347, 959.

Andalib, S. W., Tohline, J. E., & Christodoulou, D. M. 1997, ApJ Suppl. 108, 471-487.

Bryan, G. H. 1889, Phil. Trans. R. Soc. Lond., A, 180, 187.

Chandrasekhar, S., Ellipsoidal Figures of Equilibrium, (New Haven and London, Yale University Press, 1969a).

Christodoulou, D. M. 1993, ApJ, 412, 696 (C93).

Christodoulou, D. M., & Narayan, R. 1992, ApJ, 388, 451 (CN).

Christodoulou, D. M., Kazanas, D., Shlosman, I., & Tohline, J. E. 1995a, ApJ, 446, 500.

Christodoulou, D. M., Kazanas, D., Shlosman, I., & Tohline, J. E. 1995b, ApJ, 446, 510.

Dedekind, R. 1860, *J. Riene Angew. Math., 58,* 217 - 28.

Dirichlet, G. 1860, J. Reine Angew. Math., 58, 181-216.

Dyson, F. W. 1893, Phil. Trans. Roy. Soc., 184A, 1041.

Eriguchi, Y., & Hachisu, I., 1985, AA, 142, 256.

Frank, J. & Robertson, J. A., 1988, MNRAS, 232, 1.

Goldreich, P., Goodman, J., & Narayan, R. 1986, MNRAS, 221, 339.

Goodman, J., & Narayan, R. 1988, MNRAS, 231, 97 (GN).

Hachisu, I., 1986, ApJS, 61, 479.

Hunter, C. 1963, MNRAS, 126, 299.

Jacobi, C. 1882, Poggendorff Annalen der Physik und Chemie, 33 (1834), 229-38; reprinted in Gesammelte Werke 2 (Berlin, G. Reimer), 17-72.

Jeans, J. H. 1902, "On the Equilibrium of Rotating Liquid Cylinders.

Kojima, Y. 1986, Prog. Theor. Phys., 75, 251.

Landau, L. D., and Lifshitz, E. M., Fluid Mechanics, 2nd edition, Pergamon Press, 1987.

Maclaurin, C. 1742, "A Treatise on Fluxious".

Maxwell, J. C. 1859, 1890 Scientific Papers, 1, 288.

Meyer, C. O. 1842, J. f. reine und angew, Math. (Crelle) 24, 44.

Ostriker, J. 1964, ApJ, 140, 1067.

Papaloizou, J. C. B., & Pringle, J. E. 1984, MNRAS, 208, 721.

Poincare, H. 1885, *Acta Math.*, 7, 259-380.

Riemann, B. 1892 *Abh. d. Konigl. Gesell. der Wis. zu Gottingen, 9 (1860)*, 3- 36; see also *Gesammelte Mathematische Werke (* Leipzig, B. G. Teubner, 1892), P 182.

Shu, F. H., Adams, F. C., & Lizano, S. 1987, ARA&A, 25, 23.

Tohline, J. E., & Hachisu, I. 1990, ApJ, 361, 394 (TH).

Weinberg, M. D., & Tremaine, S., 1983, 271, 586, 96-A1 (1983).

Weinberg, M. D. 1983, 271, 595, 96-A10.

Wong, C.-Y. 1974, ApJ, 190, 675.

Woodward, J. W., Tohline, J. E., & Hachisu, I. 1994, ApJ, 420, 247 (WTH).

VITA

Saied W. Andalib did his undergraduate work first at College of Charleston, Charleston, South Carolina in 1979. Then he continued his education at Virginia Polytechnique Institute & State University, Blacksburg, Virginia, where he received his Bachelor Degrees of Science in Mathematics and Physics in 1983.

Saied persued his graduate study at Louisiana State University, Baton Rouge, Louisiana, where he earned Master of Science Degrees in Physics in 1987 and in Electrical & Computer Engineering in 1990. He is expected to earn his Ph.D. in Mathematical and Computational Physics in May 1998.

Saied taught physics labs and night classes of astronomy for seven years. He was in charge of the LSU Planetarium and worked with the LSU Observatory for several years.

Saied has been employed full time as a Computer Analyst since 1991.

DOCTORAL EXAMINATION AND DISSERTATION REPORT

Candidate: Saied Andalib

Major Field: Physics

Title of Dissertation: The Structure and Stability of Selected, 2-D Self-gravitating Systems

Approved:

Major Professor and Chairman

Dean of the Graduate School

EXAMINING COMMITTEE:

R.F. O'Connell

Date of Examination:

March 19, 1998

IMAGE EVALUATION TEST TARGET (QA-3)

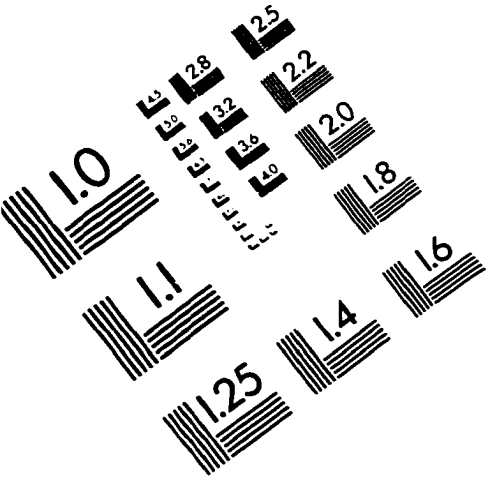

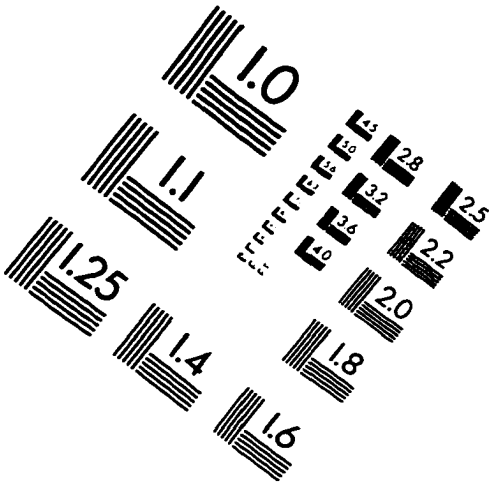

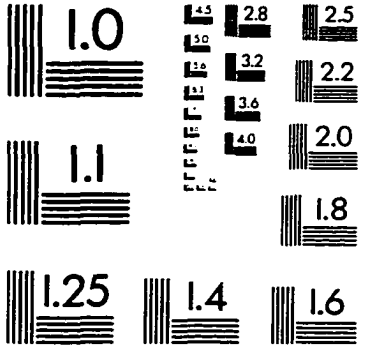

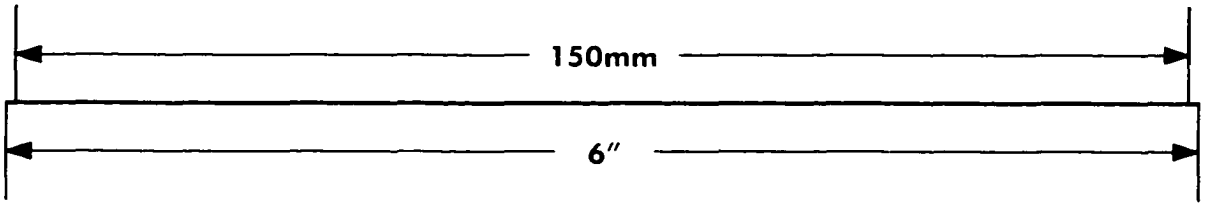

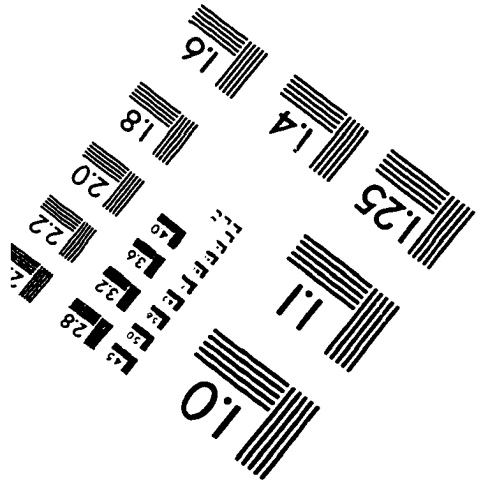

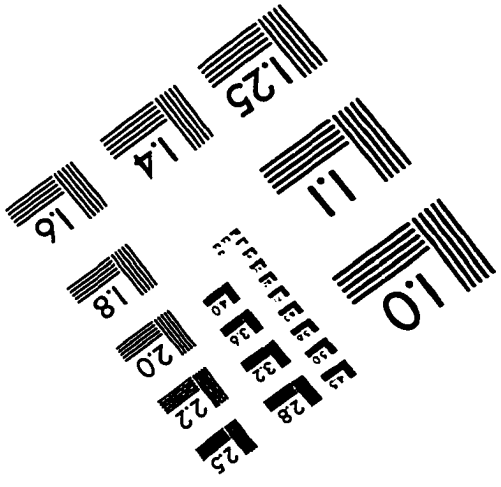

APPLIED IMAGE, Inc
1653 East Main Street
Rochester, NY 14609 USA
Phone: 716/482-0300
Fax: 716/288-5989